

UNIVERSITY OF PENNSYLVANIA

Encoding and Enhancing Acoustic Information  
at the First Stages of the Auditory System

A thesis proposal submitted in partial satisfaction of  
the requirement for the degree Doctor of Philosophy

in

Bioengineering

by

John Henry Wittig Jr

Primary Advisor:

Kwabena Boahen

Committee Members:

George Gerstein, Chair

Donata Oertel (remote)

Tom Parsons

Marc Schmidt

April 6, 2004

## Table of Contents

<b>I. Abstract</b> .....	1
<b>II. Specific Aims</b> .....	2
Aim 1: Encoding Temporal Information at the Inner Hair Cell Synapse	
Aim 2: Enhancing Auditory Information in the Cochlear Nucleus	
<b>III. Background and Significance</b> .....	4
1. Encoding Information at the Auditory Periphery	
2. The Cochlear Nucleus: Architecture, Response Profiles, and Output Paths	
3. Information Enhancement within the Cochlear Nucleus	
a. Phase locking by bushy cells	
b. Sound spectrum by t-stellate cells	
c. Amplitude modulation by octopus cells	
d. Spectral features by fusiform and giant cells	
4. Summary	
<b>IV. Preliminary Results</b> .....	15
1. Software Hair Cell Model	
2. Silicon Cochlear Nucleus Model	
a. Bushy cell synaptic connectivity	
b. Bushy cell <i>in vitro</i> characterization	
c. Silicon bushy cell model	
d. Data from silicon auditory neuron chip	
<b>V. Research Design and Methods</b> .....	23
1. Software Model of the Hair Cell Synapse	
2. Silicon Model of the Cochlear Nucleus	
3. Aim 1 Goals	
4. Aim 2 Goals	
5. Proposed Timeline	
<b>VI. Facilities</b> .....	27
<b>VII. Literature Cited</b> .....	28
<b>VIII. Appendices</b>	
1. Hair Cell Synapse Methods and Poster .....	37
2. Parameters of Bushy Cell Conductances.....	46
3. Circuit Model of Class Chip Neuron with $K_{LT}$ .....	47
4. Conductance Neuron Circuit Model.....	57

## **I. Abstract**

I propose to examine how anatomical and physiological specializations enable the mammalian nervous system to encode and enhance acoustic information. In particular I am interested in the first levels of acoustic processing: encoding sound at the inner hair cell afferent synapse and enhancing sound features a single synapse later at the cochlear nucleus. In the inner hair cells, large numbers of synaptic vesicles are tethered close to each presynaptic active zone by synaptic ribbons, which likely contribute to the extended duration and temporal precision of exocytosis in these cells. I propose to computationally examine how presynaptic calcium buffering affects this synapse's ability to encode timing information. In the cochlear nucleus, various cell types enhance acoustic information, such as waveform phase, spectrum, and pitch, despite variability in neuronal components such as conductance activation threshold, maximal conductance levels, and synaptic convergence. Using a physical model with inherent component variability, I propose to theoretically explore how the cellular and network architecture of the cochlear nucleus functions to consistently enhance acoustic information. Together, my proposed aims address how specializations in the first stages of the auditory system enable the remarkable perception of sound, by overcoming the temporal limitations of conventional synapses when encoding acoustic information, and by overcoming neural component variability when enhancing it.

## II. Specific Aims

### **Aim 1. Examines what limits the ability of the hair cell afferent synapse to convey temporal information at high frequencies**

Computational models of basilar membrane dynamics and hair cell receptor potential have identified at least two low pass filters that may contribute to the loss of timing information at high frequencies (Kidd and Weiss 1990), however all previous models ignore, or greatly simplify, the presynaptic details of the afferent synapse (Kidd and Weiss 1990; Roberts 1994; Issa and Hudspeth 1996; Hall et al. 1997; Lumpkin and Hudspeth 1998; Sumner et al. 2002). In particular, it has been suggested that the endogenous calcium buffer is fast, and that this aids in maintaining temporal acuity of synaptic transmission (Roberts 1994; Edmonds et al. 2000). A handful of recent experimental results provide a rigorous backbone on which to consider the following presynaptic details in the bullfrog hair cell: the distribution of synaptic vesicles at the active zone (Lenzi et al. 1999; Lenzi et al. 2002), the kinetics of calcium dependent exocytosis (Beutner et al. 2001), and the time course of voltage clamp initiated exocytosis in a hair cell (Parsons et al. 1994; Moser and Beutner 2000). I will create a software-based computational model to carry out the following:

- A. **Test the hypothesis that weak calcium buffering mediates exocytosis at this synapse**
- B. **Test the hypothesis that weak calcium buffering does not degrade the temporal fidelity of exocytosis at this synapse compared to the response under strong buffer conditions**

### **Aim 2. Examines how component variability affects information enhancement across the tonotopic axis of the cochlear nucleus.**

The auditory nerve encodes information regarding the timing, frequency, and amplitude of the acoustic waveform. Neurons in the cochlear nucleus enhance specific aspects of the auditory nerve's representation: precision of timing by bushy cells (Joris et al. 1994), dynamic range and duration of spectrum by t-stellate cells (Blackburn and Sachs 1990; Recio and Rhode 2000), frequency of amplitude modulation over an extended intensity range by octopus cells (Frisina et al. 1990), and detection of spectral features by fusiform and giant cells (Spirou and Young 1991). Enhancements by these various cell types are robust despite cell-to-cell component variability such as strength of synaptic inputs, distribution of active conductances (Rothman and Manis 2003a) and response profiles of local interneurons (Wickesberg et al. 1994; Golding and Oertel 1996). Using a silicon-based computational model, I propose to examine:

- A. **Phase locking by bushy cells.** Bushy cell currents exhibit a wide range of activation thresholds, time constants, and maximal conductances (Rothman and Manis 2003a). Similarly, the response profiles of bushy cell inhibitory inputs display variability (Godfrey et al. 1975; Blackburn and Sachs 1989; Kopp-Scheinflug et al. 2002). How do bushy cells consistently enhance ANF phase locking despite component variability? How do the two identified sources of inhibition differentially affect spike timing in these cells?
- B. **Recurrent network contribution to spectrum representation by t-stellate cells.** Recurrent networks exist between t-stellate, d-stellate, and tuberculoventral cells, all of which are driven by the auditory nerve (Wickesberg and Oertel 1988; Oertel et al. 1990; Zhang and Oertel 1993; Doucet and Ryugo 1997). These networks may act to

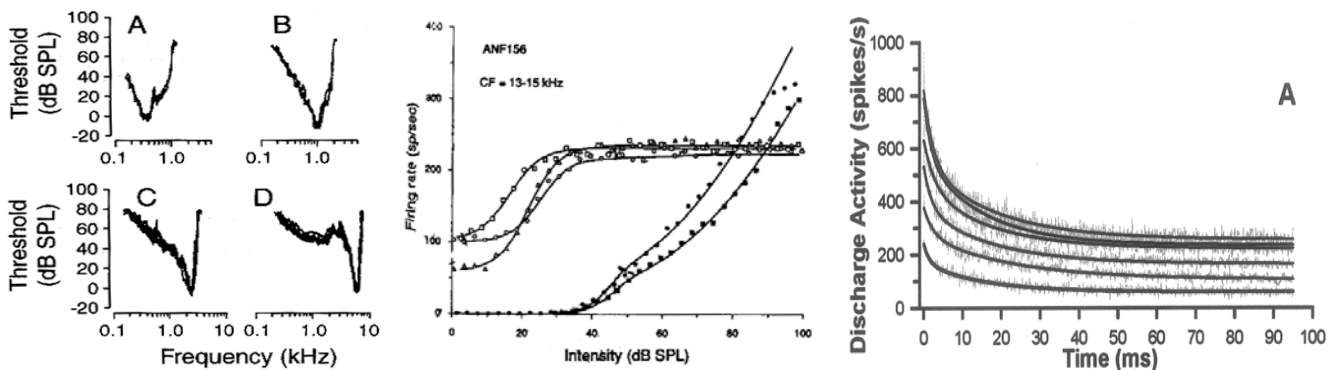
enhance t-stellate representation of spectrum (Eriksson and Robert 1999), though they probably sharpen the temporal and spectral sensitivity as well. How do network properties affect t-stellate response characteristics in light of component variability? Is the t-stellate's consistent first spike latency a byproduct of recurrent networks, membrane specializations, or merely a result of temporal acuity in the ANF?

- C. **Pitch extraction by octopus cells.** Octopus cells have distinct morphology and expression of conductances (Golding et al. 1995), though their functional significance is not clear. Octopus cells encode the pitch of pure tones and speech; they entrain to pure tones less than 800 Hz, and enhance ANF representation of amplitude modulation (Blackburn and Sachs 1990). Possibly these cells encode all aspects of pitch, including the pitch of harmonic tones. How does variation in dendritic filtering affect these cells' ability to detect onsets and extract pitch?
- D. **Specificity of spectral feature detection in fusiform and giant cells.** These dorsal cochlear nucleus principle cell types receive excitatory inputs from the auditory nerve and t-stellate cells, and strong inhibitory inputs from both wideband and narrowband interneurons (Zhang and Oertel 1994). The relative contribution of each input to a DCN principle cell shapes that cell's response profile (Spirou et al. 1999; Davis and Young 2000). How then does variability of each contributing cell type accumulate within the DCN circuit? How does variability affect these cells respond to spectral notches?

### III. Background and Significance

#### Encoding Information at the Auditory Periphery

The cochlea encodes information about the frequency, amplitude, and timing of the acoustic wave. Mechanical resonance of the basilar membrane distributes stimulus frequencies along its length. Inner hair cells within the Organ of Corti transduce the resulting movement of their stereocilia to a receptor potential that causes exocytosis of synaptic vesicles. Neurotransmitter from these vesicles excites spiral ganglion neurons, which make up the auditory nerve. Auditory nerve fibers (ANFs) transmit all auditory information to downstream auditory nuclei, the first of which is the cochlear nucleus. Due to the specificity of basilar membrane resonance, individual ANFs are sensitive to a limited range of acoustic frequency. The frequency tuning curves of four fibers innervating different regions of the basilar membrane are shown in Figure 1 (left). These curves are constructed by stimulating with pure tones of different frequencies and intensities (dB SPL) while recording spikes from an individual fiber. Threshold is the sound intensity required to increase spike rate at the neuron's most sensitive frequency, its characteristic frequency (CF), which is identified as the lowest point in the dip of each tuning curve. The tuning curves are narrow near threshold but widen with increasing sound intensity as frequency selectivity of the basilar membrane diminishes. High frequencies are absorbed at the beginning of the basilar membrane (base), such that all low frequency sounds essentially travel past high frequency regions of the membrane. This leads to the asymmetry apparent in the bottom two tuning curves (labeled C and D). Frequency information is spatially distributed across the tonotopic array of auditory nerve fibers. In cat, approximately 3,000 inner hair cells are contacted by 50,000 auditory nerve fibers (Liberman et al. 1990; Ryugo and Sento 1991), four to five times the numbers found in mice (700 and 10,000, Ehret 1979; Keithley and Feldman 1983).

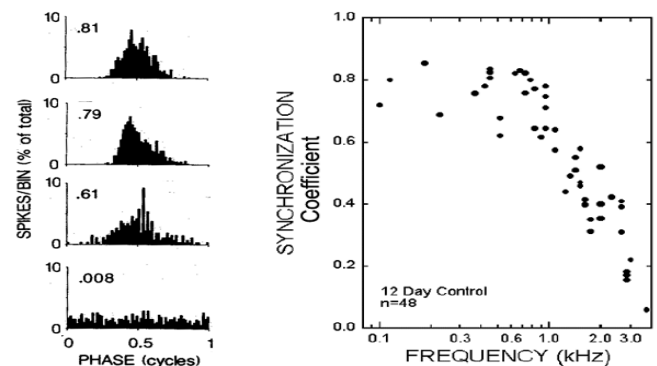


**1. Frequency selectivity and firing rate characteristics in auditory nerve fibers** (left) Frequency tuning curves for 4 different auditory nerve fibers measured from cat. A fiber's characteristic frequency (CF) is the lowest point of its tuning curve. Fibers in A-D have CFs increasing from 0.35 to 7 kHz. From Liberman and Mulroy (1982). (middle) Rate intensity curves for 3 HSR and 2 LSR fibers. Measured from Guinea pig using 100 ms CF tones, 20 to 40 repetitions per intensity. From Muller and Robertson (1991). (right) Spike rate adaptation normalized and averaged from 20 fibers stimulated with a 100ms pure tone at CF ranging from 10 to 60 dB above CF threshold. Measured in chick in Dr. Saunders' laboratory.

Individual ANFs convey information about the amplitude of the acoustic wave in their firing rates. Fibers are classified by their firing rates in the absence of a sound stimulus; low spontaneous rate (LSR) fibers fire less than 0.5 Hz, medium spontaneous rate (MSR) fire between 0.5 and 18 Hz, and high spontaneous rate (HSR) fibers fire faster than 18 Hz (Lieberman and Kiang 1978). With increasing acoustic intensity ANF spike rates increase, eventually saturating at rates up to 300 Hz (Sachs and Abbas 1974). Figure 1 (middle) compares spike rate versus sound intensity for several representative HSR and LSR fibers. Stimuli were pure tones at each fiber's CF. HSR fibers are sensitive to low sound levels, but encode a narrow range of intensity levels due to firing rate saturation. LSR fibers encode a wide range of intensity levels, but are insensitive to intensities less than 30 dB SPL. In cat the distribution of low, medium and high spontaneous rate fibers is approximately 16, 24, and 60% (Lieberman 1988). The ANF representation of waveform amplitude is not stationary. ANFs show spike rate adaptation during the course of an acoustic stimulus, presumably due to depletion of presynaptic vesicles within the inner hair cell (Geisler 1998). Figure 1 (right) shows the average time course of adaptation for 20 fibers stimulated by CF tones with intensity ranging from 10 to 60 dB above CF threshold.

Individual ANFs convey timing information regarding the onset, duration, and phase of the acoustic wave. For LSR and MSR fibers, the onset of sound is encoded by the timing of their first evoked spike, HSR fibers encode onset with the timing of their rate increase. The duration of an acoustic stimulus is encoded by the duration of increased firing rate in an ANF. In contrast, the phase of an acoustic wave is encoded by the precise timing of individual spikes. At low frequencies, ANFs entrain with the stimulus waveform, a phenomenon called phase locking. Phase locking is visualized using a period histogram which compares when spikes occurred with respect to stimulus period (Figure 2). The degree of phase locking is quantified by the synchronization coefficient (SC), which may be computed as the magnitude of the vector sum of all phase components in a normalized period histogram (Goldberg and Brown 1969). SC values range between 0 and 1.0, 0 representing no phase locking (flat period histogram) and 1.0 representing perfect phase locking (all spikes in a single bin of the phase histogram) and 1.0 occurring when all spikes line up in a single bin. Phase locking increases with sound intensity but saturates at a maximum value for each fiber. The max SC of ANFs rarely exceeds 0.8, and declines with increasing characteristic frequency. Figure 2 (right) shows max SC versus CF in the chick for CFs ranging from 0.1 – 4 kHz. Notice the sharp decline in SC at frequencies above 1 kHz, which is attributed to low-pass filtering during signal transduction by the inner hair cell (Kidd and Weiss 1990).

**2. Phase locking in auditory nerve fibers** (left) Period histogram of four different ANFs from the cat. Each fiber was stimulated with CF tones sufficient to elicit max SC, which ranges from 0.81 to 0.008 for these histograms. CF (Hz) and dB SPL for each fiber (top to bottom): 670,8; 340,23; 2830,17; 7100,35. From Joris et al (1994). (right) Plot of max SC values versus fiber CF for 48 chick ANFs. Notice the sharp decline in SC above 1 kHz. Data from Dr. Saunders' laboratory.



The inner hair cell afferent synapse must release synaptic vesicles with temporal precision to elicit phase locking in the ANF. Additionally, it must be able to support prolonged release to encode long duration sounds. The inner hair cell, like retinal sensory and bipolar cells, contains ribbon synapses; anatomical specializations which may enable the synapse to address both of these requirements. A ribbon synapse is a pre-synaptic specialization in which an electron dense structure called the synaptic ribbon or dense body is anchored at each putative active zone, where it is surrounded by synaptic vesicles. In frog, the hair cell dense body and associated vesicles have been reconstructed using electron tomography (Lenzi et al. 1999; Lenzi et al. 2002). Its 19 dense bodies (Roberts et al. 1990) are approximately 400 nm in diameter, with an average of 385 synaptic vesicles (40nm diameter) tethered to each. The dense body may tether vesicles close to the membrane to facilitate rapid fusion when calcium channels at the active zone open in response to membrane depolarization (Parsons and Sterling 2003). Additionally, the large supply of vesicles tethered locally by the dense body may serve as an immediate reserve to maintain sustained rates of exocytosis (Geisler 1998; Parsons and Sterling 2003). The depletion of this immediate reserve has been suggested to play a role in ANF spike rate adaptation (Eisen et al. 2004). Experimental evidence precisely defining the role of the dense body in these various physiological responses is currently lacking.

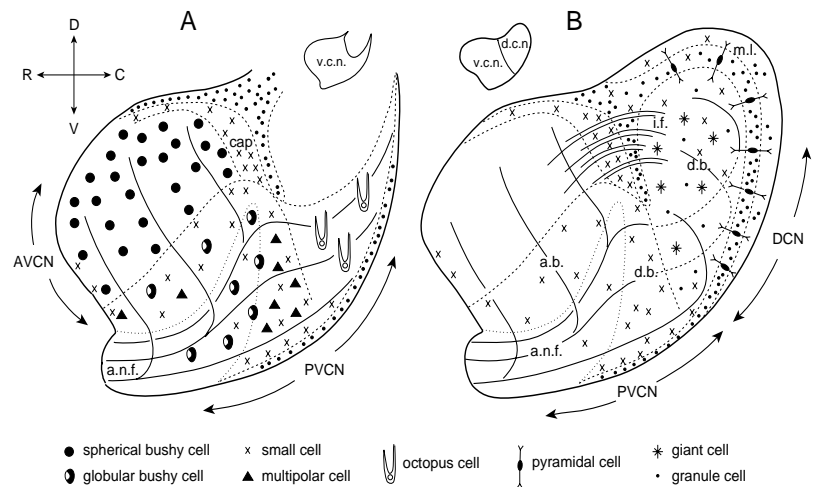
### **The cochlear nucleus: Architecture, Response Profiles, and Output Paths**

The auditory nerve bifurcates and terminates within the cochlear nucleus. Figure 3 schematizes a lateral view of the cochlear nucleus, which reveals the pathway of the auditory nerve and distribution of several distinct cochlear nucleus cell types. The auditory nerve root enters at the antero-ventral edge of the nucleus, where it sends a descending branch to the ventral cochlear nucleus, and an ascending branch to the dorsal cochlear nucleus. The various cell types labeled in Figure 3 are identified by their distinct anatomies, particularly their dendritic morphology. *In vivo* recordings of single cells have identified several distinct responses to sound (Godfrey et al. 1975; Blackburn and Sachs 1989), which have been correlated to specific cell types with single cell labeling after recording (Smith and Rhode 1987; Smith et al. 1991; Smith et al. 1993). *In vitro* recordings from brain slices (Oertel 1985) and dissociated cell culture (Manis and Marx 1991) have further detailed the conductances and local connectivity of most major cell types in the nucleus.

Only six cochlear nucleus cell types project axons to downstream auditory nuclei. Four of these emerge from the ventral cochlear nucleus: the spherical and globular bushy, t-stellate (also called t-multipolar) and octopus cells. Fusiform (also called pyramidal) and giant cells send projections out of the dorsal cochlear nucleus. Figure 4 shows how these cells response to sound (left column, *in vivo*) and to current injection (right column, *in vitro*). Each cell type has quite distinct responses to each type of stimulus. Variable responses to current injection are indicative of differences in membrane time constants and active conductances, while responses to sound are further shaped by differences in synaptic connectivity with both the auditory nerve and local interneurons. In the preliminary results section I describe in detail the combination of conductances and synaptic connectivity responsible for shaping the bushy cell response. Detailed descriptions for other cochlear nucleus cell types will be provided in the body of my thesis, and only briefly summarized here.

### 3. Lateral view of the cat cochlear nucleus

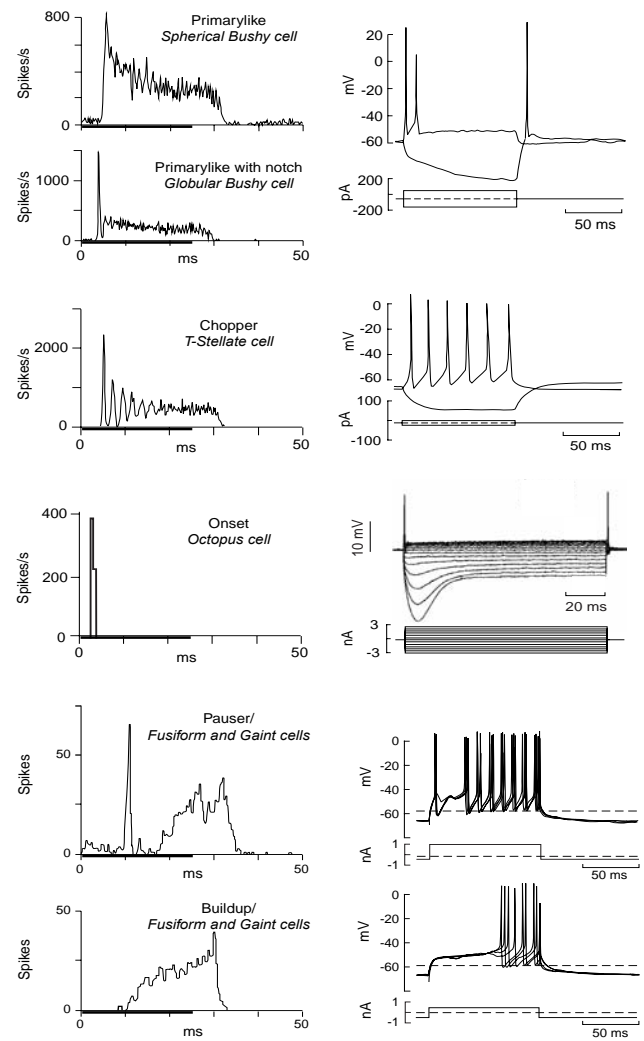
Schematic view of two saggital sections of a cat's left cochlear nucleus, the right schematic more medial than the left. The nerve root enters at the antero-ventral pole of the nucleus and bifurcates in the ventral cochlear nucleus. Thick descending fibers innervate bushy and stellate (multipolar) cells in the anterior ventral cochlear nucleus (avcn) while thin ascending fibers innervate the octopus cells of the pvcn, and several cell types in the dorsal cochlear nucleus. Both ascending and descending fibers are distributed tonotopically, those innervating high frequency regions of the cochlea are more rostral in both cases. Modified from Osen (1970).



**Bushy and octopus** cells both have low input resistances due to a combination of low threshold potassium ( $K_{LT}$ ) and hyperpolarization activated mixed cation current ( $I_H$ ) active at rest (Bal and Oertel 2000,2001; Rothman and Manis 2003a). Their short membrane time constants cause them to spike only once or twice during current injection. **Spherical bushy** cells receive 1-4 calyceal synaptic inputs via endbulbs on their cell bodies (cat, Brawer and Morest 1975; rat, Nicol and Walmsley 2002). Excitation by a single endbulb *can* elicit a bushy cell spike, so the endbulbs are super-threshold synapses, though desensitization, refractory periods and inhibition may prevent spiking at times (Kopp-Scheinflug et al. 2002). Because each synapse is super-threshold, and the number of endbulb inputs is limited, the spherical bushy response closely resembles that of the auditory nerve (primarylike) in terms of temporal jitter and spike rate adaptation (compare spherical bushy PSTH in Figure 4 with the ANF PSTH in Figure 1, right). **Globular bushy** cells receive up to 50 smaller endbulb inputs (cat, Liberman 1991; Ostapoff and Morest 1991) that are also presumably super-threshold. This large set of strong inputs reduces jitter in the globular bushy cell latency (to first spike) by increasing the likelihood that one of its inputs will exhibit the minimal latency possible. Their consistent first spike latency results in an initial peak in their PSTH, which is followed by a notch due to aligned post-spike refractory periods. **Octopus** cells have a lower input resistance than bushy cells, and receive approximately 60 ANF inputs that are sub-threshold, as excitation at a single input is not enough to elicit a spike (Golding et al. 1995). Their onset response reflects the coincidence of many ANF spikes synchronized to the onset of sound, though at frequencies less than 800 Hz their response is phase locked rather than purely onset (Rhode and Smith 1986). **T-stellate cells** do not appreciably express  $K_{LT}$  and therefore spike regularly with both current injection and auditory nerve activation (Blackburn and Sachs 1989; Rothman and Manis 2003a). They receive input from five ANFs on average in the mouse (Ferragamo et al. 1998). The latency of their first spike is very consistent, such that a large peak occurs at the beginning of their PSTH. The chopping response is due to consistent first spike latency and relatively consistent inter-spike-intervals. **Fusiform and giant** cells also do not appreciably express  $K_{LT}$ , but have significant calcium currents and calcium activated potassium currents (Kanold and Manis 1999; Molitor and Manis 1999). Their response to current injection is variable, which may reflect a shifting balance between these conductances. Their responses to

sound are significantly shaped by both excitatory and inhibitory inputs from other cell types (Nelken and Young 1994; Zhang and Oertel 1994).

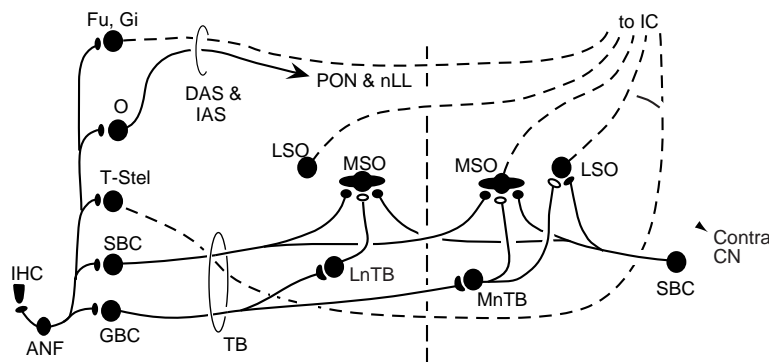
**4. In vivo and in vitro descriptions of the six projection neurons from the cochlear nucleus** (left column) Post-stimulus time histograms (PSTH) describe the in vivo response of each neuron type to sound. Pure tones were repetitively presented at each neuron's CF for 25ms to create the histograms (indicated by bar on each abscissa). Primarylike response resembles the PSTH from auditory nerve fibers (see Figure 1, right). Primarylike with notch is similar, but has a sharply timed first spike followed by a notch from spike refractoriness. Chopper response results from a consistently timed onset spike followed by a relatively fixed inter-spike-interval. Onset response characterized by very precise first latency, and little to no additional spikes per stimulation. Octopus cells exhibit an onset response to high frequency tones, but phase lock to tones up to 800 Hz. Pauser response shows first spike followed by 5 – 10 ms pause, and buildup spike probability increases with stimulus duration. Fusiform and giant cells exhibit either pauser or buildup response profiles, note their PSTH ordinate is in units of spikes rather than spikes per second. (right column) In vitro responses to current injection for each neuron type, with stimulus protocol below each trace. A wide range of input currents are required to elicit a spike from each neuron type, with octopus and bushy cells requiring the most current to elicit a spike. The traces from fusiform, giant, and t-stellate cells required hyperpolarizing current to inhibit spontaneous activity. Spherical and globular bushy cells exhibit similar responses to current injection, so a single trace is shown for both. Figures adapted from the following sources: Primarylike and chopper (PSTH, Blackburn and Sachs 1989; in vitro, Manis and Marx 1991), octopus (PSTH, Kiang et al. 1973; in vitro, Golding et al. 1999), fusiform (PSTH, Godfrey et al. 1975; in vitro, Manis 1990).



The ANF is glutamatergic and its synapses in the cochlear nucleus are excitatory (Isaacson and Walmsley 1995; Gardner et al. 1999), but all projecting neurons in the cochlear nucleus, except for octopus cells, additionally receive glycinergic inhibitory inputs from two local interneurons. Wideband inhibition comes from d-stellate cells in the ventral cochlear nucleus (Golding and Oertel 1997; Doucet et al. 1999) and narrowband inhibition comes from tuberculoventral cells (also called corn or vertical cells) in the dorsal cochlear nucleus (Wickesberg et al. 1991). The bandwidth of inhibition is correlated with the ANF innervation pattern of these two cell types; d-stellate dendrites are perpendicular to the ANF such that it spans a wide range of CFs, while tuberculoventral dendrites are parallel to the ANF. The dorsal cochlear nucleus also receives non-auditory inputs via granule cells, whose axons become parallel fibers that course perpendicular to the auditory nerve. Parallel fibers affect both of the dorsal cochlear nucleus

projection cell types through a population of interneurons, though fusiform additionally receive direct innervation by parallel fibers with synapses that exhibit long term plasticity (Golding and Oertel 1997; Fujino and Oertel 2003).

Auditory information exiting the cochlear nucleus travels in several parallel pathways, and then converges at the inferior colliculus before moving into the auditory thalamus and cortex (Figure 5). The other auditory brainstem nuclei include the medial superior olive (MSO), the lateral superior olive (LSO), the medial nucleus of the trapezoid body (MnTB), and both the ventral and dorsal nuclei of the lateral lemniscus (VNLL and DNLL). Spherical bushy cells from both sides of the brain innervate the MSO, where interaural timing differences are computed (ITD, Goldberg and Brown 1969). Globular bushy cells innervate the contralateral MnTB, which sends inhibitory inputs to the MSO and LSO. Spherical bushy cells excite the LSO from the ipsilateral side, enabling computation of interaural level differences (ILD, Boudreau and Tsuchitani 1970). The outputs from the MSO and LSO are therefore binaural, and encode cues for horizontal sound localization (Yin 2002). The largely monaural VNLL receives inputs from bushy, t-stellate, and octopus cells. Its tonotopic organization is concentric with high frequencies represented in the center and low frequencies about the core in both bat (Covey and Casseday 1991) and rat (Merchan and Berbel 1996; Malmierca et al. 1998), suggesting the role of this nucleus in temporal pattern recognition (Oertel and Wickesberg 2002). The connectivity and computation of the DNLL is not clear, though it receives binaural inputs from the ipsilateral MSO, both LSO nuclei, and the contralateral DNLL (Schwartz 1992). The inferior colliculus primarily receives inputs from the contralateral cochlear nuclei, and the ipsilateral MSO, LSO, VNLL and DNLL. It receives descending inputs from the auditory thalamus and non-auditory inputs from both somatosensory and motor systems. Its tonotopy presents as isofrequency lamina, each isofrequency sheet providing a channel of narrow bandwidth information processing, with a perpendicular axis allowing for cross spectra integration (Casseday et al. 2002). *In vivo* recordings have suggested topographical axes encoding amplitude modulation frequency (Schreiner and Langner 1988), harmonic pattern detection (Portfors and Wenstrup 2001,2002), and non-harmonic spectral feature detection (Davis et al. 2003).



5. *Auditory Brain Stem Circuit: Outputs from the cochlear nucleus* From Young and Oertel (2004).

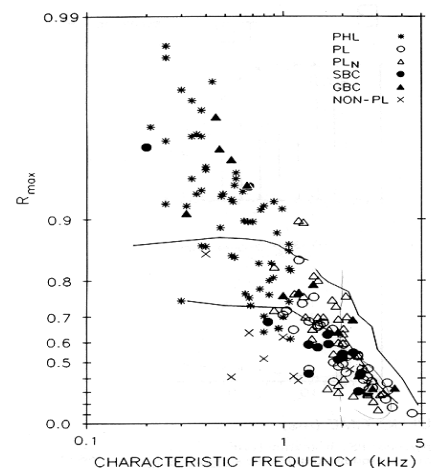
### Information Enhancement within the cochlear nucleus

*Globular bushy cells phase lock with higher precision than the auditory nerve.* The precise encoding of the acoustic waveform phase is required for sound localization in the horizontal plane (Yin 2002), and enhances interpretation of communication signals such as speech (Van Tasell et al. 1987). Joris and colleagues measured the

maximum SC of 176 fibers within the trapezoid body of the cat (Joris et al. 1994), where spherical bushy, globular bushy, and t-stellate axons project to the contralateral side of the brain. Their results, when compared to cat ANF maximum SCs (Johnson 1980), reveal substantial increases for characteristic frequencies less than 2 kHz (Figure 6). Based on spontaneous rates, Joris and colleagues argued that most of the high SC fibers originated from globular bushy cells, which have been shown to have lower spontaneous rates than spherical bushy cells with low characteristic frequencies (Smith et al. 1991; Smith et al. 1993).

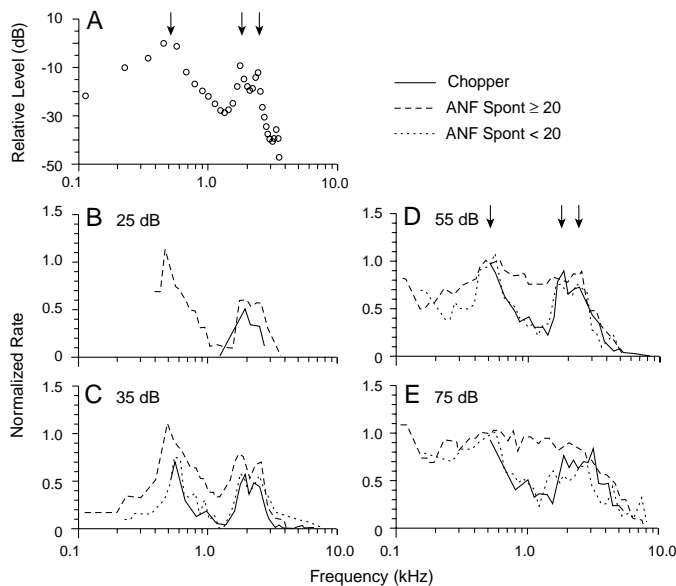
Based on the *in vitro* characterization of bushy cells (Manis and Marx 1991; Rothman and Manis 2003a), Rothman, Manis and Young (Rothman et al. 1993; Rothman and Young 1996) created a conductance based software model in attempts to explain the phase locking enhancement of globular bushy cells. Varying number and strengths of auditory nerve inputs, as well as the level of constant background inhibition, they found that 15 super-threshold inputs with a steady state inhibition achieved the best matching of both phase locking and spontaneous rates (Rothman and Young 1996). Generally, the parameter space that accounted for highly synchronous phase locking resulted in inaccurately high spontaneous rates. To date, a comprehensive model which accounts for all aspects of the globular bushy cell response has yet to be created (Young and Oertel 2004).

**6. Enhanced phase locking by bushy cells** *Solid lines indicate upper and lower boundaries of the range of maximum SC ( $R_{max}$ ) reported for cat ANFs (Johnson 1980). Recordings from 176 fibers within the trapezoid body reveal the phase locking ability of bushy and t-stellate cells. Filled symbols indicate anatomically labeled spherical bushy cells (SBC,  $N=16$ ) and globular bushy cells (GBC,  $N=13$ ). Unfilled symbols indicate unlabeled cells classified by their response profile: phase locked (PHL), primarylike (PL) and primarylike with notch (PLN). Phase locking in the trapezoid body assessed from 64 repetitions of a 25ms CF tone. Ordinate is scaled by the log of  $1-R_{max}$  to separate highly phase locked responses. From Joris et al (1994)*



*T-stellate cells encode relative sound spectrum energy over a wider range of absolute intensity levels than individual auditory nerve fibers, and the t-stellate representation is more consistent irrespective of sound duration compared to the auditory nerve.* A representation of spectrum that is robust with respect to absolute sound intensity is important for interpretation of communication signals such as speech (Remez et al. 1981; Young and Oertel 2004). Single unit recordings have been used to characterize how the auditory system encodes speech stimuli at the level of the auditory nerve (Sachs and Young 1979; Young and Sachs 1979; Delgutte and Kiang 1984a,d,b,c) and cochlear nucleus (Blackburn and Sachs 1990; Recio and Rhode 2000). Blackburn and Sachs (1990) recorded the spike rates of individual t-stellate (chopper) and ANF fibers when evoked by the vowel /ε/, then normalized and averaged those rates at each CF (Figure 7). They characterized ANFs at either HSR or medium-low spontaneous rate (<20 Hz). At low sound levels, only t-stellates and HSR fibers show increased firing rates at the sound formants. At high sound levels, only t-stellates and medium-low spontaneous rate ANFs show firing rate peaks at the formants as HSR fibers are saturated (see Figure 1, middle). The enhanced range over which t-stellate cells encode spectral peaks was recently

verified with six different vowel stimuli (Recio and Rhode 2000). The results suggest t-stellate cells are innervated by both medium-low and HSR fibers, though how they avoid saturation by their HSR inputs at moderate intensities is unclear.



### 7. Enhanced representation of sound spectrum by t-stellate cells

(A) The spectrum of the vowel /ε/. Arrows indicate formants, spectral peaks resulting from resonance within the vocal tract, which are used in the identification of vowel sounds. (B – E) Representation of /ε/ by populations of t-stellate (chopper), medium-low (Spont < 20), and high (Spont > 20) spontaneous rate ANFs with CFs ranging from 0.1 to 10 kHz. Lines are computed by a moving average ( $1/4$  octave wide) of the normalized response rate from hundreds of each neuron type, where a normalized rate of 1 means the neurons are firing at their maximum recorded rates. Rates were computed from the last 300 ms of each 400ms stimulus. Note that 75dB is a conversational sound level. From Blackburn and Sachs (1990).

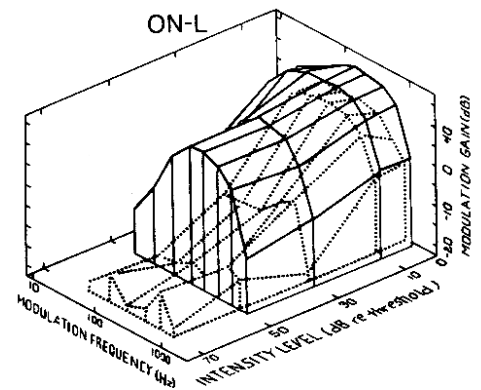
Complex communication sounds include not just steady state spectral peaks, but transitions of those peaks with respect to time. Due to adaptation in the auditory nerve, its representation of relative intensity levels may change after transitions in which some spectral peaks shift while others remain constant. T-stellate cells compensate for auditory nerve adaptation, thereby faithfully representing relative spectral energy irrespective of previous sound stimuli. This compensation is apparent when examining the average spike rate of chopper neurons throughout the duration of a long stimulus compared to the adaptation found in the auditory nerve (Pfeiffer 1966; Blackburn and Sachs 1989, compare Primarylike and Chopper response in Figure 4). Besides innervation by both medium-low and HSR auditory nerve fibers, t-stellate cells send axon collaterals locally, forming a recurrent excitatory network which likely contributes to their compensation for ANF adaptation. T-stellate cells are also part of a recurrent inhibitory network formed between d-stellate, tuberculoventral cells and themselves (Zhang and Oertel 1994). Modeling efforts have indicated the importance of dendritic filtering in eliciting the chopper response (Banks and Sachs 1991). Theoretical considerations suggest the enhanced dynamic range of t-stellate cells is mediated by their inhibitory inputs, and either results from an emergent property of their recurrent connections (Shamma 1998; Eriksson and Robert 1999; Wilson 1999), or from explicit connectivity of both auditory nerve and inhibitory inputs along their dendritic arbor (Lai et al. 1994).

*Octopus cells encode amplitude modulated sounds over a wider range of modulation frequencies and average sound intensity levels than the auditory nerve.* Psychophysical measurements indicate the importance of temporal information, such as amplitude modulation, in speech interpretation (Van Tasell et al. 1987; Smith et al. 2002). Amplitude modulated sounds are perceived to have a pitch equal to their modulation frequency. Glottal vibrations during voiced speech incur amplitude modulation at a relatively fixed frequency per individual, ranging from 60 Hz for

a baritone adult male up to several hundred hertz for young children (Hollien and Shipp 1972), which may aid in discriminating speech in a noisy environment (the cocktail party problem, Bregman et al. 1990). In addition to encoding the pitch of amplitude modulated sounds, octopus cells may encode the pitch of harmonically related tones (Kim et al. 1986; Cariani and Delgutte 1996b,a) based on their wideband auditory nerve inputs (Rhode and Smith 1986) and extremely low input resistance which mediates coincidence detection (Golding et al. 1995).

Several studies have used amplitude modulated sounds to characterize the temporal response properties of neurons in the auditory nerve (Evans 1978; Javel 1980; Palmer and Evans 1982) and cochlear nucleus (Frisina et al. 1990; Rhode and Greenberg 1994). Enhancement of amplitude modulation is found in all cells of the cochlear nucleus, though among the projection neurons it is most pronounced in octopus, followed by t-stellate cells. Figure 8 demonstrates the effectiveness of octopus (On-L) cells at encoding amplitude modulated tones relative to the auditory nerve across a range of modulation frequencies spanning 20 to 1000 Hz. Frisina et al (1990) did not anatomically identify the On-L neurons as octopus, though octopus cells can have On-L profiles (Rhode and Greenberg 1994), and have been morphologically and physiologically identified enhancers of amplitude modulation in other recordings (Blackburn and Sachs 1990; Rhode and Greenberg 1994). In Figure 8, neural representation of amplitude modulation was quantified as modulation gain, which compares modulation depth of the neuron's PSTH to that of the stimulus (see Figure legend for details). Notice that both cells exhibit decreasing ability to encode amplitude modulation depth as average sound intensity increases and as modulation frequency increases.

**8. Enhanced representation of amplitude modulation in octopus cells** *Mongolian gerbils were presented with amplitude modulated, 100ms pure tones at each neuron's CF. Both the intensity level and modulation frequency were varied while stimulus modulation depth was held constant at 35%. Fourier analysis of stimulus waveform and response PSTH were used to compute modulation depth, defined as the modulation frequency component / average response. Modulation gain quantifies the relative modulation depths of the neural response and sound stimulus, and is defined as  $20 \log_{10}(\text{response} / \text{stimulus modulation depth})$ . The surface delineated with dotted lines shows a representative HSR ANF's modulation gain with respect to modulation frequency and sound intensity. Onset-locker (octopus or globular bushy cell) neurons exhibit increased modulation gain relative to the auditory nerve across all parameter values. From Frisina et al (1990).*

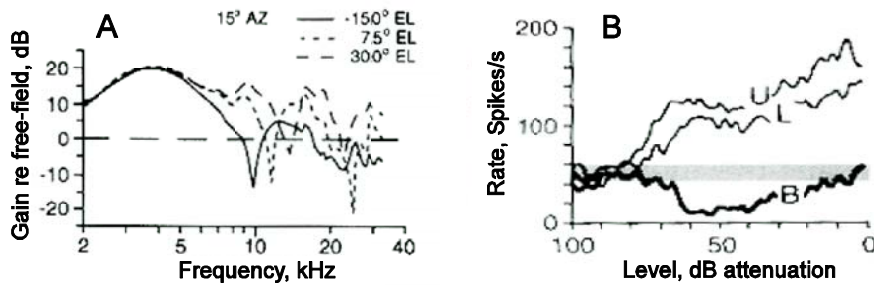


*Fusiform and giant cells encode specific, sharp spectral features that are not conveyed by single auditory nerve fibers alone.* The detection of specific, sharp spectral features may be important for vertical sound localization, or signaling the rest of the auditory system that interesting acoustic information is located at a particular frequency (Nelken and Young 1994). Sounds are filtered by our heads and outer ears based on their angle of incidence, creating Head Related Transfer Functions (HRTFs) that are depended on the location of a sound source. Behavioral studies with cats show an increase in sound localization performance when noise in the frequency band between 5 and 18 kHz is presented (Huang and May 1996). Rice and colleagues (1992) characterized HRTFs for different sound source locations in cats, and found a prominent notch within this frequency range that shifts with sound source location

(Figure 9a). *In vivo* recordings from fusiform and giant cells show an inhibitory sensitivity to notch frequency. These neurons are inhibited by HRTF-filtered noise when the notch frequency is centered at their CF, though they are excited by broadband noise (BBN) or HRTF-filtered noise with the notch either above or below their CF (Figure 9b).

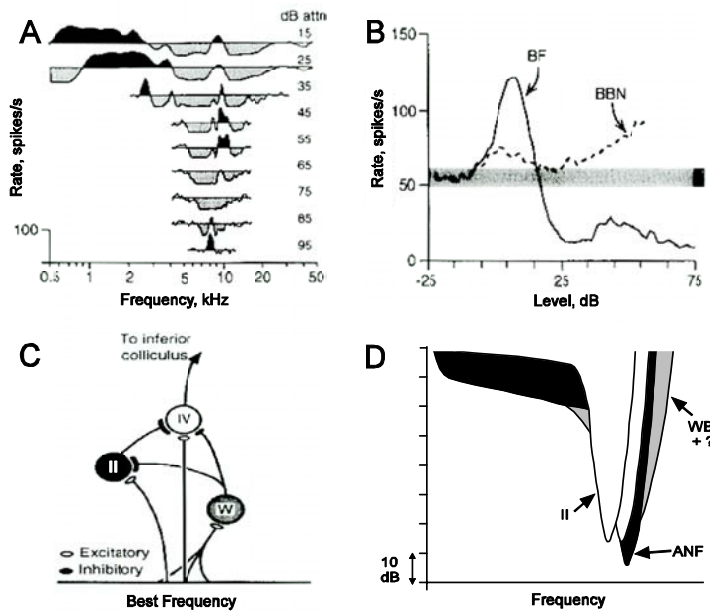
### 9. Spectral feature detection by fusiform and giant cells used for monaural sound localization

(a) HTRFs from a cat for three sound source locations. White noise was emitted from a speaker held at various locations, and the frequency response at the cat's right eardrum was measured.



Prominent notch between 8 – 18 kHz shifts to higher frequencies as sound source elevation increases. From Rice et al (1992). (b) Rate intensity functions of a fusiform or giant cell when stimulated with HRTF-filtered noise stimuli. Stimuli are similar to those shown in a, with notch frequencies positioned at the neuron's characteristic frequency (B), and above or below it (U, L). Sound level given as attenuation, but spectrum level was the same for the three traces. Shaded bar indicates spontaneous discharge rates for this neuron. Notice a prominent inhibition (decrease in rate) when the notch is centered at best frequency, but excitation otherwise. This neuron is excited by BBN at all levels, and inhibited by tones at its characteristic frequency at high sound levels (Figure 10b). From Young and Davis (2002).

Notch detection in the dorsal cochlear nucleus is computed via interaction of excitatory and inhibitory inputs to the fusiform and giant cells. Fusiform and giant cells typically have a type IV response map in unanaesthetized cat, shown in Figure 10a (Young and Brownell 1976; Young 1980; Rhode and Kettner 1987). Type IV response map features include excitation at low stimulus levels near the neuron's characteristic frequency and inhibition over most of the response area at moderate to high stimulus levels. This response characteristic suggests low threshold excitatory innervation at best frequency coupled with high threshold wideband inhibition (WBI). Despite inhibition over a wide range of pure tone frequencies and intensities, type IV neurons are excited by BBN at all sound levels (Figure 10b). Cross correlation of spikes from a type IV neuron and type II neuron indicate these cells also receive narrowband inhibition (Voigt and Young 1980). The compilation of these and other experimental evidence lead to the proposal of the network shown in Figure 10c, with conceptual tuning curves shown in Figure 10d (Spirou and Young 1991). In this model, excitation by BBN is due to release of narrowband inhibition by type II inputs, which themselves are inhibited by WBI. Subsequent experiments have identified the two inhibitory interneurons as tuberculoventral (type II, Voigt and Young 1980; Rhode 1999) and d-stellate (wideband inhibitors, Smith and Rhode 1989; Oertel et al. 1990; Doucet et al. 1999). Computational models including the three cell types proposed by Spirou and Young can successfully account for most properties of type IV neurons in the DCN (Blum et al. 1995; Hancock et al. 1997; Blum and Reed 1998). Integration of non-auditory inputs involves an additional pathway through the parallel fibers and several other interneurons not shown (Young and Davis 2002).



**10. Spectral feature detection by fusiform and giant cells (type IV response)** (a) Typical response map for dorsal cochlear nucleus projection cells (type IV response). Pure tones ranging from 4 – 50 kHz were presented at various intensity levels (represented in dB attenuation in this plot). Spontaneous rate of this neuron is approximately 100Hz, as show in ordinate scale, and is represented as horizontal line for each intensity level. Excitatory and inhibitory responses are shown in black and gray. CF is roughly 8 kHz. (b) Rate intensity functions for a pure tone at CF and BBN. Gray horizontal region indicates the range of spontaneous rates of this neuron. Ordinate delineates spike rate for pure tone stimulus only, BBN response was shifted down for comparison. Sound levels are given as dB SPL. Compare these responses to those from notch noise in Figure 9b. (c) Neural circuit model proposed by Spirou and Young (1991). The bottom horizontal line represents the tonotopic array of auditory nerve fibers. Type II neurons (II, tuberculoventral) receive narrowband ANF input, and inhibit type IV. WBI neurons (W, d-stellate) receive wideband ANF input, and inhibit both type II and type IV neurons. Type IV neurons receive inhibition from both interneurons, and narrowband excitation from ANF. (d) Schematic representation of the frequency tuning curves of excitatory and inhibitory inputs to a type IV neuron. The schematic of ANF and type II tuning curves resemble those in Figure 1, right. Notice the threshold intensities of each input, at low sound levels, the cell only receives excitatory input from the ANF, soon followed by inhibition from type II inputs, and inhibition by WBI at even higher intensity levels. Data in a and b from Nelken and Young (1994).

Summary

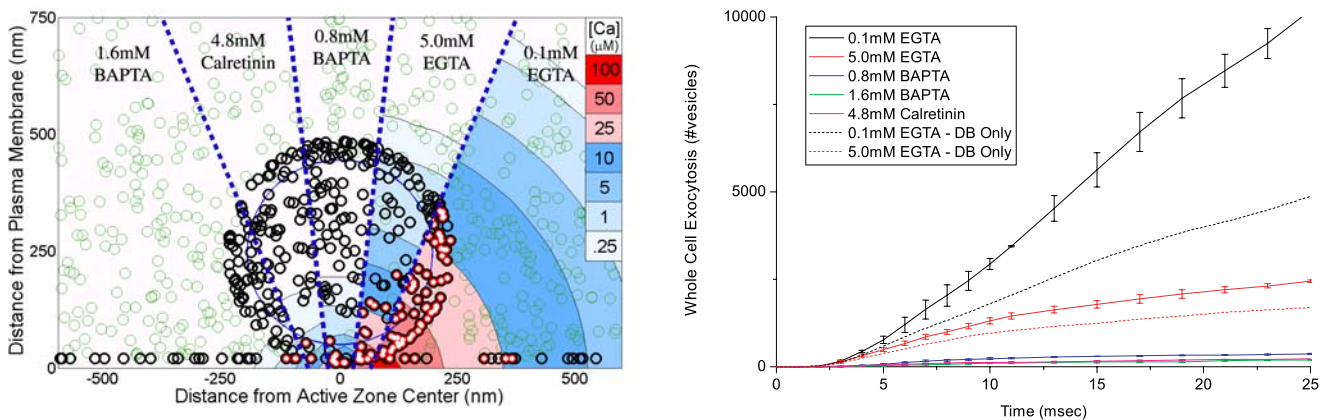
## Summary

Acoustic information is encoded by the inner hair cell synapse, wholly represented by the tonotopic array of ANFs, and then processed by divergent pathways in the cochlear nucleus. I have introduced the important features of ANF and cochlear nucleus cellular responses, plus several information enhancements observed in the cochlear nucleus. The ANF response is driven by the specialized inner hair cell synapse. Each cochlear nucleus cell type has a unique milieu of membrane conductances that shape their *in vitro* response (Figure 4, right), while their *in vivo* responses are further defined by innervation by both ANFs and local interneurons (Figure 4, left). In the following Preliminary Results section, I present the software modeling approach I will use to explore how information is encoded at the hair cell synapse. Additionally, I will detail my approach to modeling the bushy cell membrane in silicon. The first step of this process is to delve further into the details of this particular cell's *in vitro* characterization, carefully evaluating the data sets briefly mentioned in this section, followed by comparison with the simulated response of my model bushy cell.

## IV. Preliminary Results

### Software hair cell Model

In order to address Specific Aim 1, I have designed a novel computational method for probing the details of the hair cell afferent synapse. In this section I will describe my modeling approach and present some simulation results; more detailed results and conclusions will be addressed in my thesis. This work has been carried out under the guidance of T.D. Parsons. We model voltage gated activation of calcium channels, buffered diffusion of calcium in the active zone, calcium binding to synaptic vesicles, and vesicle fusion. Traditional models of buffered diffusion are purely deterministic; they approximate numerical solutions to a set of differential equations in discretized space and time (Roberts 1994; Meinrenken et al. 2002). Our initial approach followed this path, though we found that low stimulus levels, such as those that are responsible for the spontaneous rates of ANFs, could not be adequately described deterministically. We have therefore developed a Hybrid Deterministic-Stochastic Implementation (HDSI) to describe exocytosis under any range of stimulus conditions. The HDSI technique combines whole cell parameters, such as calcium current activation and the kinetics of exocytosis, with stochastic processes such as the gating of individual channels and binding of individual calcium ions (Kruk et al. 1997; Gil et al. 2000). Our hybrid technique successfully brings together disparate types of physiological information while maintaining enough similarity to previous purely deterministic models to facilitate comparison with our results.



**11. How calcium buffering affects hair cell exocytosis** (left) A cross section of a single hair cell active zone. The abscissa represents the plasmalemma surface; at the center of the abscissa is an array of 72 calcium channels. The dense body is directly above the calcium channel array, and has roughly 385 synaptic vesicles tethered around it (black circles). Simulation results using five buffer conditions used experimentally are displayed for comparison, with the strongest buffer (1.6mM BAPTA) on the left and the weakest (0.1mM EGTA) on the right. After 25ms at -50mV (-75mV holding) free calcium levels extend much further in the weak buffer condition, resulting in more exocytosis (vesicles filled with red and white). (right) The time course of exocytosis for the five buffer conditions on the right. Mean and standard error calculated from five simulations for each condition. The dotted lines represent exocytosis under the EGTA conditions when only vesicles tethered to the dense body or plasmalemma are considered fusion competent (black circles on right Figure). Solid lines consider all vesicles in the active zone, including the cytosolic vesicles represented as green circles in the left schematic.

We validate the HDSI implementation by comparing simulated results with other physiological inner hair cell data such as exocytosis driven by uncaged calcium (Beutner et al. 2001) and calcium induced activation of BK channels (Roberts 1993). We have presented the HDSI technique in poster form at the Association for Research in Otolaryngology (Wittig Jr. and Parsons 2004). Manuscripts describing our modeling technique, and the conclusions drawn about calcium buffering at the hair cell synapse, are currently in preparation. Figure 11 compares the effects of calcium buffering on the spatial calcium gradient at the active zone, and on the time course of exocytosis. The active zone is defined by an array of 72 calcium channels (Roberts et al. 1990; Roberts 1994) centered on the abscissa, which are distributed up to 150nm from the active zone center. Directly above the active zone center is the dense body (400nm diameter) which is surrounded by synaptic vesicles (40nm diameter, not to scale) that are distributed according to Lenzi et al (1999; 2002). Vesicles that are tethered to the dense body or plasmalemma are black, and cytosolic vesicles are green. We have simulated the response of a voltage clamp step to -50mV from a holding potential of -75mV under five different buffer conditions. The diverse mobile buffer conditions we examined were based on somewhat conflicting experimental methods and results (Roberts 1993; Edmonds et al. 2000; Moser and Beutner 2000).

During the 25ms simulations, calcium ions enter at the active zone center and diffuse or are sequestered by mobile buffer, thereby creating the free calcium gradients observed with each condition (Figure 11, left). The strongest buffer condition (1.6mM BAPTA) shown in the left section of the schematic effectively inhibits the spread of free calcium compared to the progressively weaker buffer conditions to its right. The differential spread of free calcium with each buffer condition leads to a differential amount of calcium dependent exocytosis. The synaptic vesicles with concentric red and white coloring indicate vesicles that exocytosed within the 25ms depolarization. Again moving from strong (left) to weak (right) buffer conditions, we observe an increased extent of exocytosed vesicles. The time course of exocytosis for these five buffer conditions is predicted in Figure 11, right. Solid lines and error bars show the mean and standard error from five simulations for each buffer condition. As expected from the calcium distributions, the weak buffering conditions lead to significantly more whole cell exocytosis, as 0.1mM EGTA followed by 5.0mM EGTA result in the greatest amount of release. The role of the dense body in exocytosis is unclear (Parsons and Sterling 2003), to test if vesicles are preferentially released from the dense body we can exclude cytosolic vesicles from our simulation results. Dashed lines (11, right) show simulation results when just vesicles tethered to the dense body or plasmalemma were considered fusion competent (only the black vesicles in 11, left). By comparing such results with capacitance recordings from hair cells (Parsons et al. 1994; Moser and Beutner 2000), we can hypothesize about the selectivity of dense body versus cytosolic vesicles during exocytosis.

### **Silicon cochlear nucleus Model**

Through the rest of this section, I will walk you through my methodology for modeling a single cochlear nucleus cell in silicon, the bushy cell. My process for developing a model of the bushy cell is as follows:

- Overview of bushy cell characterization – synaptic connectivity and *in vitro* response.
- Mathematical description of the biological bushy cell – the conductance equation

- Implementation of the conductance equation in silicon – generalized circuit design
- Comparison of circuit simulation results with experimental data

Unlike the other cell types of the cochlear nucleus, a silicon implementation of a bushy-like cell has already been fabricated in silicon by our lab. This neuron was designed to be the spiral ganglion cell for a silicon cochlea chip, produced in 2002. I will conclude this section with data I have collected and analyzed from a silicon bushy-like neuron. Criticism of that model's design and response is addressed in the appendix.

### *Synaptic Connectivity*

Bushy cells use large, calyceal synapses called endbulbs both to receive some of their ANF inputs, and to excite neurons in the MnTB. Bushy cells are innervated via endbulb and non-endbulb synapses with differing proportions from the three classes of spontaneous rate ANFs. Liberman (1991) used HRP labeling of physiologically characterized ANFs to find the average number and location of synapses each ANF type makes in the cochlear nucleus (table 1). Liberman predicted the ANF innervation of bushy cells based on the tonotopic distribution of ANF spontaneous rates (Liberman 1988) and counts of both globular and spherical bushy cells (6,300 and 36,000 respectively, Osen 1970). His predictions agree with reconstructions of electron micrographs by Ostapoff and Morest (1991) that identify 20 – 50 ANF excitatory synapses on or near the cell body of globular bushy cells. Ostapoff and Morest also identified two different types of inhibitory synapses, 10 – 30 putative glycinergic synapses were distributed approximately evenly across the cell and its dendrites, while 15 – 45 putative gabaergic synapses had highest densities on the cell body and on the distal dendrites. The glycinergic inputs originate from d-stellate and tuberculoventral cells (Wickesberg and Oertel 1990; Golding and Oertel 1997; Ferragamo et al. 1998) but the gabaergic inputs have yet to be identified, though they may originate from Golgi cells in the granular cell domain (Osen et al. 1991; Kolston et al. 1992). The relative proportion of inputs from d-stellate and tuberculoventral cells have not been identified anatomically, though physiological evidence indicates the proportion is quite variable (Kopp-Scheinpflug et al. 2002).

<i>ANF divergence</i>	LSR	MSR	HSR			
spherical bushy endbulb	1	1	1			
Non-endbulb	1	1	0.5			
Globluar bushy	3	2	6			

<i>CN convergence</i>	LSR	MSR	HSR	Glyc	GABA
spherical bushy total	0.5	0.5	2	?	?
Globluar bushy modified endbulb	2.6	2.9	19.4	.	.
Non-Endbulb	2.5	3	22	10-30	15-45

**Table 1. innervation of bushy cells.** (left) ANF divergence by spontaneous rate; the average number of synapses a single fiber of each SR type makes in the cat. (right) Convergence of inputs onto bushy cells; predicted ANF numbers based on ANF divergence and distribution, predicted inhibitory numbers assume each synapse is from a distinct cell. Glycine (Glyc) and Gaba estimates have not been made for spherical bushy cells. ANF data from Liberman (1991), inhibitory inputs from Ostapoff and Morest (1991).

The large synaptic area of calyceal synapses leads to large evoked PSCs. Nicol and Walmsley (2002) used serial-section electron microscopy to reconstruct four rat endbulbs of Held. They found that each was made up of 85 – 217 active zones that cumulatively contained thousands of docked vesicles per endbulb, leading to large evoked

EPSCs (2.8nA at a holding potential of -60mV, Oleskevich and Walmsley 2000). EPSCs are mediated mainly by fast AMPA receptors, composed of GluR3 and GluR4 receptor subunits in the flop configuration (Gardner et al. 2001). On average bushy cell mEPSCs have an amplitude of 65pA (holding at -65mV), rise time of 140 $\mu$ sec, and a decay time constant of 400 $\mu$ sec (Gardner et al. 1999). Assuming each mini results from a single vesicle fusion, the evoked EPSCs are elicited by more than 40 vesicle fusions. While the large surface area of calyceal synapses lends to large evoked currents, it also limits the diffusion of exocytosed glutamate from the cleft, which causes synaptic depression via desensitization (Trussell et al. 1993). Bushy cell mEPSCs desensitize with a time constant of 910 $\mu$ sec, and recover from desensitization with a time constant of 19ms (Gardner et al. 2001). The physiological details of the inhibitory inputs to bushy cells have not been characterized to the extent of the excitatory ANF inputs, though sound evoked IPSPs (Smith and Rhode 1987) and evoked rate reduction (Kopp-Scheinflug et al. 2002) have been clearly observed.

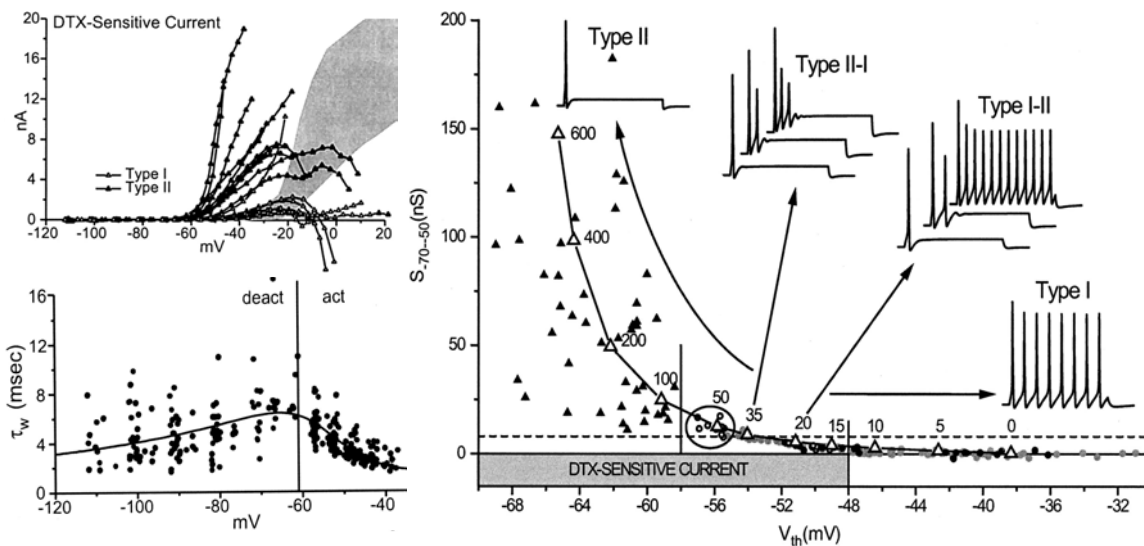
### *In vitro Characterization*

The potassium conductances that shape the response of bushy cells have been characterized under voltage clamp using dissociated ventral cochlear nuclei from adult guinea pigs (Manis and Marx 1991; Rothman and Manis 2003b,a). Dissociated cells are classified based on their response to current injection such that the t-stellate response is called type I, and the bushy response type II (see *in vitro* responses in Figure 4). Manis and Marx (1991) identified  $K_{LT}$  as the primary conductance that is responsible for the bushy cell characteristic response of 1 to 3 spikes when injected with current. Figure 12 presents the characterization of  $K_{LT}$  in VCN cells by Rothman and Manis (2003c; 2003b; 2003a). Dendrotoxin (DTX) was used to pharmacologically isolate  $K_{LT}$  (12, top left), which revealed a clear difference in activation voltage between the low threshold (lines, activated close to -60mV) and high threshold potassium currents (gray area, activates close to -30mV). Boltzman fits to bushy and t-stellate conductances were used to quantify their differences in  $K_{LT}$  and  $K_{HT}$ ; activation curves for  $K_{HT}$  were statistically identical for the two cell types, yet  $K_{LT}$  currents were larger and activated approximately 10mV more negative in bushy cells. The time course of  $K_{LT}$  activation and deactivation in bushy cells followed fourth order kinetics with an average time constant of roughly 4ms (12, bottom left), and most bushy cells showed a slow, partial inactivation with a time constant ranging from 30ms to greater than 150ms.

Bushy cells operate with significant component variability: their  $K_{LT}$  conductance qualitatively exhibits a wide range of peak currents, activation curves, and time course of activation (12, left). Rothman and Manis sought to quantitatively compare whole cell IV characteristics across the VCN in Figure 12, right. The threshold voltage ( $V_{th}$ , abscissa) required to elicit an inward current of 0.1nA in 171 cells ranged from -70 to -30mV. Within the bushy cell population, fits to the IV curve between -70mV and -50mV varied from 8 to 180nS ( $S_{-70,-50}$ , ordinate). Rothman and Manis simulated the *in vitro* response of model cells using a range of  $V_{th}$  and  $S_{-70,-50}$  parameter values (open triangles and  $V_{mem}$  traces to the right). The continuity of whole cell IV characteristics is reflected in the continuity of simulated membrane responses, which ranged from clearly type II (bushy) profiles, to intermediate type II-I and I-II, to clearly type I (t-stellate) profiles. All simulations in which the  $K_{LT}$  maximum conductance exceeded 35nS yielded

characteristic type II responses despite roughly 20 fold variability in maximum conductance and 10mV variability in  $V_{th}$ .

The culmination of detailed *in vitro* characterization is a complete description of all of a cell's conductances. Goldman, Hodgkin and Katz derived the relationship between relative ion permeability and membrane voltage, which can be simplified by assuming a linear IV relation about the reversal potential (Hodgkin and Huxley 1952). Though not valid for all ionic conditions and cell types, this assumption has been verified empirically for several conductances in the cochlear nucleus (Manis and Marx 1991; Bal and Oertel 2001) and allows for synthesis of the conductance equation; a differential equation describing membrane voltage as a function of conductances and reversal potential for each conductance (Equation 1). Beyond the  $K_{LT}$  and  $K_{HT}$  conductances described by Rothman and Manis (2003b; 2003a), bushy cells express a fast inactivating sodium current ( $I_{Na}$ ) responsible for action potential generation as well as a slow, hyperpolarization activated current ( $I_H$ ) which balances  $K_{LT}$  at rest thereby reducing the membrane time constant (Golding et al. 1999). These conductances have not been characterized in bushy cells per say, but have been characterized extensively elsewhere, including in octopus and t-stellate cells of the cochlear nucleus (Bal and Oertel 2000; Rodrigues and Oertel 2004).



**12. Characterization of bushy cell potassium conductances in vitro** (top left) Steady state I-V curves from type I (t-stellate) and type II (bushy) cells. Gray area denotes range of high threshold potassium ( $K_{HT}$ ) responses isolated pharmacologically

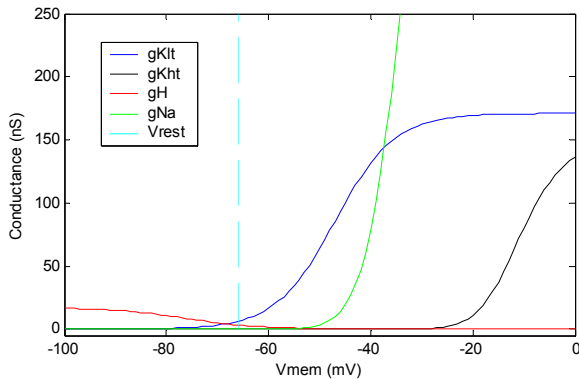
with the dendrotoxin (DTX) Toxin-I. DTX-sensitive currents ( $K_{LT}$ ) are estimated by subtraction of isolated  $K_{HT}$  currents from control currents. (bottom left) Time constant ( $\tau_w$ ) of activation and deactivation measured for 33 type II cells. Currents elicited by voltage steps from -60 or -70mV to the command potential on the abscissa were fit to a fourth order kinetic description of  $I_{LT}$ . (right) Whole cell I-V curve characteristics vary in a continuum across 171 VCN cells.  $V_{th}$  is the voltage which elicits an inward current of 0.1nA. Slope conductance ( $S_{-70,-50}$ ) is defined as the slope of the I-V relation between -70 to -50mV, computed by linear regression. An increased slope conductance generally indicates increased maximum  $K_{LT}$  conductance. Vertical line at -58mV denotes the boundary between type I and type II cells defined by *in vitro* response, while horizontal dashed line at  $S_{-70,-50} = 8nS$  represents another natural boundary. Eleven model VCN cells were simulated using various maximum  $K_{LT}$  conductances (open triangles, with max conductance above). Simulation results for the indicated sets of points exemplify the continuum of responses across the VCN. Increasing current injections are shown for type II-I and type I-II simulations.  $K_{LT}$  I-V, time course, and simulation results from Rothman and Manis (2003c; 2003b; 2003a).

In Figure 13, I summarize the steady state activation curves of the four dominant bushy cell conductances. Each conductance may be translated into a current based on its reversal potential and the membrane potential,  $V_{mem}$  (Equations 2-4;  $E_H = -35mV$ ,  $E_{Na} = 0mV$ ,  $E_K = -80mV$ ). Resting potential ( $V_{rest} = -63mV$ ) represents the membrane potential at which all currents sum to zero in steady state. At potentials hyperpolarized to  $V_{rest}$ , (less than  $-65mV$ ) in steady state,  $g_H$  dominates the conductances and acts to depolarize the membrane. At slightly depolarized potentials ( $-65$  to  $-45mV$ ) in steady state,  $g_{K_{LT}}$  dominates and acts to hyperpolarize the cell. At more depolarized membrane potentials,  $g_{Na}$  clearly dominates the milieu of conductances thereby initiating the positive feedback required for spiking. All of these conductances change in a time dependent manner, and my steady state analogies need be interpreted as simplifications. At  $V_{rest}$ ,  $g_{Na}$ ,  $g_{K_{HT}}$ ,  $g_{K_{LT}}$ , and  $g_H$  have time constants of 0.4, 3.7, 6.3, and 511 ms, respectively. The sluggishness of  $g_{K_{LT}}$  relative to  $g_{Na}$  enables one to three spikes to be elicited at the onset of a depolarizing current injection *in vitro* (Figure 4); at the onset of injection  $V_{mem}$  depolarizes to a voltage where  $g_{Na}$  dominates for a few milliseconds causing spikes, until  $g_{K_{LT}}$  activates sufficiently to pull  $V_{mem}$  back towards the resting potential and fight the depolarizing current. Thus  $g_{K_{LT}}$  works to shape the integration of inputs and is not driven by spike activity. In contrast, conductance based modeling by Rothman and Manis (2003c) show  $K_{HT}$  primarily acts to narrow the action potential width, and has little effect on integration of synaptic inputs.

### Conductance Equations

$$(1) \quad \left( \frac{C_{mem}}{g_K + g_{Na} + g_H} \right) \frac{\partial V_{mem}}{\partial t} = -V_{mem} + \left( \frac{g_K E_K + g_{Na} E_{Na} + g_H E_H}{g_K + g_{Na} + g_H} \right)$$

$$(2-4) \quad I_K = g_K (V_{mem} - E_K); \quad I_{Na} = g_{Na} (V_{mem} - E_{Na}); \quad I_H = g_H (V_{mem} - E_H)$$

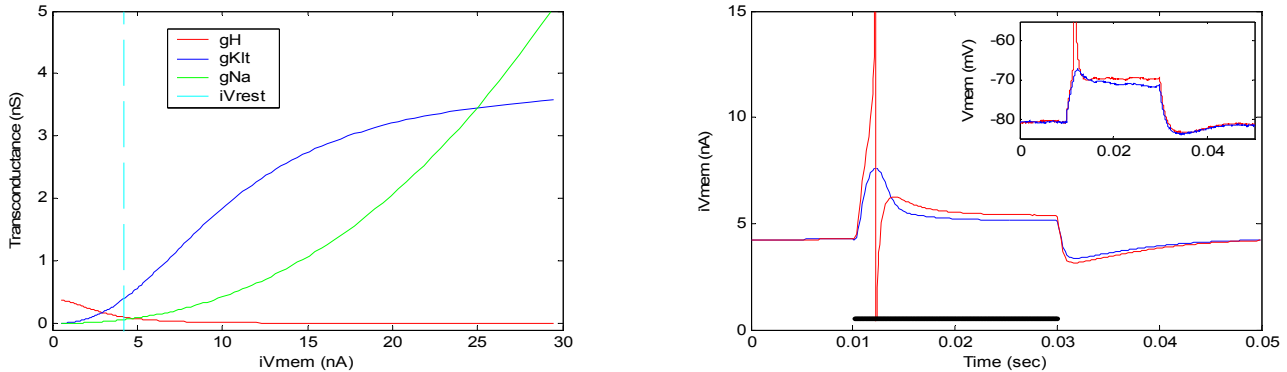


**13. Bushy cell steady state conductances** *G-V curves of four bushy cell conductances. All conductances described by Boltzman functions with parameters detailed in the appendix. Vertical dashed line indicates resting potential of -66mV.  $g_{K_{LT}}$  and  $g_{K_{HT}}$  characterized by Rothman and Manis (2003a),  $g_H$  adapted from Huguenard and McCormick (1992),  $g_{Na}$  based on Costa (1996) and Belluzzi et al (1985). An *in vitro* temperature of 22°C was used in the characterizations listed.*

### Silicon bushy cell model

I have developed a silicon-based implementation of the conductance equation using a combination of capacitors and transistors. My conductance neuron model extends and generalizes an earlier design by John Arthur (Arthur and Boahen 2004). My design relies heavily on the operation of MOS-FET transistors in the sub-threshold regime. In this regime the transistors pass extremely small currents ranging from  $10^{-14}A$  (tens of fA) to  $10^{-7}A$  (hundreds of nA). Small currents are required to create biologically plausible time constants using small capacitors ( $\sim 100fF$ ). Additionally, small currents translate to less power loss across the chip (power =  $V \cdot I$ ), allowing silicon models to more closely approach the power efficiency of the human brain. Particularly important in my conductance model is the current-mode low pass filter, which is a sub-circuit consisting of three or four sub-threshold transistors

and a capacitor. I implement the membrane time constant and the activation kinetics of each conductance using separate, tunable low pass filters. Additionally, conductance parameters such as maximum conductance and activation time constant are controlled using separate off chip voltage sources. In this section, I present simulated results of my silicon implementation of a bushy cell; the simulations presented here assume homogeneity among circuit elements. In a later section, I will address variability intrinsic to silicon design with data from a fabricated silicon auditory neuron.



**14. Silicon bushy cell simulations** (left) simulated silicon bushy cell G-V curves. Transconductance is the change in transistor current with respect to the change in its gate voltage. Each biological conductance modeled in my silicon bushy cell is represented by a separate transconductance:  $g_H$ ,  $g_{KLT}$ , and  $g_{Na}$ . The model conductances are 50 times smaller than those observed biologically (Figure 13) to compensate for an increased driving force and a 100x reduction in membrane capacitance. Membrane voltage is represented by the current  $iV_{mem}$ .  $iV_{mem}$  ranges from 0 to 30nA in this figure, which corresponds to a biological  $V_{mem}$  range of approximately -75mV to -30mV. Resting  $iV_{mem}$  for this cell is 4.3nA. The silicon  $g_{K_{HT}}$  is activated by a digital spiking mechanism and therefore is not plotted against  $iV_{mem}$ . (right) Comparison of silicon and biological bushy cell responses to depolarizing current injection.  $iV_{mem}$  is plotted versus time during a 20ms injection of 6pA (blue, no spike) and 10pA (red, onset spike). Inset shows a biological bushy cell's response to a 20ms injection of 175pA (blue, no spike) and 200pA (red, onset spike), recorded by M. McGinley in Dr. Oertel's laboratory, and compensated for a junction potential of -12mV. This cell is slightly hyperpolarized likely due to hypoxia, yet qualitatively shows the characteristic bushy cell response.

My silicon bushy cell model utilizes the four dominant conductances depicted in Figure 13. Based on the modeling results of Rothman and Manis (2003c), I describe  $g_{K_{HT}}$  as active only to repolarize the membrane after a spike, and therefore I consider it independent of  $V_{mem}$ . In Figure 14 I present the silicon bushy cell's simulated steady state activation curves and *in vitro* response to current injection. Membrane voltage is represented as the current  $iV_{mem}$  to take advantage of current-mode low pass filters. Biological conductances are represented by the transconductance of specific transistors in the circuit model (see appendix). In the G-V curves of Figure 14, I plot the relative conductances of  $g_H$ ,  $g_{K_{LT}}$  and  $g_{Na}$  while  $iV_{mem}$  spans from 0 to 20nA, which corresponds to the  $V_{mem}$  range of approximately -75mV to -30mV in Figure 13. The steady state balance of  $I_H$  and  $I_{K_{LT}}$  leads to a resting  $iV_{mem}$  of 4.3nA. The simulated silicon bushy cell response to current injection (Figure 14, right) qualitatively matches that found *in vitro* (Figure 14, right inset). The onset of a strong depolarizing current injection elicits a single spike (red traces) followed by a sag in  $V_{mem}$  as  $K_{LT}$  activates. A slightly weaker current injection causes a rise in  $V_{mem}$  which

again subsides as  $K_{LT}$  turns on (blue traces). In both cases, when the current injection ceases a hyperpolarizing rebound is observed until  $K_{LT}$  deactivates to its resting state. One quite noticeable difference between the silicon and biological bushy cells is the hyperpolarizing phase of their action potentials. The biological bushy cells seem to have an electrotonically distant axon hillock resulting in a peak  $V_{mem}$  of only  $-50\text{mV}$  at the height of the action potential and little or no discernable hyperpolarization immediately after the spike. The silicon bushy cell is a single compartment model and the spiking mechanism drives digital circuitry, therefore it generates a large range of currents which peak at  $6\mu\text{A}$  and completely hyperpolarizes the cell momentarily.

#### Data from silicon auditory neuron chip

Modeling in silicon forces consideration of the tradeoffs between component size and variability. The fabrication procedure imbeds electron acceptors and donors (dopant ions) into specified areas of a crystalline silicon surface in order to form transistor and capacitor components. Decreasing component size allows for more transistors within a specified area, but increases variability between components as quantal differences in dopant ion concentration are accentuated (de Gyvez and Tuinhout 2004). A similar tradeoff can be found in neurons, where component size may correlate to the number of channels representing a whole cell conductance. The fewer the channels, the more noisy an individual cell becomes, and the more likely it will deviate from another cell of the same type. Cell-to-cell variability could potentially be reduced with high expression levels for each conductance, which in certain cells may be the case, though this is not the case in bushy cells (Figure 12). In general, nature imposes limitations on power consumption which ultimately limit the production of proteins such as ionic channels and the ability of a neuron to replenish the ionic gradients maintaining its membrane potential. Neural systems are particularly adept at functioning with high levels of component variability (Figure 6), and due to its parallels, hardware modeling is an appropriate means of exploring this phenomenology.

**15. Variability in silicon Klt implementation** (top)  $K_{LT}$  IV curves from 21 silicon neurons. Mock voltage clamp was achieved by injecting a fixed current onto the neuron's membrane capacitor ( $I_{IN}$ ), and recording  $V_{mem}$  and  $K_{LT}$  once  $V_{mem}$  stabilized. Bias settings were tuned while creating the 5<sup>th</sup> trace to the right (black, with saturation knee at  $0.18\text{nA}$ ), then held constant while each chip was sequentially characterized using the same setup.  $K_{LT}$  is divided by an approximated pad gain of 1000. Most traces formed a loop at the knee between exponential rise and linear saturation which has been removed for clarity. The loops were likely due to poor sodium current isolation; at low injection levels  $K_{LT}$  only balanced  $I_{IN}$ , but at high levels  $V_{mem}$  increased so that  $K_{LT}$  balanced both  $I_{IN}$  and  $I_{Na}$ . Semi-log plot (not shown) reveals most traces have similar slopes, but drastically different threshold and saturation points. (bottom) Comparison of  $K_{LT}$  threshold and saturation in 21 silicon neurons. Maximum  $K_{LT}$  current ( $I_{max}$ ) is plotted against the  $V_{mem}$  required to elicit  $1\text{pA}$  of  $K_{LT}$  current ( $V_{th}$ ). Metrics chosen to roughly mimic those of Rothman and Manis (Figure 12, right).

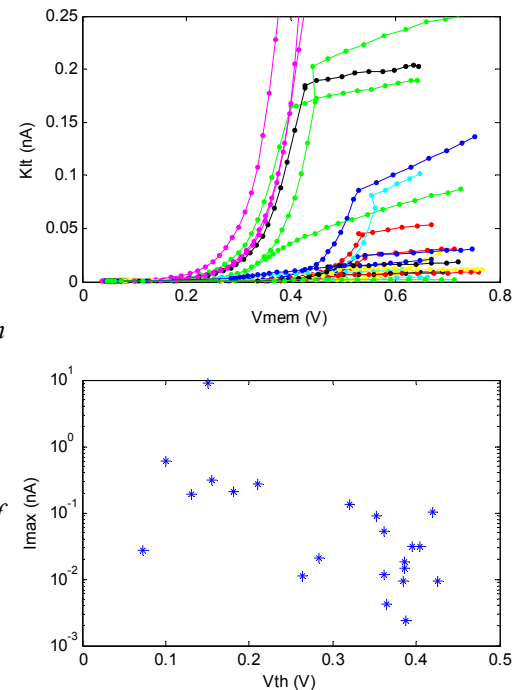


Figure 15 exemplifies how variability between identically designed transistor circuits leads to drastic differences in the response of a silicon  $K_{LT}$  circuit. These results come from an integrate-and-fire silicon spiral ganglia neuron with a  $K_{LT}$  sub-circuit. Description of the circuit is provided in the appendix. I collected the steady state IV curve from 21 separate chips using identical bias settings and test ranges. In Figure 15 (top), I present the IV curve of all 21 chips on a linear scale. All traces show an increase in  $K_{LT}$  current with increasing  $V_{mem}$ , but they differ drastically in their onset of activation and maximal current levels. To quantify this variability in comparison with that observed by Rothman and Manis (2003a), I determined the threshold voltage ( $V_{th}$ ) at which the  $K_{LT}$  current exceeded 1pA and the maximal current ( $I_{max}$ ) for each IV curve (Figure 15, bottom). With the  $K_{LT}$  circuit decoupled from the neuron, spikes ensue when the membrane voltage exceeds roughly 0.75V. Among 21 chips,  $V_{th}$  had a range of 0.35V, almost half of the voltage range used for pre-spike integration of inputs.  $I_{max}$  showed the greatest variability, spanning a range of more than three orders of magnitude with a mean and standard deviation of 0.49nA and 1.85nA respectively.

## V. Research Design and Methods

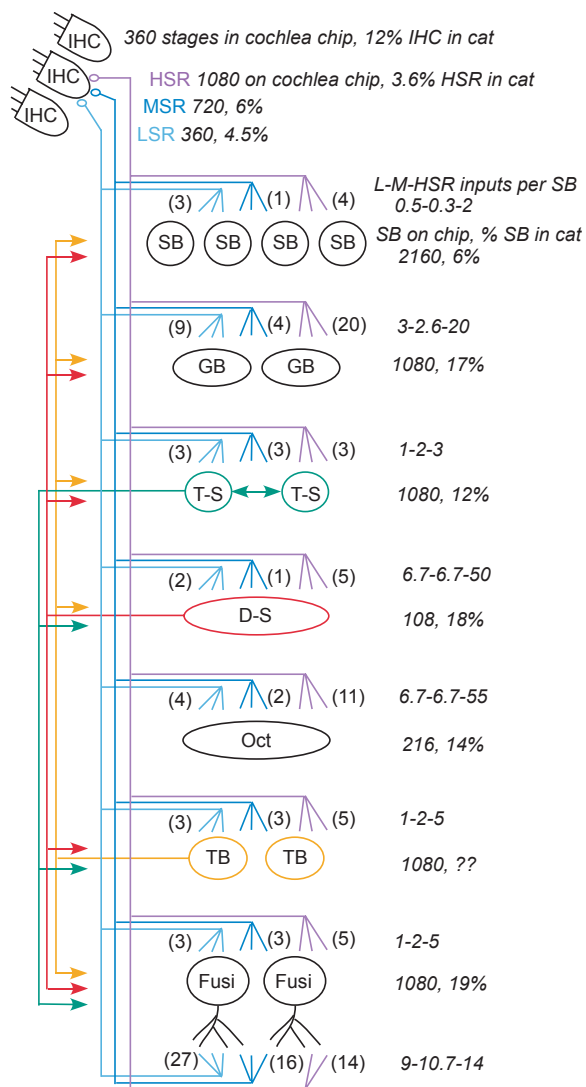
### Software model of the hair cell synapse

Please refer to copy of poster (Wittig Jr. and Parsons 2004), and draft of methods section in the appendix.

### Silicon model of the cochlear nucleus

I propose to design a cochlear nucleus chip that will include a core array of approximately 7,000 conductance based neuron models (Figure 16). I propose to adhere to the experimentally suggested ANF convergences indicated in Figure 16 so I can focus on the goals of Specific Aim 2; namely how variability in conductance parameters and interneuron connectivity affect information enhancement in the cochlear nucleus. Although I will custom design each neuron type and its connectivity, my overall design approach will follow that already established in Dr. Boahen's laboratory. Each silicon neuron will react in real time to synaptic inputs driven both by ANF inputs originating off chip and by local connectivity on chip. In the Preliminary Results section, I plotted the predicted response of my model bushy cell membrane, which took less than one minute to simulate on a Pentium 4 workstation. In silicon, the analog computations of membrane voltage and conductance changes occur in real time. When a silicon neuron spikes, a digital representation of that spike is sent off chip using the Address Event Representation (AER, Boahen 2000). This parallels biological neurons in which integration of inputs is continuous (analog), and communication to other neurons via an action potential is all-or-none (digital). Digital communication is necessary in silicon due to limited number of output pins from a single chip; with an array of 1024 neurons AER requires no more than 10 pins to convey the unique address of each neuron when it spikes, as opposed to using 1024 separate pins to output  $V_{mem}$  from each individual neuron.

When routing AER spikes off chip, such as from the silicon Cochlea to the silicon cochlear nucleus, it is possible to use a microprocessor to designate synaptic connectivity or implement synaptic fan-out (Tabata and Boahen 2002). On chip connectivity can be realized using diffuser networks (Merolla and Boahen 2003), which offer flexibility in how much a given signal is spread by adjustment off chip bias settings. Parameters affecting the conductance equations and synaptic strengths for each neuron type can also be adjusted using off chip biases. Silicon neuron array analysis usually parallels that of extracellular recordings because only spike information is conveyed off chip via AER. Because membrane properties are particularly important in cochlear nucleus information processing, I will output  $iV_{mem}$  (Figure 14) and the conductance currents from a single neuron (the tapped neuron) of each type for mock intracellular experiments. To facilitate component characterization, all tapped neurons will also include circuitry for mock current and voltage clamp experiments.



### 16. Proposed innervation and cell counts on the cochlear nucleus chip compared to cat data.

Input address space will match ANF outputs from B. Wen's Cochlea chip; it has 360 stages which represent individual inner hair cells (IHC), each innervated with 1 LSR, 2 MSR, and 3 HSR auditory nerve fibers. Numbers of each ANF type on the cochlea chip are shown, followed by the percentage of cat ANF type represented. Each ANF innervates seven modeled CN cell types; spherical bushy (SB), globular bushy (GB), *t*-stellate (T-S), *d*-stellate (D-S), octopus (Oct), tuberculoventral (TB), and fusiform/giant (Fusi). Fusiform and giant cells response similarly to sound, and will be modeled as a single cell type. To the right of each cell type is the proposed number on the CN chip, followed by the percentage of that cell type found in cat. I distribute ANF synapses to match the convergence numbers per cell observed anatomically (Lieberman 1991, 1993) and physiologically (Ferragamo et al. 1998) based on the counts of each cell type (Osen 1970; Adams 1976) and ANF types (Lieberman and Mulroy 1982; Ryugo and Sento 1991). As such, each ANF spontaneous rate type innervates a single CN cell type with different synaptic spread, as is observed anatomically (Table I). For instance, a single LSR fiber will innervate 3 SB cells, MSR just 1, and LSR 4 different SB cells. Based on the number of each fiber type and number of SB cells, the number of L-M-HSR inputs per each SB cell will be 0.5-0.3-2. Innervation of D-S estimated based on tuning curves. Number of TB cells estimated to match T-S cell count. Fusi require

separate somatic and dendritic inputs due to dramatic differences in synaptic spread, in all other cell types ANF inputs are assumed homogeneous. Local inhibitory connections from D-S, and TB cells (red and orange arrows) will be implemented on chip, as well as excitatory connectivity from T-S cells (green arrows). Schematic neuron widths represent the frequency range of their inputs, D-S and Oct both receiving the most wideband inputs.

**Aim 1. Examines what limits the ability of the hair cell afferent synapse to convey temporal information at high frequencies**

- A. Test the hypothesis that weak calcium buffering mediates exocytosis at this synapse. Several kinetic equivalents to the endogenous calcium buffer have been suggested experimentally, ranging from 0.1mM EGTA (weakest, Moser and Beutner 2000) to 1.6mM BAPTA (strongest, Roberts 1993). Using my software model of the hair cell synapse, I will simulate a voltage clamp experiment under various buffer conditions and compare the time course of vesicle release with experimental perforated patch results (Parsons et al. 1994; Moser and Beutner 2000). By matching each of my simulated results with the experimental data, my model will suggest what buffer condition mediates exocytosis. Additionally, I will probe the sensitivity of my result to various assumed parameters such as the distribution of vesicles at the plasmalemma (Lenzi et al. 1999; Lenzi et al. 2002) and the distribution of calcium channels at the active zone (Roberts et al. 1990; Roberts 1994).
- B. Test the hypothesis that weak calcium buffering does not degrade the temporal fidelity of exocytosis at this synapse compared to the response under strong buffer conditions. Again simulating voltage clamp experiments, I will examine how buffering affects the time course of exocytosis over a range of stimulation levels. Unlike Goal A, which compares the time course and magnitude of simulation results with physiological data, Goal B calls for comparison strictly between the temporal components of each simulation response. I will compare several temporal features across buffer conditions and stimulus magnitudes; the latency to first release, 10% release, 50% release, and the time constants of exocytosis for each condition. I will also model acoustically driven changes in receptor potential (using a filtered, half wave rectified sinusoidal input current) to observe the degree of phase locking over short periods of time.

**Aim 2. Examines how component variability affects information enhancement across the tonotopic axis of the cochlear nucleus**

The first step to addressing Aim 2 is to find the ideal bias settings and characterize component variability on the cochlear nucleus chip. In addressing each goal of Aim 2, I will use the bias settings that best reproduce the intracellular response of each cell in question unless otherwise stated. As shown in Figure 16, individual conductances from a tapped neuron can be compared between chips to create an estimate of their variability. This is achieved by finding optimal bias settings for a conductance of a single tapped neuron, then characterizing the same conductance on multiple chips while keeping the bias settings fixed. I will also use this approach to characterize variability in spike thresholds and synaptic strengths for each neuron type on the cochlear nucleus chip. These mock intracellular comparisons can only be carried out across chips because I will implement only one tapped neuron of each cell type per chip. In contrast, mock extracellular comparisons can be carried out for all neurons on a chip by analyzing their AER outputs.

Acoustic stimulation will be achieved by one of two methods: computer simulated acoustic stimulation of a cochlea and ANF model (Rothman et al. 1993; Eriksson and Robert 1999) or stimulation of Bo Wen's silicon Cochlea chip with a current source that describes an acoustic waveform. Computer simulated ANF models have been designed

to express observed physiological features including spike rate adaptation (Figure 1, right) and the frequency dependence of phase locking (Figure 2), and as such will provide a rigorous description of cochlear nucleus inputs for the mock *in vivo* experiments. In contrast, B. Wen's current silicon Cochlea chip is currently in fabrication, and its response has not yet been characterized. The silicon Cochlea will provide real time inputs that are subject to the same sources of component variability described throughout this document, namely variability in input levels, and conductance parameters. As such, this input source will offer further insight as to the contribution of variability to information processing in the auditory system, as well as highlight the complexities of modeling large-scale, multi-chip systems.

- A. **Phase locking by bushy cells.** I will investigate the phase locking ability of globular bushy cells using computer simulated ANF outputs to pure tone stimuli. My simulated ANF input will necessarily excite a majority of the chip based on the spontaneous rates of the various ANF fiber types – this is important because of local inhibition by interneurons. I will construct period histograms and find the synchronization coefficient to quantify phase locking in each cell (Figure 2). In order to examine how component variability affects phase locking, I will sequentially rotate the CF of the ANF inputs such that a particular input ANF address will have a CF of 1kHz for one trial, 1.2kHz for the next, and so on. This technique effectively allows me to quantify phase locking with the same pure tone stimuli using a variety of neurons from the same chip. I will also quantify the effect of inhibition on bushy cell phase locking. Using biases affecting the spread and strength of inhibition from both d-stellate and tuberculoventral cells, I will characterize how these parameters relate to phase locking ability.
- B. **Recurrent network contribution to spectrum representation by t-stellate cells.** I will first probe the dynamic range of t-stellate outputs using pure tone stimuli. The pure tone results should indicate that t-stellate's spike rate varies over a wider range of acoustic intensity levels than any one of its ANF inputs. As with the bushy cells, each t-stellate neuron will be characterized using a range of CF inputs to observe the variability across chip and across spectrum. I will then systematically characterize the effects of change the spread and strength of each recurrent connection – those from t-stellates, d-stellates, and tuberculoventral cells (Figure 16). Finally, I will stimulate using stereotyped speech patterns to facilitate comparison with previous experimental results (Blackburn and Sachs 1990; Recio and Rhode 2000), while varying the recurrent connectivity.
- C. **Pitch extraction by octopus cells.** I will characterize variability in octopus dendritic filtering using the tapped version of this cell on my chip. By adjusting the space constant of dendritic filtering while stimulating with simulated ANF inputs, I will probe how variability in dendritic filtering affects the response of these cells to sound. In particular, I will quantify each octopus cell's phase locking ability (synchronization coefficient) when stimulating with low frequency pure tones and its gain in representing amplitude modulated sounds (Figure 8). Additionally I will use the synchronization coefficient metric to quantify the octopus cell's ability to represent the pitch of a harmonic complex. Octopus cell ability to encode these three forms of pitch will be related to the component variability observed in their dendritic filtering, synaptic inputs, and membrane conductances.
- D. **Specificity of spectral feature detection in fusiform and giant cells.** In order to assess how variability of each input cell type accumulates within the DCN circuit, I will first characterize each individual cell type's variability:

ANF, t-stellate, d-stellate, and tuberculoventral inputs. Variability will be assessed in terms of tuning curves for each cell type, as well as conformation to each types expected PSTH response. By explicitly controlling the contribution of each input to the fusiform cells, I will isolate their respective affects on fusiform spectral feature detection. I will measure the specificity of fusiform spectral feature detection using previously established experimental techniques (Spirou and Young 1991; Nelken and Young 1994), which include sensitivity to notch width and location (see Figure 9).

### **Proposed Timeline**

I plan to complete circuit design of each of the included neurons by August 2004. I will layout my circuit design for submission in the October 18<sup>th</sup> fabrication cycle, though if layout or design complications arise, the next submission data is on December 6<sup>th</sup>. During the 8 to 10 week fabrication period, I will continue work on my Aim 1 goals and develop the computer simulated cochlea and ANF models required to test my chip. Through 2005 I will address my Aim 2 goals, and write and defend my thesis Spring 2006.

### **VI. Facilities**

My proposed research aims are computational and require no facilities specialized for research with animals. Specific Aim 1 requires the use of a Pentium IV workstation; programmatic structure and execution times are specified in Appendix 1. Specific Aim 2 requires computer simulation during the design and layout phase. I will have my cochlear nucleus chip fabricated using the educational consortium MOSIS. Chip testing will involve standard equipment available in Dr. Boahen's laboratory such as power supplies, logic analyzers, digital input/output pc boards, and function generators. The particular equipment used to address each goal of Aim 2 will be further addressed in my thesis.

## VII. Literature Cited

- Adams, J.C. (1976). Single Unit Studies on the Dorsal and Intermediate Acoustic Striae. *J Comp Neurol* 170(1): 97-106.
- Arthur, J.V. and Boahen, K. (2004). Recurrently Connected Silicon Neurons with Active Dendrites for One-Shot Learning. International Joint Conference on Neural Networks.
- Bal, R. and Oertel, D. (2000). Hyperpolarization-Activated, Mixed-Cation Current (I(H)) in Octopus Cells of the Mammalian Cochlear Nucleus. *J Neurophysiol* 84(2): 806-17.
- Bal, R. and Oertel, D. (2001). Potassium Currents in Octopus Cells of the Mammalian Cochlear Nucleus. *J Neurophysiol* 86(5): 2299-311.
- Banks, M.I. and Sachs, M.B. (1991). Regularity Analysis in a Compartmental Model of Chopper Units in the Anteroventral Cochlear Nucleus. *J Neurophysiol* 65(3): 606-29.
- Belluzzi, O., Sacchi, O. and Wanke, E. (1985). A Fast Transient Outward Current in the Rat Sympathetic Neurone Studied under Voltage-Clamp Conditions. *J Physiol* 358: 91-108.
- Beutner, D., Voets, T., Neher, E. and Moser, T. (2001). Calcium Dependence of Exocytosis and Endocytosis at the Cochlear Inner Hair Cell Afferent Synapse. *Neuron* 29(3): 681-90.
- Blackburn, C.C. and Sachs, M.B. (1989). Classification of Unit Types in the Anteroventral Cochlear Nucleus: Pst Histograms and Regularity Analysis. *J Neurophysiol* 62(6): 1303-29.
- Blackburn, C.C. and Sachs, M.B. (1990). The Representations of the Steady-State Vowel Sound /E/ in the Discharge Patterns of Cat Anteroventral Cochlear Nucleus Neurons. *J Neurophysiol* 63(5): 1191-212.
- Blum, J.J. and Reed, M.C. (1998). Effects of Wide Band Inhibitors in the Dorsal Cochlear Nucleus. Ii. Model Calculations of the Responses to Complex Sounds. *J Acoust Soc Am* 103(4): 2000-9.
- Blum, J.J., Reed, M.C. and Davies, J.M. (1995). A Computational Model for Signal Processing by the Dorsal Cochlear Nucleus. Ii. Responses to Broadband and Notch Noise. *J Acoust Soc Am* 98(1): 181-91.
- Boahen, K.A. (2000). Point-to-Point Connectivity between Neuromorphic Chips Using Address Events. *IEEE Transactions on Circuits and Systems II: Analog and Digital Signal Processing* 47(5): 416-434.
- Boudreau, J.C. and Tsuchitani, C. (1970). Cat Superior Olive S-Segment Cell Discharge to Tonal Stimulation. *Contrib Sens Physiol* 4: 143-213.
- Brawer, J.R. and Morest, D.K. (1975). Relations between Auditory Nerve Endings and Cell Types in the Cat's Anteroventral Cochlear Nucleus Seen with the Golgi Method and Nomarski Optics. *J Comp Neurol* 160(4): 491-506.
- Bregman, A.S., Liao, C. and Levitan, R. (1990). Auditory Grouping Based on Fundamental Frequency and Formant Peak Frequency. *Can J Psychol* 44(3): 400-13.
- Cariani, P.A. and Delgutte, B. (1996a). Neural Correlates of the Pitch of Complex Tones. I. Pitch and Pitch Salience. *J Neurophysiol* 76(3): 1698-716.

- Cariani, P.A. and Delgutte, B. (1996b). Neural Correlates of the Pitch of Complex Tones. II. Pitch Shift, Pitch Ambiguity, Phase Invariance, Pitch Circularity, Rate Pitch, and the Dominance Region for Pitch. *J Neurophysiol* 76(3): 1717-34.
- Casseday, J.H., Fremouw, T. and Covey, E. (2002). The Inferior Colliculus: A Hub for the Central Auditory System. *Integrative Functions in the Mammalian Auditory Pathway*. D. Oertel, A. N. Popper and R. R. Ray. New York, Springer: 238-318.
- Costa, P.F. (1996). The Kinetic Parameters of Sodium Currents in Maturing Acutely Isolated Rat Hippocampal Ca1 Neurons. *Brain Res Dev Brain Res* 91(1): 29-40.
- Covey, E. and Casseday, J.H. (1991). The Monaural Nuclei of the Lateral Lemniscus in an Echolocating Bat: Parallel Pathways for Analyzing Temporal Features of Sound. *J Neurosci* 11(11): 3456-70.
- Davis, K.A., Ramachandran, R. and May, B.J. (2003). Auditory Processing of Spectral Cues for Sound Localization in the Inferior Colliculus. *J Assoc Res Otolaryngol* 4(2): 148-63.
- Davis, K.A. and Young, E.D. (2000). Pharmacological Evidence of Inhibitory and Disinhibitory Neuronal Circuits in Dorsal Cochlear Nucleus. *J Neurophysiol* 83(2): 926-40.
- De Gyvez, J.P. and Tuinhout, H.P. (2004). Threshold Voltage Mismatch and Intra-Die Leakage Current in Digital Cmos Circuits. *IEEE Journal of Solid-State Circuits* 39(1): 157-168.
- Delgutte, B. and Kiang, N.Y. (1984a). Speech Coding in the Auditory Nerve: I. Vowel-Like Sounds. *J Acoust Soc Am* 75(3): 866-78.
- Delgutte, B. and Kiang, N.Y. (1984b). Speech Coding in the Auditory Nerve: III. Voiceless Fricative Consonants. *J Acoust Soc Am* 75(3): 887-96.
- Delgutte, B. and Kiang, N.Y. (1984c). Speech Coding in the Auditory Nerve: IV. Sounds with Consonant-Like Dynamic Characteristics. *J Acoust Soc Am* 75(3): 897-907.
- Delgutte, B. and Kiang, N.Y. (1984d). Speech Coding in the Auditory Nerve: V. Vowels in Background Noise. *J Acoust Soc Am* 75(3): 908-18.
- Doucet, J.R., Ross, A.T., Gillespie, M.B. and Ryugo, D.K. (1999). Glycine Immunoreactivity of Multipolar Neurons in the Ventral Cochlear Nucleus Which Project to the Dorsal Cochlear Nucleus. *J Comp Neurol* 408(4): 515-31.
- Doucet, J.R. and Ryugo, D.K. (1997). Projections from the Ventral Cochlear Nucleus to the Dorsal Cochlear Nucleus in Rats. *J Comp Neurol* 385(2): 245-64.
- Edmonds, B., Reyes, R., Schwaller, B. and Roberts, W.M. (2000). Calretinin Modifies Presynaptic Calcium Signaling in Frog Sacculus Hair Cells. *Nature Neuroscience* 3(8): 786-90.
- Ehret, G. (1979). Quantitative Analysis of Nerve Fibre Densities in the Cochlea of the House Mouse (*Mus Musculus*). *J Comp Neurol* 183(1): 73-88.
- Eisen, M.D., Spassova, M.A. and Parsons, T.D. (2004). Large Releasable Pool of Synaptic Vesicles in Chick Cochlear Hair Cells. *J Neurophysiol*.
- Eriksson, J.L. and Robert, A. (1999). The Representation of Pure Tones and Noise in a Model of Cochlear Nucleus Neurons. *J Acoust Soc Am* 106(4 Pt 1): 1865-79.

- Evans, E.F. (1978). Place and Time Coding of Frequency in the Peripheral Auditory System: Some Physiological Pros and Cons. *Audiology* 17(5): 369-420.
- Ferragamo, M.J., Golding, N.L. and Oertel, D. (1998). Synaptic Inputs to Stellate Cells in the Ventral Cochlear Nucleus. *J Neurophysiol* 79(1): 51-63.
- Frisina, R.D., Smith, R.L. and Chamberlain, S.C. (1990). Encoding of Amplitude Modulation in the Gerbil Cochlear Nucleus: I. A Hierarchy of Enhancement. *Hear Res* 44(2-3): 99-122.
- Fujino, K. and Oertel, D. (2003). Bidirectional Synaptic Plasticity in the Cerebellum-Like Mammalian Dorsal Cochlear Nucleus. *Proc Natl Acad Sci U S A* 100(1): 265-70.
- Gardner, S.M., Trussell, L.O. and Oertel, D. (1999). Time Course and Permeation of Synaptic Ampa Receptors in Cochlear Nuclear Neurons Correlate with Input. *J Neurosci* 19(20): 8721-9.
- Gardner, S.M., Trussell, L.O. and Oertel, D. (2001). Correlation of Ampa Receptor Subunit Composition with Synaptic Input in the Mammalian Cochlear Nuclei. *J Neurosci* 21(18): 7428-37.
- Geisler, C.D. (1998). *From Sound to Synapse*. New York, Oxford Press.
- Gil, A., Segura, J., Pertusa, J.A. and Soria, B. (2000). Monte Carlo Simulation of 3-D Buffered Ca(2+) Diffusion in Neuroendocrine Cells. *Biophys J* 78(1): 13-33.
- Godfrey, D.A., Kiang, N.Y. and Norris, B.E. (1975). Single Unit Activity in the Posteroventral Cochlear Nucleus of the Cat. *J Comp Neurol* 162(2): 247-68.
- Goldberg, J.M. and Brown, P.B. (1969). Response of Binaural Neurons of Dog Superior Olivary Complex to Dichotic Tonal Stimuli: Some Physiological Mechanisms of Sound Localization. *J Neurophysiol* 32(4): 613-36.
- Golding, N.L., Ferragamo, M.J. and Oertel, D. (1999). Role of Intrinsic Conductances Underlying Responses to Transients in Octopus Cells of the Cochlear Nucleus. *J Neurosci* 19(8): 2897-905.
- Golding, N.L. and Oertel, D. (1996). Context-Dependent Synaptic Action of Glycinergic and Gabaergic Inputs in the Dorsal Cochlear Nucleus. *J Neurosci* 16(7): 2208-19.
- Golding, N.L. and Oertel, D. (1997). Physiological Identification of the Targets of Cartwheel Cells in the Dorsal Cochlear Nucleus. *J Neurophysiol* 78(1): 248-60.
- Golding, N.L., Robertson, D. and Oertel, D. (1995). Recordings from Slices Indicate That Octopus Cells of the Cochlear Nucleus Detect Coincident Firing of Auditory Nerve Fibers with Temporal Precision. *J Neurosci* 15(4): 3138-53.
- Hall, J.D., Betarbet, S. and Jaramillo, F. (1997). Endogenous Buffers Limit the Spread of Free Calcium in Hair Cells. *Biophys J* 73(3): 1243-52.
- Hancock, K.E., Davis, K.A. and Voigt, H.F. (1997). Modeling Inhibition of Type II Units in the Dorsal Cochlear Nucleus. *Biol Cybern* 76(6): 419-28.
- Hodgkin, A.L. and Huxley, A.F. (1952). A Quantitative Description of Membrane Current and Its Application to Conduction and Excitation in Nerve. *J Physiol* 117(4): 500-44.
- Hollien, H. and Shipp, T. (1972). Speaking Fundamental Frequency and Chronologic Age in Males. *J Speech Hear Res* 15(1): 155-9.

- Huang, A.Y. and May, B.J. (1996). Sound Orientation Behavior in Cats. II. Mid-Frequency Spectral Cues for Sound Localization. *J Acoust Soc Am* 100(2 Pt 1): 1070-80.
- Huguenard, J.R. and McCormick, D.A. (1992). Simulation of the Currents Involved in Rhythmic Oscillations in Thalamic Relay Neurons. *J Neurophysiol* 68(4): 1373-83.
- Isaacson, J.S. and Walmsley, B. (1995). Receptors Underlying Excitatory Synaptic Transmission in Slices of the Rat Anteroventral Cochlear Nucleus. *J Neurophysiol* 73(3): 964-73.
- Issa, N.P. and Hudspeth, A.J. (1996). The Entry and Clearance of Ca<sup>2+</sup> at Individual Presynaptic Active Zones of Hair Cells from the Bullfrog's Sacculus. *Proceedings of the National Academy of Sciences* 93: 9527-9532.
- Javel, E. (1980). Coding of Am Tones in the Chinchilla Auditory Nerve: Implications for the Pitch of Complex Tones. *J Acoust Soc Am* 68(1): 133-46.
- Johnson, D.H. (1980). The Relationship between Spike Rate and Synchrony in Responses of Auditory-Nerve Fibers to Single Tones. *J Acoust Soc Am* 68(4): 1115-22.
- Joris, P.X., Carney, L.H., Smith, P.H. and Yin, T.C. (1994). Enhancement of Neural Synchronization in the Anteroventral Cochlear Nucleus. I. Responses to Tones at the Characteristic Frequency. *J Neurophysiol* 71(3): 1022-36.
- Kanold, P.O. and Manis, P.B. (1999). Transient Potassium Currents Regulate the Discharge Patterns of Dorsal Cochlear Nucleus Pyramidal Cells. *J Neurosci* 19(6): 2195-208.
- Keithley, E.M. and Feldman, M.L. (1983). The Spiral Ganglion and Hair Cells of Bronx Waltzer Mice. *Hear Res* 12(3): 381-91.
- Kiang, N.Y., Morest, D.K., Godfrey, D.A., Guinan, J.J. and Kane, E.C. (1973). Stimulus Coding at Caudal Levels of the Cat's Auditory Nervous System: I. Response Characteristics of Single Units. *Basic Mechanisms in Hearing*. A. R. Moller and P. Boston. New York, Academic: 455-478.
- Kidd, R.C. and Weiss, T.F. (1990). Mechanisms That Degrade Timing Information in the Cochlea. *Hear Res* 49(1-3): 181-207.
- Kim, D.O., Rhode, W.S. and Yin, T.C. (1986). Responses of Cochlear Nucleus Neurons to Speech Signals: Neural Encoding of Pitch, Intensity and Other Parameters. *Auditory Frequency Selectivity*. B. C. J. Moore and R. D. Patterson, Plenum Publishing Corp: 281-288.
- Kolston, J., Osen, K.K., Hackney, C.M., Ottersen, O.P. and Storm-Mathisen, J. (1992). An Atlas of Glycine- and Gaba-Like Immunoreactivity and Colocalization in the Cochlear Nuclear Complex of the Guinea Pig. *Anat Embryol (Berl)* 186(5): 443-65.
- Kopp-Scheinpflug, C., Dehmel, S., Dorrscheidt, G.J. and Rubsamen, R. (2002). Interaction of Excitation and Inhibition in Anteroventral Cochlear Nucleus Neurons That Receive Large Endbulb Synaptic Endings. *J Neurosci* 22(24): 11004-18.
- Kruk, P.J., Korn, H. and Faber, D.S. (1997). The Effects of Geometrical Parameters on Synaptic Transmission: A Monte Carlo Simulation Study. *Biophys J* 73(6): 2874-90.
- Lai, Y.C., Winslow, R.L. and Sachs, M.B. (1994). A Model of Selective Processing of Auditory-Nerve Inputs by Stellate Cells of the Antero-Ventral Cochlear Nucleus. *J Comput Neurosci* 1(3): 167-94.

- Lenzi, D., Crum, J., Ellisman, M.H. and Roberts, W.M. (2002). Depolarization Redistributes Synaptic Membrane and Creates a Gradient of Vesicles on the Synaptic Body at a Ribbon Synapse. *Neuron* 36(4): 649-59.
- Lenzi, D., Runyeon, J.W., Crum, J.W., Ellisman, M.H. and Roberts, W.M. (1999). Synaptic Vesicle Populations in Saccular Hair Cells Reconstructed by Electron Tomography. *Journal of Neuroscience* 19: 119-132.
- Lieberman, M.C. (1988). Physiology of Cochlear Efferent and Afferent Neurons: Direct Comparisons in the Same Animal. *Hear Res* 34(2): 179-91.
- Lieberman, M.C. (1991). Central Projections of Auditory-Nerve Fibers of Differing Spontaneous Rate. I. Anteroventral Cochlear Nucleus. *J Comp Neurol* 313(2): 240-58.
- Lieberman, M.C. (1993). Central Projections of Auditory Nerve Fibers of Differing Spontaneous Rate, II: Posteroventral and Dorsal Cochlear Nuclei. *J Comp Neurol* 327(1): 17-36.
- Lieberman, M.C., Dodds, L.W. and Pierce, S. (1990). Afferent and Efferent Innervation of the Cat Cochlea: Quantitative Analysis with Light and Electron Microscopy. *J Comp Neurol* 301(3): 443-60.
- Lieberman, M.C. and Kiang, N.Y. (1978). Acoustic Trauma in Cats. Cochlear Pathology and Auditory-Nerve Activity. *Acta Otolaryngol Suppl* 358: 1-63.
- Lieberman, M.C. and Mulroy, M.J. (1982). Acute and Chronic Effects of Acoustic Trauma: Cochlear Pathology and Auditory Nerve Pathophysiology. *New Perspectives on Noise-Induced Hearing Loss*. R. P. Hamernick, D. Henderson and R. Salvi. New York, Raven: 105-135.
- Lumpkin, E.A. and Hudspeth, A.J. (1998). Regulation of Free Ca<sup>2+</sup> Concentration in Hair-Cell Stereocilia. *Journal of Neuroscience* 18(16): 6300-18.
- Malmierca, M.S., Leergaard, T.B., Bajo, V.M., Bjaalie, J.G. and Merchan, M.A. (1998). Anatomic Evidence of a Three-Dimensional Mosaic Pattern of Tonotopic Organization in the Ventral Complex of the Lateral Lemniscus in Cat. *J Neurosci* 18(24): 10603-18.
- Manis, P.B. (1990). Membrane Properties and Discharge Characteristics of Guinea Pig Dorsal Cochlear Nucleus Neurons Studied in Vitro. *J Neurosci* 10(7): 2338-51.
- Manis, P.B. and Marx, S.O. (1991). Outward Currents in Isolated Ventral Cochlear Nucleus Neurons. *J Neurosci* 11(9): 2865-80.
- Meinrenken, C.J., Borst, J.G. and Sakmann, B. (2002). Calcium Secretion Coupling at Calyx of Held Governed by Nonuniform Channel-Vesicle Topography. *J Neurosci* 22(5): 1648-67.
- Merchan, M.A. and Berbel, P. (1996). Anatomy of the Ventral Nucleus of the Lateral Lemniscus in Rats: A Nucleus with a Concentric Laminar Organization. *J Comp Neurol* 372(2): 245-63.
- Merolla, P. and Boahen, K. (2003). A Recurrent Model of Orientation Maps with Simple and Complex Cells. *Advances in Neural Information Processing Systems* 16, MIT Press.
- Molitor, S.C. and Manis, P.B. (1999). Voltage-Gated Ca<sup>2+</sup> Conductances in Acutely Isolated Guinea Pig Dorsal Cochlear Nucleus Neurons. *J Neurophysiol* 81(3): 985-98.
- Moser, T. and Beutner, D. (2000). Kinetics of Exocytosis and Endocytosis at the Cochlear Inner Hair Cell Afferent Synapse of the Mouse. *Proceedings of the National Academy of Sciences* 97(2): 883-8.

- Muller, M. and Robertson, D. (1991). Shapes of Rate-Versus-Level Functions of Primary Auditory Nerve Fibres: Test of the Basilar Membrane Mechanical Hypothesis. *Hear Res* 57(1): 71-8.
- Nelken, I. and Young, E.D. (1994). Two Separate Inhibitory Mechanisms Shape the Responses of Dorsal Cochlear Nucleus Type Iv Units to Narrowband and Wideband Stimuli. *J Neurophysiol* 71(6): 2446-62.
- Nicol, M.J. and Walmsley, B. (2002). Ultrastructural Basis of Synaptic Transmission between Endbulbs of Held and Bushy Cells in the Rat Cochlear Nucleus. *J Physiol* 539(Pt 3): 713-23.
- Oertel, D. (1985). Use of Brain Slices in the Study of the Auditory System: Spatial and Temporal Summation of Synaptic Inputs in Cells in the Anteroventral Cochlear Nucleus of the Mouse. *J Acoust Soc Am* 78(1 Pt 2): 328-33.
- Oertel, D. and Wickesberg, R.E. (2002). Ascending Pathways through Ventral Nuclei of the Lateral Lemniscus and Their Possible Role in Pattern Recognition in Natural Sounds. *Integrative Functions in the Mammalian Auditory Pathway*. D. Oertel, A. N. Popper and R. R. Ray. New York, Springer: 207-237.
- Oertel, D., Wu, S.H., Garb, M.W. and Dizack, C. (1990). Morphology and Physiology of Cells in Slice Preparations of the Posteroventral Cochlear Nucleus of Mice. *J Comp Neurol* 295(1): 136-54.
- Oleskevich, S. and Walmsley, B. (2000). Phosphorylation Regulates Spontaneous and Evoked Transmitter Release at a Giant Terminal in the Rat Auditory Brainstem. *J Physiol* 526 Pt 2: 349-57.
- Osen, K.K. (1970). Course and Termination of the Primary Afferents in the Cochlear Nuclei of the Cat. An Experimental Anatomical Study. *Arch Ital Biol* 108(1): 21-51.
- Osen, K.K., Lopez, D.E., Slyngstad, T.A., Ottersen, O.P. and Storm-Mathisen, J. (1991). Gaba-Like and Glycine-Like Immunoreactivities of the Cochlear Root Nucleus in Rat. *J Neurocytol* 20(1): 17-25.
- Ostapoff, E.M. and Morest, D.K. (1991). Synaptic Organization of Globular Bushy Cells in the Ventral Cochlear Nucleus of the Cat: A Quantitative Study. *J Comp Neurol* 314(3): 598-613.
- Palmer, A.R. and Evans, E.F. (1982). Intensity Coding in the Auditory Periphery of the Cat: Responses of Cochlear Nerve and Cochlear Nucleus Neurons to Signals in the Presence of Bandstop Masking Noise. *Hear Res* 7(3): 305-23.
- Parsons, T.D., Lenzi, D., Almers, W. and Roberts, W.M. (1994). Calcium-Triggered Exocytosis and Endocytosis in an Isolated Presynaptic Cell: Capacitance Measurements in Saccular Hair Cells. *Neuron* 13: 875-883.
- Parsons, T.D. and Sterling, P. (2003). Synaptic Ribbon: Conveyor Belt or Safety Belt? *Neuron* 37: 379-382.
- Pfeiffer, R.R. (1966). Classification of Response Patterns of Spike Discharges for Units in the Cochlear Nucleus: Tone-Burst Stimulation. *Exp Brain Res* 1(3): 220-35.
- Portfors, C.V. and Wenstrup, J.J. (2001). Responses to Combinations of Tones in the Nuclei of the Lateral Lemniscus. *J Assoc Res Otolaryngol* 2(2): 104-17.
- Portfors, C.V. and Wenstrup, J.J. (2002). Excitatory and Facilitatory Frequency Response Areas in the Inferior Colliculus of the Mustached Bat. *Hear Res* 168(1-2): 131-8.
- Recio, A. and Rhode, W.S. (2000). Representation of Vowel Stimuli in the Ventral Cochlear Nucleus of the Chinchilla. *Hear Res* 146(1-2): 167-84.

- Remez, R.E., Rubin, P.E., Pisoni, D.B. and Carrell, T.D. (1981). Speech Perception without Traditional Speech Cues. *Science* 212(4497): 947-9.
- Rhode, W.S. (1999). Vertical Cell Responses to Sound in Cat Dorsal Cochlear Nucleus. *J Neurophysiol* 82(2): 1019-32.
- Rhode, W.S. and Greenberg, S. (1994). Encoding of Amplitude Modulation in the Cochlear Nucleus of the Cat. *J Neurophysiol* 71(5): 1797-825.
- Rhode, W.S. and Kettner, R.E. (1987). Physiological Study of Neurons in the Dorsal and Posteroventral Cochlear Nucleus of the Unanesthetized Cat. *J Neurophysiol* 57(2): 414-42.
- Rhode, W.S. and Smith, P.H. (1986). Encoding Timing and Intensity in the Ventral Cochlear Nucleus of the Cat. *J Neurophysiol* 56(2): 261-86.
- Rice, J.J., May, B.J., Spirou, G.A. and Young, E.D. (1992). Pinna-Based Spectral Cues for Sound Localization in Cat. *Hear Res* 58(2): 132-52.
- Roberts, W.M. (1993). Spatial Calcium Buffering in Saccular Hair Cells. *Nature* 363(6424): 74-6.
- Roberts, W.M. (1994). Localization of Calcium Signals by a Mobile Calcium Buffer in Frog Saccular Hair Cells. *Journal of Neuroscience* 14(5 Pt 2): 3246-3262.
- Roberts, W.M., Jacobs, R.A. and Hudspeth, A.J. (1990). Colocalization of Ion Channels Involved in Frequency Selectivity and Synaptic Transmission at Presynaptic Active Zones of Hair Cells. *Journal of Neuroscience* 10(11): 3664-3684.
- Rodrigues, A.R.A. and Oertel, D. (2004). Hyperpolarization-Activated Cation Current,  $I_h$ , in Stellate Cells of the Ventral Cochlear Nucleus on Mice. Association of Research in Otolaryngology, Daytona Beach, FL.
- Rothman, J.S. and Manis, P.B. (2003a). Differential Expression of Three Distinct Potassium Currents in the Ventral Cochlear Nucleus. *J Neurophysiol* 89(6): 3070-82.
- Rothman, J.S. and Manis, P.B. (2003b). Kinetic Analyses of Three Distinct Potassium Conductances in Ventral Cochlear Nucleus Neurons. *J Neurophysiol* 89(6): 3083-96.
- Rothman, J.S. and Manis, P.B. (2003c). The Roles Potassium Currents Play in Regulating the Electrical Activity of Ventral Cochlear Nucleus Neurons. *J Neurophysiol* 89(6): 3097-113.
- Rothman, J.S. and Young, E.D. (1996). Enhancement of Neural Synchronization in Computational Models of Ventral Cochlear Nucleus Bushy Cells. *Auditory Neuroscience* 2: 47-62.
- Rothman, J.S., Young, E.D. and Manis, P.B. (1993). Convergence of Auditory Nerve Fibers onto Bushy Cells in the Ventral Cochlear Nucleus: Implications of a Computational Model. *J Neurophysiol* 70(6): 2562-83.
- Ryugo, D.K. and Sento, S. (1991). Synaptic Connections of the Auditory Nerve in Cats: Relationship between Endbulbs of Held and Spherical Bushy Cells. *J Comp Neurol* 305(1): 35-48.
- Sachs, M.B. and Abbas, P.J. (1974). Rate Versus Level Functions for Auditory-Nerve Fibers in Cats: Tone-Burst Stimuli. *J Acoust Soc Am* 56(6): 1835-47.
- Sachs, M.B. and Young, E.D. (1979). Encoding of Steady-State Vowels in the Auditory Nerve: Representation in Terms of Discharge Rate. *J Acoust Soc Am* 66(2): 470-9.

- Schreiner, C.E. and Langner, G. (1988). Periodicity Coding in the Inferior Colliculus of the Cat. II. Topographical Organization. *J Neurophysiol* 60(6): 1823-40.
- Schwartz, I.R. (1992). The Superior Olivary Complex and Lateral Lemniscal Nuclei. *The Mammalian Auditory Pathway: Neuroanatomy*. D. B. Webster, A. N. Popper and R. R. Fay. New York, Springer-Verlag: 117-167.
- Shamma, S. (1998). Spatial and Temporal Processing in Central Auditory Networks. *Methods in Neuronal Modeling: From Ions to Networks*. C. Koch and I. Segev. Cambridge, MIT Press: 411-460.
- Smith, P.H., Joris, P.X., Carney, L.H. and Yin, T.C. (1991). Projections of Physiologically Characterized Globular Bushy Cell Axons from the Cochlear Nucleus of the Cat. *J Comp Neurol* 304(3): 387-407.
- Smith, P.H., Joris, P.X. and Yin, T.C. (1993). Projections of Physiologically Characterized Spherical Bushy Cell Axons from the Cochlear Nucleus of the Cat: Evidence for Delay Lines to the Medial Superior Olive. *J Comp Neurol* 331(2): 245-60.
- Smith, P.H. and Rhode, W.S. (1987). Characterization of Hrp-Labeled Globular Bushy Cells in the Cat Anteroventral Cochlear Nucleus. *J Comp Neurol* 266(3): 360-75.
- Smith, P.H. and Rhode, W.S. (1989). Structural and Functional Properties Distinguish Two Types of Multipolar Cells in the Ventral Cochlear Nucleus. *J Comp Neurol* 282(4): 595-616.
- Smith, Z.M., Delgutte, B. and Oxenham, A.J. (2002). Chimaeric Sounds Reveal Dichotomies in Auditory Perception. *Nature* 416(6876): 87-90.
- Spirou, G.A., Davis, K.A., Nelken, I. and Young, E.D. (1999). Spectral Integration by Type Ii Interneurons in Dorsal Cochlear Nucleus. *J Neurophysiol* 82(2): 648-63.
- Spirou, G.A. and Young, E.D. (1991). Organization of Dorsal Cochlear Nucleus Type Iv Unit Response Maps and Their Relationship to Activation by Bandlimited Noise. *J Neurophysiol* 66(5): 1750-68.
- Sumner, C.J., Lopez-Poveda, E.A., O'mard, L.P. and Meddis, R. (2002). A Revised Model of the Inner-Hair Cell and Auditory-Nerve Complex. *J Acoust Soc Am* 111(5 Pt 1): 2178-88.
- Taba, B. and Boahen, K. (2002). Topographic Map Formation by Silicon Growth Cones. *Advances in Neural Information Processing Systems* 15, MIT Press.
- Trussell, L.O., Zhang, S. and Raman, I.M. (1993). Desensitization of Ampa Receptors Upon Multiquantal Neurotransmitter Release. *Neuron* 10(6): 1185-96.
- Van Tasell, D.J., Soli, S.D., Kirby, V.M. and Widin, G.P. (1987). Speech Waveform Envelope Cues for Consonant Recognition. *J Acoust Soc Am* 82(4): 1152-61.
- Voigt, H.F. and Young, E.D. (1980). Evidence of Inhibitory Interactions between Neurons in Dorsal Cochlear Nucleus. *J Neurophysiol* 44(1): 76-96.
- Wickesberg, R.E. and Oertel, D. (1988). Tonotopic Projection from the Dorsal to the Anteroventral Cochlear Nucleus of Mice. *J Comp Neurol* 268(3): 389-99.
- Wickesberg, R.E. and Oertel, D. (1990). Delayed, Frequency-Specific Inhibition in the Cochlear Nuclei of Mice: A Mechanism for Monaural Echo Suppression. *J Neurosci* 10(6): 1762-8.
- Wickesberg, R.E., Whitlon, D. and Oertel, D. (1991). Tuberculoventral Neurons Project to the Multipolar Cell Area but Not to the Octopus Cell Area of the Posteroventral Cochlear Nucleus. *J Comp Neurol* 313(3): 457-68.

- Wickesberg, R.E., Whitlon, D. and Oertel, D. (1994). In Vitro Modulation of Somatic Glycine-Like Immunoreactivity in Presumed Glycinergic Neurons. *J Comp Neurol* 339(3): 311-27.
- Wilson, H.R. (1999). *Spikes, Decisions, and Actions: The Dynamical Foundations of Neuroscience*. Oxford, Oxford Press.
- Wittig Jr., J.H. and Parsons, T.D. (2004). Modeling Hair Cell Exocytosis Using a Hybrid Deterministic-Stochastic Implementation. Association for Research in Otolaryngology, Daytona Beach, FL.
- Yin, T.C.T. (2002). Neural Mechanisms of Encoding Binaural Localization Cues in the Auditory Brainstem. *Integrative Functions in the Mammalian Auditory Pathway*. D. Oertel, A. N. Popper and R. R. Ray. New York, Springer: 99-159.
- Young, E.D. (1980). Identification of Response Properties of Ascending Axons from Dorsal Cochlear Nucleus. *Brain Res* 200(1): 23-37.
- Young, E.D. and Brownell, W.E. (1976). Responses to Tones and Noise of Single Cells in Dorsal Cochlear Nucleus of Unanesthetized Cats. *J Neurophysiol* 39(2): 282-300.
- Young, E.D. and Davis, K.A. (2002). Circuitry and Function of the Dorsal Cochlear Nucleus. *Integrative Functions in the Mammalian Auditory Pathway*. D. Oertel, A. N. Popper and R. R. Ray. New York, Springer: 160-206.
- Young, E.D. and Oertel, D. (2004). Cochlear Nucleus. *The Synaptic Organization of the Brain*. G. M. Sheperd. Oxford, University Press: 125-164.
- Young, E.D. and Sachs, M.B. (1979). Representation of Steady-State Vowels in the Temporal Aspects of the Discharge Patterns of Populations of Auditory-Nerve Fibers. *J Acoust Soc Am* 66(5): 1381-1403.
- Zhang, S. and Oertel, D. (1993). Tuberculoventral Cells of the Dorsal Cochlear Nucleus of Mice: Intracellular Recordings in Slices. *J Neurophysiol* 69(5): 1409-21.
- Zhang, S. and Oertel, D. (1994). Neuronal Circuits Associated with the Output of the Dorsal Cochlear Nucleus through Fusiform Cells. *J Neurophysiol* 71(3): 914-30.

## Appendix 1: Hair Cell Synapse Methods and Poster

### Methods:

#### Hybrid Implementation:

We present a novel computational modeling approach to simulate the synaptic details of a bullfrog saccular hair cell. Our model focused on a single pre-synaptic active zone, and addressed calcium influx, buffered calcium diffusion, and exocytosis. Computational models of cellular diffusion processes are usually either deterministic or stochastic. Deterministic diffusion models consist of a set of differential equations solved in time and space. Such modeling is appropriate for describing continuous, macroscopic functions such as flux, population kinetics, or transport (Kidd and Weiss 1990; Roberts 1994; Wu et al. 1996; Hall et al. 1997). Stochastic diffusion models consist of a set of time dependent probabilistic equations that are repetitively evaluated using a pseudo random number generator. Stochastic modeling is therefore appropriate for describing the time evolving location or state of individual species, although large-scale stochastic simulations can be used to describe macroscopic functions such as calcium diffusion throughout a cell (Gil et al. 2000). In our computational model of the frog hair cell sacculus active zone, we created a hybrid deterministic-stochastic implementation. Macroscopic properties of the synaptic physiology such as whole cell calcium current activation and buffered diffusion of calcium were modeled deterministically where as microscopic aspects defined by discrete, molecular-level events such as channel gating, calcium binding, and vesicle fusion were modeled stochastically.

#### Deterministic Components:

**Whole Cell Calcium Current Activation.** We simulated whole cell calcium current activation based on the 3<sup>rd</sup> order calcium channel gating model of Hudspeth and Lewis (1988). The whole cell calcium current,  $I_{Ca}$ , was equal to the maximum total calcium conductance ( $G_{max}$ ) multiplied by the cubic activation parameter ( $m$ ) and the calcium driving force (Equation 1). Hudspeth and Lewis described the voltage and time dependent value of  $m$  as a differential equation dependent on the closing and opening rates  $\alpha$  and  $\beta$  (Equation 2-4). Refer to table 2 for parameter values.

$$(A1.1) \quad \text{Whole Cell } I_{Ca} = G_{max} \times m^3 (V_{mem} - E_{Ca})$$

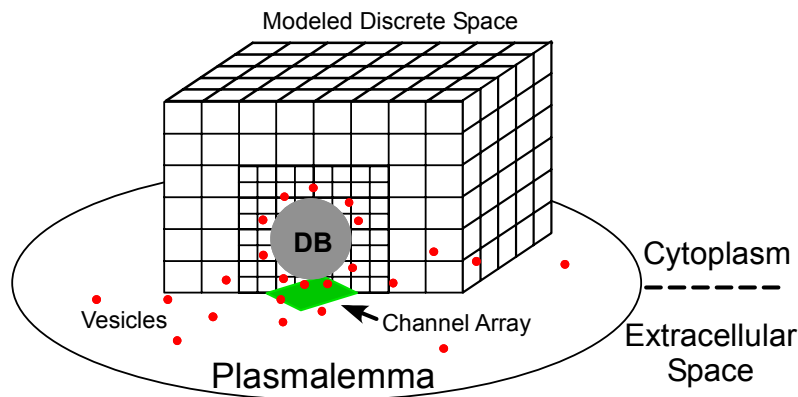
$$(A1.2) \quad \frac{dm}{dt} = \alpha(1 - m) - \beta m$$

$$(A1.3) \quad \beta = \beta_0 \exp\left[\frac{(V_{mem} + V_0)}{V_B}\right] + K_B$$

$$(A1.4) \quad \alpha = \alpha_0 \exp\left[\frac{-(V_{mem} + V_0)}{V_A}\right] + K_A$$

#### Buffered Diffusion:

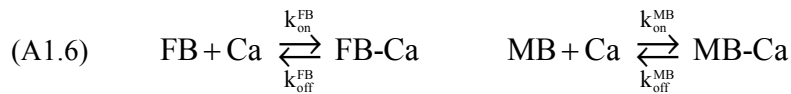
**Geometrical Considerations.** We simulated time evolving buffered diffusion of calcium in the hair cell cytoplasm based on Robert's (1994) computationally intensive model. We considered a cytoplasmic "active zone volume" of  $3.2 \times 3.2 \times 1.6 \mu\text{m}$ . This volume was bounded against a planar plasma membrane surface, with one complete active zone at its center. We discretized the active zone volume into thousands of cubical volume elements (voxels), for numerical evaluation purposes. We used multiple voxel sizes to efficiently model the active zone volume, with small voxels closer to the active zone center and large voxels further away. When modeling exocytosis, where the diameter of vesicles is approximately  $40\text{nm}$  (Lenzi et al. 1999), we used a minimum voxel size of  $(40\text{nm})^3$  closest to the active zone center, and up to  $(320\text{nm})^3$  at the edges of the array. For determining the spatial profile of calcium across the plasmalemma surface we used a minimum voxel size of  $(5\text{nm})^3$  to produce plots similar to those of Roberts (1993). When modeling the activation of BK channels we used a minimum voxel size of  $(10\text{nm})^3$ , based on the dimension of the channel mouth (Doyle et al. 1998).



**Computation of Calcium Concentration.** For each voxel, we solved the time evolving free calcium concentration. We modeled four contributions to the change in free calcium with respect to time ( $d[\text{Ca}]/dt$ ): calcium influx at open calcium channels, diffusion of free calcium in the cytosol, and buffering of free calcium by both fixed and mobile buffers (Equation 4). We described calcium diffusion using Equation 5 (Roberts 1994; Hall et al. 1997; Lumpkin and Hudspeth 1998). Free calcium and mobile buffer were allowed to diffuse freely throughout the active zone volume according to their respective diffusion coefficients,  $D_{\text{Ca}}$  and  $D_{\text{MB}}$ . Diffusion was constrained at the boundaries of the volume; the plasma membrane reflected all diffusing species while the other five surfaces of the active zone volume had static free calcium and total mobile buffer concentrations. Equations 6 and 7 enumerate formulas of the kinetic relations and equivalent differential equations used to describe binding of free calcium (Ca) to both fixed (FB) and mobile (MB) buffers. Calcium was bound by the buffers forming two distinct complexes (FB-Ca and MB-Ca) according to the respective rate constants detailed in Table 2.

$$(A1.4) \quad \frac{d[\text{Ca}]_{\text{total}}}{dt} = \frac{d[\text{Ca}]_{\text{Ca influx}}}{dt} + \frac{d[\text{Ca}]_{\text{diffusion}}}{dt} + \frac{d[\text{Ca}]_{\text{fixed buffer}}}{dt} + \frac{d[\text{Ca}]_{\text{mobile buffer}}}{dt}$$

$$(A1.5) \quad \frac{d[\text{Ca}]_{\text{diffusion}}}{dt} = D_{\text{Ca}} \nabla^2 [\text{Ca}] = D_{\text{Ca}} \left( \frac{\partial^2 [\text{Ca}]}{\partial x^2} + \frac{\partial^2 [\text{Ca}]}{\partial y^2} + \frac{\partial^2 [\text{Ca}]}{\partial z^2} \right)$$



$$(A1.7) \quad \frac{d[\text{Ca}]_{\text{buffers}}}{dt} = \overbrace{k_{\text{off}}^{\text{FB}}[\text{FB-Ca}] - k_{\text{on}}^{\text{FB}}[\text{FB}][\text{Ca}]}^{\text{Fixed Buffer Contribution}} + \overbrace{k_{\text{off}}^{\text{MB}}[\text{MB-Ca}] - k_{\text{on}}^{\text{MB}}[\text{MB}][\text{Ca}]}^{\text{Mobile Buffer Contribution}}$$

Voxels containing calcium channels experienced a change in calcium concentration due to calcium ion influx according to Equations 8 and 9. The voxel calcium current ( $I_{\text{Ca-Vox}}(t)$ ), was a function of the number of open channels in the voxel ( $N_{\text{open-Vox}}$ ), the single channel conductance ( $G_{\text{unit}}$ ), the membrane voltage ( $V_{\text{mem}}$ ), and the reversal potential of calcium ( $E_{\text{rev-Ca}}$ ). The change in calcium concentration due to this current was described using equation 9, where  $F$  is Faraday's constant,  $Z_{\text{ca}}$  is the charge of a single calcium ion, and  $\text{Volume}_{\text{vox}}$  is the volume of the voxel under consideration.

$$(A1.8) \quad I_{\text{Ca-Vox}}(t) = N_{\text{open-Vox}}(t) \cdot G_{\text{unit}} [V_{\text{mem}}(t) - E_{\text{rev-Ca}}]$$

$$(A1.9) \quad \frac{d[\text{Ca}]}{dt} = - \frac{I_{\text{Ca-Vox}}(t)}{(Z_{\text{ca}} \cdot F \cdot \text{Volume}_{\text{Vox}})}$$

**Mobile Buffer Selection.** Identifying an endogenous buffer in the hair cell active zone has been elusive, as several proteins have been proposed (Edmonds et al. 2000; Heller et al. 2002; Hackney et al. 2003). Additionally, several kinetic equivalents to the endogenous buffer zone have been suggested, ranging from millimolar concentrations of the fast buffer BAPTA (Roberts 1994) to micromolar concentrations of the slow buffer EGTA (Moser and Beutner 2000). Throughout our simulations we attempted to understand how such disparate buffering conditions effected calcium diffusion, regulation of calcium dependent potassium (BK) channels, and exocytosis. Our spatio-temporal simulations of buffered calcium diffusion compared the extreme cases of 1.6mM BAPTA and 100 $\mu$ m EGTA. The fast buffer concentration was an experimentally suggested kinetic equivalent to the endogenous buffer based on both perforated patch, and buffer dialyzed whole cell recordings of BK currents (Roberts 1994) in bullfrog sacullar hair cells. The slow buffer concentration was the experimentally suggested kinetic equivalent based on perforated and dialyzed whole cell patch recordings of exocytosis in murine inner hair cells (Moser and Beutner 2000).

Our BK channel simulations were carried out in a range of fast buffer concentrations, from 0.0 to 8.0mM BAPTA, providing a dose response characterization of buffer concentration on local calcium concentration. We were then able to compare the relative effectiveness of 100 $\mu$ m EGTA and 4.8mM Calretinin to the various BAPTA concentrations. Calretinin has been identified as a potential endogenous buffer in the saccular hair cell (Edmonds et al 2000) at a concentration of 1.2mM. Recombinant Calretinin has five binding sites (Schwaller et al. 1997; Stevens and Rogers 1997), four of which are high affinity with a  $K_d$  of 1.5 $\mu$ m. We simplify our Calretinin model by ignoring cooperativity between the binding sites, thereby modeling the four equivalent sites by increasing the buffer

concentration by a factor of four. Our exocytosis simulations (Fig 6, 7) compared the effects of the slow buffer EGTA (100 $\mu$ M and 5.0mM, both suggested by Moser and Beutner (2000), the endogenous buffer Calretinin, and its two closest kinetic equivalents in BAPTA, 0.8 and 1.6mM.

### Stochastic Components:

**Channel gating.** Stochastic modeling of single channel gating with appropriate dwell times was necessary to elicit appropriate spatiotemporal calcium gradients to drive physiological-like response at low stimulation levels, such as spontaneous activity of the afferent fiber. Our stochastic model of single channel gating was based on experimental evidence of spatial channel distribution, single channel open probabilities, and dwell time distributions. We distributed 84 calcium channels in voxels at the plasma membrane according to Robert's (1994) analysis of freeze-fracture electron microscopy data (Roberts et al. 1990). Single channel recordings (Rodriguez-Contreras and Yamoah 2001,2003) provided evidence that saccular hair cell L-type calcium channels have no more than a 0.4 maximum open probability ( $P_{max}$ ) and dwell time distributions described by the sum of three exponentials. We used their maximum open probability and dwell time descriptions to shape the stochastic nature of single channel opening and closing in our model. Unfortunately, kinetic data on single calcium channels in the hair cell was not available over a wide range of potentials. Thus, our stochastic model of channel gating was necessarily guided by our deterministic solution of whole cell calcium current activation. At each sampled time point  $t$ , the number of open channels in the active zone was determined using Equations 10 and 11.

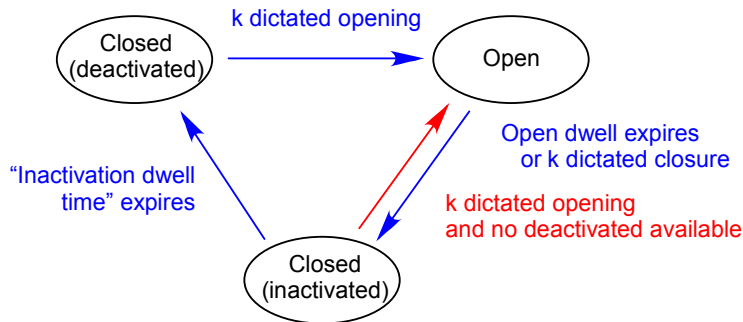
$$(A1.10) \quad P_o(t) = (m(t))^3 \times P_{max}$$

$$(A1.11) \quad \text{Pr}[\# \text{ open channel} = k] = \binom{N}{k} \times (P_o(t))^k \times (1 - P_o(t))^{N-k} \quad \textit{binomial distribution}$$

The single channel open probability ( $P_o$ ) is a function of the deterministic whole cell calcium current activation ( $m^3$ ), and maximum single channel open probability ( $P_{max}$ ). The number of channels opened at each time point ( $k$ ), were described by the binomial distribution, where  $N$  was the number of channels per active zone. We evaluated stochastic channel gating transitions every 250 $\mu$ sec. This was the minimum sampling rate required for good agreement between the time course of single active zone and whole cell currents (Roberts et al. 1990; Issa and Hudspeth 1994).

We complimented this temporal description of how many channels were open with a spatial description of which channels were open based on the available dwell time data (Rodriguez-Contreras and Yamoah 2001). To spatially distribute the open channels, we used a three state model where a channel was either open, deactivated (ready to open), or inactivated (not ready to open). Four state transitions could occur in our model. Channel state transitions occurred for two reasons; the probabilistic number of channels open ( $k$ , Eq 11) dictated a change in the number of open channels, or a channel's computed dwell time in its current state expired. When a channel transitioned to its open state

or inactivated state, its probabilistic dwell time was computed and stored. Below we list each transition our model channels made, and what reasons motivated such state changes.



**Probabilistic Number of Calcium ions.** Stochastic modeling of the instantaneous calcium concentration was also required. At low  $[Ca]$ , such as the resting value of 48nM, the expected number of calcium ions in a  $(40\text{nm})^3$  voxel is far less than 1 (only 0.002). Therefore, at each calcium diffusion time step, we transformed the deterministic calcium concentration ( $[Ca]$ ) into probabilistic number of calcium ions ( $n$ ) according to Equations 12 – 15. We defined a calcium diffusion time step ( $t_{\text{diff}}$ ) as half the voxel dimension squared divided by the calcium diffusion coefficient (Gil et al. 2000). A large scaling factor ( $S$ ), was used to scale even the smallest calcium concentration ( $n$ , with units  $\text{Ca}^{++}$  ions/voxel) to a large whole number ( $N$ ). In practice, we increased the scaling factor according to the concentration by multiples of 1000 until the number of ions exceeded 1000, at which point the rounding error was less than 0.1%. This error was found to be acceptable when comparing stochastic and deterministic solutions. The reciprocal of the scaling factor defined the probability ( $P_1$ ) of finding a single molecule in the voxel. We probabilistically found the number of molecules ( $m$ ) by drawing from the binomial distribution described by  $P_1$  and  $N$ .

$$(A1.12) \quad n = \text{deterministic \# of ions} = [Ca](t) * \text{Avogadro's number} / \text{voxel volume}$$

$$(A1.13) \quad N = \text{scaled integral number of molecules} = \text{round}(n * S) \approx n * S$$

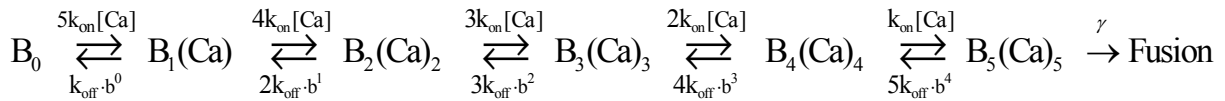
$$(A1.14) \quad \text{Pr}[\text{observing a single molecule per voxel in the scaled concentration}] = P_1 \approx 1 / S$$

$$(A1.15) \quad \text{Pr}[\# \text{ molecules per voxel} = m] = \binom{N}{m} \times (P_1)^m \times (1 - P_1)^{N-m} \quad \textit{binomial distribution}$$

**Calcium Binding and Vesicle Fusion.** Our hybrid model combined the classical deterministic solution of calcium concentration in space and time with a probabilistic description of calcium binding and vesicle fusion. We randomly fixed vesicles in space according to the spatial distributions described by Lenzi et al (1999; 2002). We assigned each vesicle to a voxel based on its spatial location. We modeled calcium dependent exocytosis according to the kinetic model of vesicle fusion described by Beutner (2001). By the law of mass action, we probabilistically

applied this kinetic model to small populations of vesicles contained within each voxel. The population size per voxel varied from 1 to >20 vesicles.

At each calcium diffusion time step, we calculated all calcium dependent rate constants using the number of calcium ions found probabilistically. Following is a schematic of Beutner's kinetic model.



The population of vesicles with 0 to 5 calcium ions bound are represented by  $B_0$  to  $B_5(\text{Ca})_5$ . The on rates  $k_{\text{on}1}$  and  $k_{\text{on}2}$  are calcium dependent. Based on such rate constants, we described the probability of a single vesicle transitioning to the right (binding a  $\text{Ca}^{++}$  ion) or transitioning to the left (unbinding a  $\text{Ca}^{++}$  ion). By the law of mass action, we expressed the probability of a single vesicle with one Calcium ion bound ( $B_1(\text{Ca})$ ), as follows:

$$(A1.16) \quad \text{Pr}[B_1 \text{ transitions left to } B_0] = P_L = \frac{\Delta B_{1\text{-left}}}{[B_1]} = k_{\text{off}} \Delta t$$

$$(A1.17) \quad \text{Pr}[B_1 \text{ transitions right to } B_2] = P_R = \frac{\Delta B_{1\text{-right}}}{[B_1]} = 4k_{\text{on}}[\text{Ca}] \Delta t$$

The probability a single vesicle in state  $B_1$  would transition right or left was expressed as a function of the respective rate constant and the time step ( $\Delta t$ ) under consideration (Gil et al. 2000). This single vesicle transition probability was applied to all vesicles in the state  $B_1$  using the binomial distribution. To avoid transition preference, we randomly chose which transition to evaluate first at each time step. We initially set the time step to the calcium diffusion time step, but reduced it as necessary such that the maximum probability of any transition during the time step was less than 0.1 (empirically determined necessary for convergence by (Gil et al. 2000)).

We extended the above example to all five binding steps and the calcium independent fusion step described in Beutner's (2001) kinetic model. We solved probabilistic kinetics for each vesicle in our model, continually updating the calcium concentration according to equations 12 – 15. We verified our implementation against a standard deterministic implementation that solved differential equations to describe exocytosis of populations of vesicles subjected to the same calcium concentration profile.

### Program Structure:

All computations and data structures were been implemented in C (LabWindows/CVI, National Instruments) and carried out on multiple 1-8 – 2.4GHz Pentium workstations. The programmatic flow was as follows, with designated computation times for a 25msec exocytosis simulation:

- I. *Deterministic*– whole cell calcium current activation based on membrane voltage fluctuations with respect to time (< 1 second )

- II. *Stochastic*– channel gating ( < 1 second )
- III. *Deterministic*– buffered calcium diffusion computation ( ~4 hours )
  - Save calcium concentration profiles to disk ( ~40 Mbytes )
- IV. *Stochastic*– calcium binding and vesicle fusion ( ~10 minutes )
  - Output results to text file for graphing an further analysis

We numerically solved all differential equations using a 5<sup>th</sup> order Ruge-Kutta algorithm. Uniform and binomial deviates were drawn according to the methods described in *Numerical Recipes in C* (Press et al 2<sup>nd</sup> edition). We used Matlab 6.5 (Mathworks) for creating three dimensional vesicle distributions and graphical analysis of calcium profiles in the active zone.

To predict the whole cell behavior of a frog saccular hair cell, we scaled the exocytic out put of a single active zone by populating it with 19 times the number of expected vesicles (Lenzi et al. 1999; Lenzi et al. 2002). Exocytosis plots represent the average and standard error from multiple scaled active zone simulations. We simulated exocytosis for each buffer and voltage condition 50 times; we saved 5 buffered diffusion files to disk, then simulated exocytosis based on 5 scaled vesicle distributions, with 2 probabilistic exocytosis trials a per combination. Therefore, variation in the exocytosis output was introduced from three sources; variations in the spatio-temporal active zone calcium profile introduced by stochastic channel gating, variations in the random vesicle distributions, and variations introduced by stochastic modeling of exocytosis.

### Literature Cited in Appendix 1:

- Beutner, D., Voets, T., Neher, E. and Moser, T. (2001). Calcium Dependence of Exocytosis and Endocytosis at the Cochlear Inner Hair Cell Afferent Synapse. *Neuron* 29(3): 681-90.
- Doyle, D.A., Morais Cabral, J., Pfuetzner, R.A., Kuo, A., Gulbis, J.M., Cohen, S.L., Chait, B.T. and Mackinnon, R. (1998). The Structure of the Potassium Channel: Molecular Basis of K<sup>+</sup> Conduction and Selectivity. *Science* 280(5360): 69-77.
- Edmonds, B., Reyes, R., Schwaller, B. and Roberts, W.M. (2000). Calretinin Modifies Presynaptic Calcium Signaling in Frog Saccular Hair Cells. *Nature Neuroscience* 3(8): 786-90.
- Gil, A., Segura, J., Pertusa, J.A. and Soria, B. (2000). Monte Carlo Simulation of 3-D Buffered Ca(2+) Diffusion in Neuroendocrine Cells. *Biophys J* 78(1): 13-33.
- Hackney, C.M., Mahendrasingam, S., Jones, E.M. and Fettiplace, R. (2003). The Distribution of Calcium Buffering Proteins in the Turtle Cochlea. *J Neurosci* 23(11): 4577-89.
- Hall, J.D., Betarbet, S. and Jaramillo, F. (1997). Endogenous Buffers Limit the Spread of Free Calcium in Hair Cells. *Biophys J* 73(3): 1243-52.
- Heller, S., Bell, A.M., Denis, C.S., Choe, Y. and Hudspeth, A.J. (2002). Parvalbumin 3 Is an Abundant Ca<sup>2+</sup> Buffer in Hair Cells. *J Assoc Res Otolaryngol*.
- Hudspeth, A.J. and Lewis, R.S. (1988). Kinetic Analysis of Voltage- and Ion-Dependent Conductances in Saccular Hair Cells of the Bull-Frog, *Rana Catesbeiana*. *Journal of Physiology-London* 400: 237-74.

- Issa, N.P. and Hudspeth, A.J. (1994). Clustering of Ca<sup>2+</sup> Channels and Ca(2+)-Activated K<sup>+</sup> Channels at Fluorescently Labeled Presynaptic Active Zones of Hair Cells. *Proceedings of the National Academy of Sciences* 91: 7578-7582.
- Kidd, R.C. and Weiss, T.F. (1990). Mechanisms That Degrade Timing Information in the Cochlea. *Hear Res* 49(1-3): 181-207.
- Lenzi, D., Crum, J., Ellisman, M.H. and Roberts, W.M. (2002). Depolarization Redistributes Synaptic Membrane and Creates a Gradient of Vesicles on the Synaptic Body at a Ribbon Synapse. *Neuron* 36(4): 649-59.
- Lenzi, D., Runyeon, J.W., Crum, J.W., Ellisman, M.H. and Roberts, W.M. (1999). Synaptic Vesicle Populations in Saccular Hair Cells Reconstructed by Electron Tomography. *Journal of Neuroscience* 19: 119-132.
- Lumpkin, E.A. and Hudspeth, A.J. (1998). Regulation of Free Ca<sup>2+</sup> Concentration in Hair-Cell Stereocilia. *Journal of Neuroscience* 18(16): 6300-18.
- Moser, T. and Beutner, D. (2000). Kinetics of Exocytosis and Endocytosis at the Cochlear Inner Hair Cell Afferent Synapse of the Mouse. *Proceedings of the National Academy of Sciences* 97(2): 883-8.
- Roberts, W.M. (1993). Spatial Calcium Buffering in Saccular Hair Cells. *Nature* 363(6424): 74-6.
- Roberts, W.M. (1994). Localization of Calcium Signals by a Mobile Calcium Buffer in Frog Saccular Hair Cells. *Journal of Neuroscience* 14(5 Pt 2): 3246-3262.
- Roberts, W.M., Jacobs, R.A. and Hudspeth, A.J. (1990). Colocalization of Ion Channels Involved in Frequency Selectivity and Synaptic Transmission at Presynaptic Active Zones of Hair Cells. *Journal of Neuroscience* 10(11): 3664-3684.
- Rodriguez-Contreras, A. and Yamoah, E.N. (2001). Direct Measurement of Single-Channel Ca(2+) Currents in Bullfrog Hair Cells Reveals Two Distinct Channel Subtypes. *J Physiol* 534(Pt 3): 669-89.
- Rodriguez-Contreras, A. and Yamoah, E.N. (2003). Effects of Permeant Ion Concentrations on the Gating of L-Type Ca<sup>2+</sup> Channels in Hair Cells. *Biophys J* 84(5): 3457-69.
- Schwaller, B., Durussel, I., Jermann, D., Herrmann, B. and Cox, J.A. (1997). Comparison of the Ca<sup>2+</sup>-Binding Properties of Human Recombinant Calretinin-22k and Calretinin. *J Biol Chem* 272(47): 29663-71.
- Stevens, J. and Rogers, J.H. (1997). Chick Calretinin: Purification, Composition, and Metal Binding Activity of Native and Recombinant Forms. *Protein Expr Purif* 9(2): 171-81.
- Wu, Y.C., Tucker, T. and Fettiplace, R. (1996). A Theoretical Study of Calcium Microdomains in Turtle Hair Cells. *Biophysical Journal* 71(5): 2256-2275.

# Modeling hair cell exocytosis using a hybrid deterministic-stochastic implementation

John H Wittig Jr and Thomas D. Parsons

University of Pennsylvania, Philadelphia, PA 19104



## Introduction

**Modeling Aims**

We present a novel computational modeling approach to simulate the synaptic details of a bullfrog saccular hair cell. Our model focuses on a single pre-synaptic active zone, and addresses calcium influx, buffered calcium diffusion, and exocytosis. Our aims are to create a **comprehensive and detailed** computational model of hair cell exocytosis that:

- Unifies disparate experimental paradigms:**
  - Voltage clamp exocytosis (Parsons et al 1994, Moser and Beutner 2000)
  - Flash photolysis of caged calcium (Beutner et al 2001)
  - Spontaneous rates of VIII<sup>th</sup> nerve
  - Evoked response of VIII<sup>th</sup> nerve
- Considers anatomical details of the synapse:**
  - Distribution of vesicles about the dense body (Lenzi et al 1999, 2002)
  - Possible distributions of calcium channels (Roberts et al 1990, Roberts 1994, Wu et al 1996, Rodriguez-Contreras and Yamoah 2001)
- Considers physiological details of the synapse:**
  - Gating and single channel conductance of calcium channels (Rodriguez-Contreras and Yamoah 2001, 2003)
  - Movement of vesicles toward the active zone (Zenisek et al 2002)
- Remains founded in whole cell kinetic analysis:**
  - Activation of calcium current (Hudspeth and Lewis 1988)
  - Calcium buffering (Roberts 1993, Tucker and Fettiplace 1996, Ricci et al 1998, Moser and Beutner 2001)
  - Calcium dependent exocytosis (Beutner et al 2001)

## Methods

**Modeling Details**

**Geometrical considerations**  
We considered a cytoplasmic "active zone volume" of 3.2 x 3.2 x 1.6 nm. This volume was bounded against a planar plasma membrane surface, with one complete active zone at its center. We discretized the active zone volume into thousands of cubical volume elements (voxels), for numerical evaluation purposes. We used multiple voxel sizes to efficiently model the active zone volume, with small voxels closer to the active zone center and large voxels further away. When modeling exocytosis, where the diameter of vesicles is approximately 40 nm (Lenzi et al 1999), we used a minimum voxel size of (40 nm)<sup>3</sup> closest to the active zone center, and up to (320 nm)<sup>3</sup> at the edges of the array (left schematic). When modeling the activation of BK channels we used a minimum voxel size of (10 nm)<sup>3</sup>, based on the dimension of the channel mouth (Doyle et al 1998).

**Deterministic Components**  
Both deterministic components were solved by solving differential equations defined by the respective kinetic equations. Solutions to whole cell current activation and buffered diffusion of calcium have been described in detail by others (Hudspeth and Lewis 1988, Roberts 1994), following is a recapitulation of the kinetic equations solved (Eq 1-4).

$$(1) \frac{d[Ca]_{act}}{dt} = \frac{d[Ca]_{influx}}{dt} - \frac{d[Ca]_{outflux}}{dt} + \frac{d[Ca]_{influx}}{dt} - \frac{d[Ca]_{outflux}}{dt}$$

$$(2) \frac{d[Ca]_{influx}}{dt} = N_{channels}(t) \cdot G_{max} [V_{mem}(t) - E_{Ca}] = \frac{I_{Ca}(t)}{Z_{Ca} \cdot F \cdot Volume_{act}}$$

$$(3) \frac{d[Ca]_{outflux}}{dt} = D_{Ca} \nabla^2 [Ca] - D_{Ca} \frac{\partial^2 [Ca]}{\partial x^2} + \frac{\partial^2 [Ca]}{\partial x^2}$$

$$(4) \frac{d[Ca]_{influx}}{dt} = k_{on} [FB-Ca] - k_{off} [F][Ca] + k_{on} [MB-Ca] - k_{off} [M][Ca]$$

**Calcium Channel Gating**  
L-type calcium channels in the hair cell have not been completely characterized at the single channel level. Rodriguez-Contreras and Yamoah (2001) have described the distribution of open and closed dwell times at a single holding potential and the maximum open probability P<sub>max</sub>. Therefore we use our deterministic solution of whole cell I<sub>Ca</sub> activation to calculate single channel open probability, then randomly choose which channels undergo transitions based on Rodriguez-Contreras's dwell time distributions.

- Probabilistically find number of open channels, *k*, every 250μsec based on deterministic activation parameter, *m* (Eq 5-8)
- Randomly choose which channels to transition based on their states (depicted below)
- Probabilistically find new open/closed dwell times based on Rodriguez-Contreras's distributions

(5) Whole Cell I<sub>Ca</sub> = *G*<sub>max</sub> × *m* × (V<sub>mem</sub> - E<sub>Ca</sub>)

(6)  $\frac{dm}{dt} = \alpha(1-m) - \beta m$

(7) Open Probability = P<sub>o</sub>(t) = (m<sub>o</sub>)<sup>k</sup> × P<sub>max</sub>

(8)  $Pf[\text{open channel}] = \sum_{k=0}^{\infty} (P_o(t))^k \times (1 - P_o(t))^{N-k}$

**Number of calcium ions**  
When considering small volumes, deterministic calcium concentrations translate to fractions of calcium ions per voxel. A single calcium ion is predicted when deterministic concentrations are 25.95 μM for a (40 nm)<sup>3</sup> voxel, yet 13.28 mM for a (5 nm)<sup>3</sup> voxel! The quanta of calcium ion associated with a deterministic concentration fluctuates stochastically as calcium undergoes Brownian motion. We iteratively find the quantal number of calcium ions in each voxel at each calcium diffusion time step, which is half the voxel dimension squared divided by the calcium diffusion coefficient (1.3 μsec (40 nm)<sup>2</sup>; 2 nsec (5 nm)<sup>2</sup>).

- Find deterministic number of Ca ions = *n* = [Ca] × Avagadro's number / voxel volume
- Scale up volume to make *n* large, so it can be approximated by an integer number *N*
- Use binomial to find the number of ions expected in the pre-scaled volume

**Calcium binding and exocytosis**  
We stochastically model calcium dependent exocytosis based on the six state model of Beutner et al 2001. Their model includes five calcium binding steps, and one irreversible fusion step (Eq 9). We convert the kinetic model to a stochastic model based on the law of mass action. Example probabilities are shown for transitions from a single state (Eq 10-11)

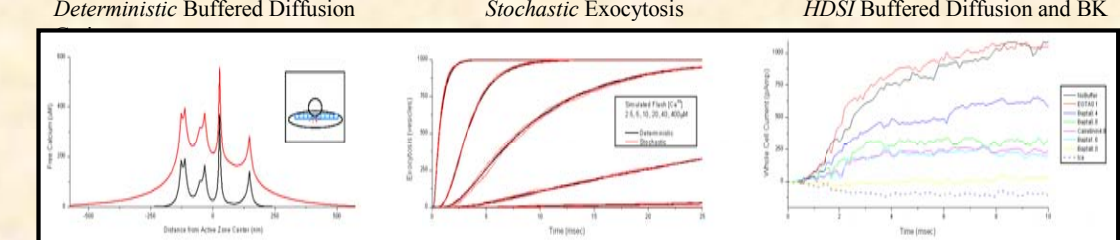
- Quantal number of calcium ions are found based on deterministic solution (see above)
- Calcium dependent forward and backward rates are converted to probabilities
- Time step is reduced so no probability exceeds 0.1 (Gil et al 2000).
- Binomial deviates are drawn based on the respective transition probabilities and number of vesicles in the state under consideration

$$(9) B_0 \xrightleftharpoons[k_{off}]{k_{on}} B_1(Ca) \xrightleftharpoons[k_{off}]{k_{on}} B_2(Ca) \xrightleftharpoons[k_{off}]{k_{on}} B_3(Ca) \xrightleftharpoons[k_{off}]{k_{on}} B_4(Ca) \xrightleftharpoons[k_{off}]{k_{on}} B_5(Ca) \xrightarrow{k_{fusion}} Fusion$$

$$(10) Pf[\text{transitions left to } B_1] = P_1 = \frac{M_1 \cdot [Ca]}{[B_1]}$$

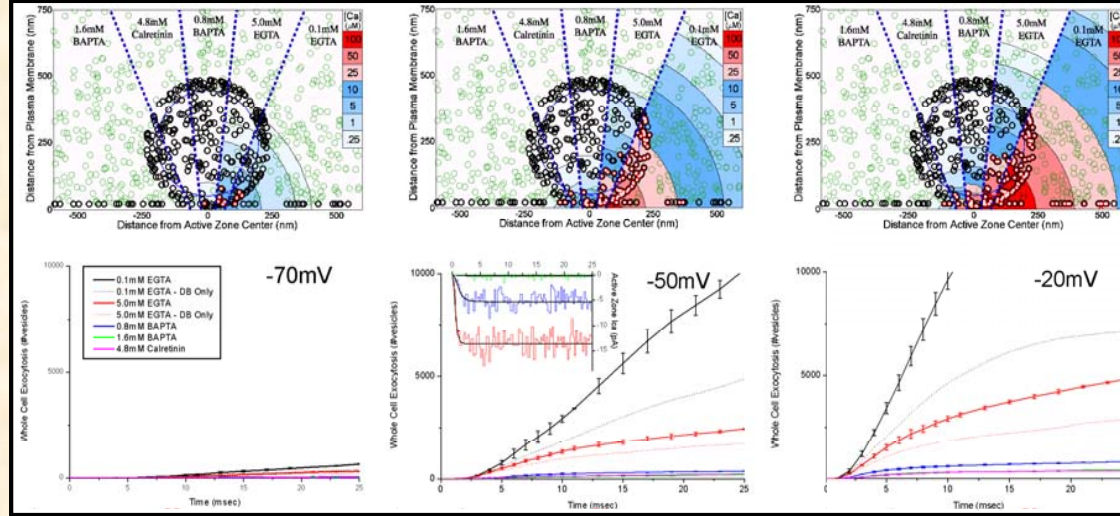
$$(11) Pf[\text{transitions right to } B_1] = P_1 = \frac{M_1 \cdot [Ca]}{[B_1]} = 4k_{on} [Ca] M$$

## Technique Verification

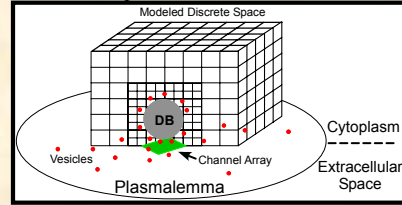


## Exocytosis Predictions

[Ca<sup>2+</sup>] profiles and time course of exocytosis elicited by voltage clamp steps from -75mV



### Discrete space and time at the active



### Methods Overview

**Hybrid Deterministic-Stochastic Implementation (HDSI)**

**Deterministic Components:**

- Whole cell calcium current activation (Hudspeth and Lewis 1988)
- Buffered Diffusion (Roberts 1994)

**Stochastic Components:**

- Calcium channel gating
- Conversion of deterministic [Ca<sup>2+</sup>] to number of calcium ions
- Calcium binding and vesicle fusion

**Program Structure** – 25 msec v-clamp simulation (run time on 1.8 GHz P4):

- *Deterministic* – whole cell, voltage dependent calcium current activation (<1 sec)
- *Stochastic* – channel gating (<1 sec)
- *Deterministic* – buffered calcium diffusion computation (~4 hours)
- *Stochastic* – save results to disk (~40 MBytes)
- *Stochastic* – calcium binding and vesicle fusion (~10 min)
- *Stochastic* – output results to text file for graphing and further analysis

## Summary

**Deterministic vs Stochastic**

- Deterministic modeling simulates continuous processes and seeds stochastic processes – buffered diffusion and I<sub>Ca</sub> activation
- Stochastic modeling simulates discrete processes - channel gating, calcium binding, and vesicle fusion

**Exocytosis Buffering Conditions**

- Proposed endogenous buffer (4.8mM Calretinin, Edmonds et al 2000) mediates exocytic response between 0.8 mM and 1.6 mM BAPTA, as predicted by Roberts (1993)
- Weak buffering conditions reported by Moser and Beutner (2000) yields radically different time course and absolute levels of exocytosis than proposed endogenous buffer

**Features of the HDSI Technique**

- Generally applicable technique that can be used to simulate wide range of conditions
- Stochastic components required for simulations with low probability (i.e. spontaneous release, or central synapses with few vesicles)
- Stochastic components required for modeling non-stationary [Ca<sup>2+</sup>] (i.e. from sinusoidal or sound evoked depolarizations)
- Uses deterministic solutions as basis for stochastic process modeling when sufficiently detailed data is not available

## Appendix 2: Parameters of Bushy Cell Conductances

The following descriptions of Bushy cell conductances were reported by Rothman and Manis (2003). Where the reversal potentials are:  $V_K = -80$  mV,  $V_{Na} = +55$  mV,  $V_h = -43$  mV, and  $V_{lk} = -65$  mV. The maximum value for each conductance is listed below, followed by equations governing their magnitude and time course of activation.

$\bar{g}_{LT}$	$\bar{g}_{HT}$	$\bar{g}_{Na}$	$\bar{g}_h$
200nS	150nS	1000nS	20nS

### Low-threshold $K^+$ current

$$\begin{aligned}
 I_{LT} &= \bar{g}_{LT} \cdot w^4 z \cdot (V - V_K) \\
 w_\infty &= [1 + \exp(-(V + 48)/6)]^{-1/4} \\
 z_\infty &= (1 - \zeta) \cdot [1 + \exp((V + 71)/10)]^{-1} + \zeta \quad (\zeta = 0.5) \\
 \tau_w &= 100 \cdot [6 \exp((V + 60)/6) + 16 \exp(-(V + 60)/45)]^{-1} + 1.5 \\
 \tau_z &= 1000 \cdot [\exp((V + 60)/20) + \exp(-(V + 60)/8)]^{-1} + 50
 \end{aligned}$$

### High-threshold $K^+$ current

$$\begin{aligned}
 I_{HT} &= \bar{g}_{HT} \cdot [\varphi n^2 + (1 - \varphi)p] \cdot (V - V_K) \quad (\varphi = 0.85) \\
 n_\infty &= [1 + \exp(-(V + 15)/5)]^{-1/2} \\
 p_\infty &= [1 + \exp(-(V + 23)/6)]^{-1} \\
 \tau_n &= 100 \cdot [11 \exp((V + 60)/24) + 21 \exp(-(V + 60)/23)]^{-1} + 0.7 \\
 \tau_p &= 100 \cdot [4 \exp((V + 60)/32) + 5 \exp(-(V + 60)/22)]^{-1} + 5
 \end{aligned}$$

### Fast $Na^+$ current

$$\begin{aligned}
 I_{Na} &= \bar{g}_{Na} \cdot m^3 h \cdot (V - V_{Na}) \\
 m_\infty &= [1 + \exp(-(V + 38)/7)]^{-1} \\
 h_\infty &= [1 + \exp((V + 65)/6)]^{-1} \\
 \tau_m &= 10 \cdot [5 \exp((V + 60)/18) + 36 \exp(-(V + 60)/25)]^{-1} + 0.04 \\
 \tau_h &= 100 \cdot [7 \exp((V + 60)/11) + 10 \exp(-(V + 60)/25)]^{-1} + 0.6
 \end{aligned}$$

### Hyperpolarization-activated cation current

$$\begin{aligned}
 I_h &= \bar{g}_h \cdot r \cdot (V - V_h) \\
 r_\infty &= [1 + \exp((V + 76)/7)]^{-1} \\
 \tau_r &= 10^5 \cdot [237 \exp((V + 60)/12) + 17 \exp(-(V + 60)/14)]^{-1} + 25
 \end{aligned}$$

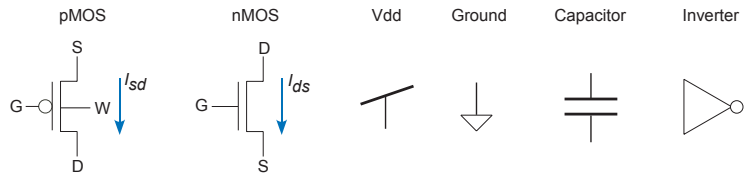
### Appendix 3: Circuit Model of Class Chip Neuron with $K_{LT}$

#### Circuit elements and sub-threshold current equations

Circuit schematics in Appendices 3 and 4 use the six design elements shown to the right.

Metal-Oxide-Silicon field effect transistors (MOS-

FET) come in two flavors; pMOS transistors conduct holes, while nMOS transistors conduct electrons. The fabrication process currently used in Dr. Boahen's lab starts with p-type silicon that is doped with ions that donate holes. The conduction channel in a pMOS device is n-type (doped with ions that donate electrons), so each pMOS transistor is within an n-type well, resulting in a four terminal device. In contrast, the nMOS conduction channel is formed from the p-type doping that makes up the bulk of the silicon. The bulk is grounded, so nMOS transistors are three terminal devices. MOS-FET terminals include the gate (G), source (S), drain (D) and well (W). In general, if the well terminal is not specified in a circuit diagram, it is connected to Vdd. Vdd is the power supply voltage on chip; the 0.25 $\mu$ m process currently used in lab is optimized for a Vdd of 2.5V. Ground is the low voltage point on chip, which we designate as 0V such that all voltages are in reference to ground. An inverter is constructed by stacking a pMOS and nMOS transistor so their gates are connected (the inverter input) and their drains are connected (the inverter output). This configuration is used frequently in digital circuitry, where signals are abstracted to zeros (Ground) and ones (Vdd). If the input to an inverter is zero, its output is one, and vice versa.



The equations describing sub-threshold transistor current ( $I_{sd}$  and  $I_{ds}$ ) as a function of the voltages at each terminal are given below. Sub-threshold operation occurs when there is relatively little voltage difference between a transistor's gate and source. This regime of operation produces very small currents, ranging from  $10^{-15}$  to  $10^{-8}$  Amps, which are exponentially related to the voltages at each terminal. We design a majority of our circuits to operate sub-threshold for three reasons: small currents minimize power consumption, small currents enable the use of small capacitors when creating temporal filters, and the exponential relationship between voltage and current provides a convenient tool for modeling many biological phenomena. Above threshold currents are related to the square of the terminal voltages. As our modeling technique rarely considers above-threshold current relations, those equations are not provided in this document.

$$\begin{aligned} \text{pMOS } I_{sd} &= I_o \left( \frac{w}{L} \right) \left( e^{\frac{\kappa(V_w - V_g) - (V_w - V_s)}{u_t}} - e^{\frac{\kappa(V_w - V_g) - (V_w - V_d)}{u_t}} \right) \\ I_{sd-sat} &= I_o \left( \frac{w}{L} \right) e^{\frac{\kappa(V_w - V_g) - (V_w - V_s)}{u_t}} ; \quad \{V_s \geq V_d + 4u_t\} \end{aligned}$$

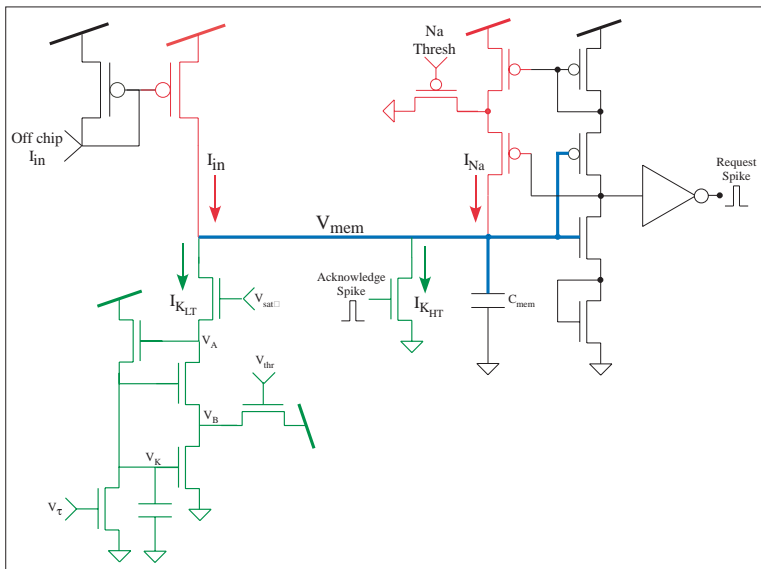
$$\begin{aligned} \text{nMOS } I_{ds} &= I_o \left( \frac{w}{L} \right) \left( e^{\frac{\kappa V_g - V_s}{u_t}} - e^{\frac{\kappa V_g - V_d}{u_t}} \right) \\ I_{ds-sat} &= I_o \left( \frac{w}{L} \right) e^{\frac{\kappa V_g - V_s}{u_t}} ; \quad \{V_d \geq V_s + 4u_t\} \end{aligned}$$

When operating sub-threshold the transistor currents ( $I_{sd}$  and  $I_{ds}$ ) are exponentially related to the gate, source, drain, and well voltages ( $V_g$ ,  $V_s$ ,  $V_d$ , and  $V_w$ , respectively). In the above equations, each device is further characterized by the device-dependent constants  $\kappa$ ,  $I_o$ , and the device's dimensions (width and length). Thermal voltage  $u_t$  is approximately 26mV at room temperature. I have characterized long (1/10 W/L) pMOS and nMOS transistors from a test chip and found  $I_o = 0.083\text{pA}$  and  $\kappa = 0.69$  for the pMOS, while  $I_o = 5.6\text{pA}$  and  $\kappa = 0.79$  for the nMOS transistor.

For the two long transistors measured, the transition from sub-threshold to above threshold occurred at 0.56V  $V_{gs}$  ( $I_{ds}$  is 12nA) for pMOS and 0.38V  $V_{gs}$  ( $I_{ds}$  is 36nA) for nMOS. Not only are these parameters different for pMOS and nMOS transistor types, they also vary among transistors of the same type due to process variability during fabrication. When the voltage difference between drain and source terminals exceeds approximately  $4u_t$  ( $\sim 100\text{mV}$ ) the transistors operate in saturation. The simplified saturation equations are also shown above. Frequently our analyses utilize these saturation equations.

## General description of the class chip auditory neuron

Throughout the rest of this appendix section, I describe the design and characterization of a silicon auditory neuron fabricated in Dr. Boahen's laboratory. It is an integrate-and-fire neuron model with the addition of a low threshold potassium current designed by Dr. Boahen. This is the circuit design of the spiral ganglion cells in B. Wen's silicon cochlea that convert the response of her basilar membrane to spiking output using the Address Event Representation (AER). An isolated spiral ganglion neuron has been reproduced on an instructional chip used in Dr. Boahen's class (henceforth referred to as the class chip) fabricated in 2003. The class chip auditory neuron shown in Figure A3.1 has several features that enable its characterization; it can be directly excited with injected current ( $I_{in}$ ), it is self resetting (Request Spike and Acknowledge Spike are connected on chip with a delay), and both  $V_{mem}$  and  $I_{KLT}$  are conveyed off chip for mock *in vitro* characterization. The colors in this simplified representation of neuron circuit indicate  $V_{mem}$  (blue) and the transistors that implement  $V$  depolarizing currents (red) and repolarizing currents (green).

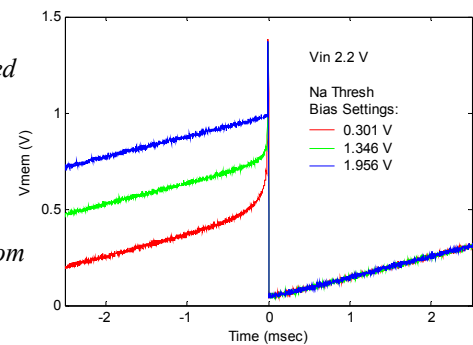


**A3.1: Simplified circuit diagram of class chip auditory neuron** The membrane capacitor ( $C_{mem}$ ) integrates four currents: input current ( $I_{in}$ ) driven from an off-chip source, positive feedback sodium current ( $I_{Na}$ ), post-spike repolarizing potassium current ( $I_{KHT}$ ), and the low-threshold potassium current ( $I_{KLT}$ ). Increasing membrane voltage ( $V_{mem}$ ) activates both  $I_{Na}$  and  $I_{KLT}$ .  $Na$  Thresh adjusts the threshold of  $I_{Na}$  activation.  $V_{\tau}$ ,  $V_{thr}$ , and  $V_{sat}$  affect  $I_{KLT}$  function. The bias controlling  $V_{sat}$  is inverted. Throughout the text I refer to this inverted input as  $V_{sat}$  such that when  $V_{sat}$  is 0V,  $V_{sat}$  is 2.5V and the channel is fully enabled.  $V_{dd}$  for this chip is 2.5V.

The spiking mechanism of this neuron operates as follows. At resting  $V_{mem}$  is 0V. Assuming  $I_{KLT}$  is disabled, when  $I_{in}$  is non-zero, current is linearly integrated on the membrane capacitor ( $C_{mem}$ ). As  $V_{mem}$  increases, current passes through the nMOS and pMOS transistors connected in series to the right of the circuit. The top red pMOS

mirrors this current. When this mirrored current surpasses the sodium threshold set by Na Thresh,  $I_{Na}$  dumps current onto  $V_{mem}$ , further increasing it. This creates a positive feedback loop mimicking the depolarizing phase of an action potential. At a high enough value,  $V_{mem}$  triggers a switch in the digital circuitry represented by the inverter symbol, which in this particular neuron leads to the delayed activation of  $I_{KHT}$  which pulls  $V_{mem}$  back to 0V thus resetting the neuron. Na Thresh is a bias setting controlled off chip, which makes this neuron's spike threshold adjustable. In Figure A3.2, I demonstrate the effect of adjusting Na Thresh. The spike width in a standard silicon neuron is determined by the time it takes the transmitter circuitry to acknowledge the spike request, which can range from nanoseconds to microseconds depending on communication bandwidth. The circuitry of this self-resetting neuron has been adjusted to produce a spike width of 5ns, mimicking operation under low-activity conditions. With such a short spike width,  $V_{mem}$  does not actually reach the Vdd during a spike; in this case it peaks at approximately 1.3V as observed in the figure.

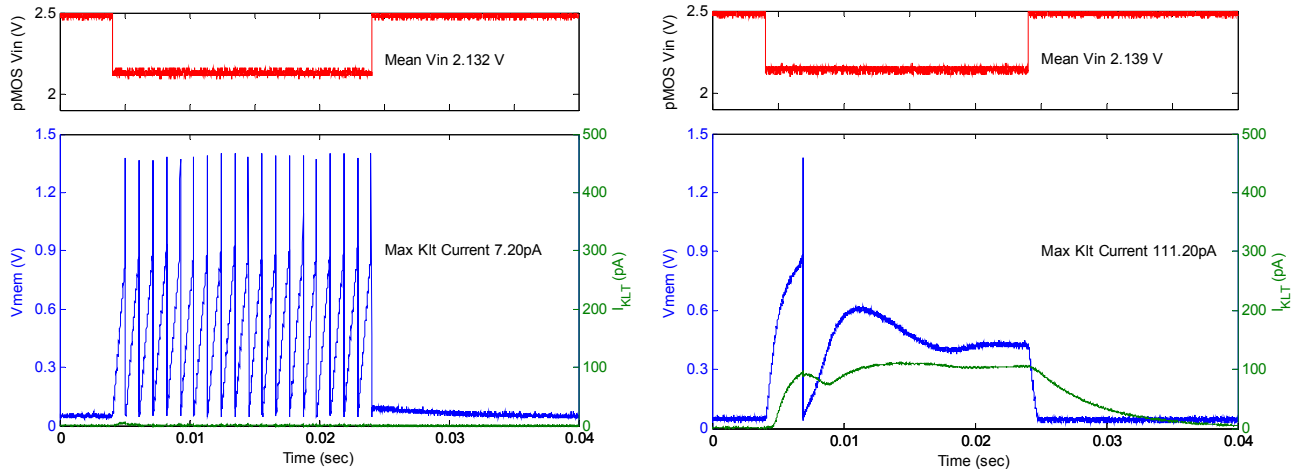
**A3.2: Adjustable sodium threshold in silicon** Oscilloscope traces of  $V_{mem}$  captured from the class chip showing how adjusting the Na Thresh bias affects spike threshold with  $I_{KLT}$  disabled ( $V_{sat}$  is 2.5V). The voltage applied to the input pMOS is 2.2V. Spike threshold ranges from approximately 0.5 to 1V in this figure. This integrate-and-fire neuron has a linear trajectory of  $V_{mem}$  until positive feedback from  $I_{Na}$  activates giving it an upward curvature immediately preceding a spike.



Enabling  $I_{KLT}$  significantly affects the response of this neuron to a step injection of depolarizing current. In Figure A3.3, I show the response of the auditory neuron to a step increase in current when  $I_{KLT}$  is disabled (left), and when it is enabled (right). The integrate-and-fire response is characterized by a constant spike rate during current injection, linear trajectory of  $V_{mem}$  before  $I_{Na}$  activates, and a slow return to baseline when current injection ceases. In contrast, this neuron's response resembles that of a biological bushy cell when  $I_{KLT}$  is enabled (right). The step increase in injected current causes a rapid depolarization (increase) of the  $V_{mem}$  leading to a single spike (blue trace) until  $I_{KLT}$  sufficiently activates (green trace) to shunt the input current and prevent multiple spikes. As  $I_{KLT}$  is temporally filtered, its activation lags behind  $V_{mem}$ , such that the  $V_{mem}$  and  $I_{KLT}$  traces are out of phase initially. By the end of the 20msec current injection,  $I_{KLT}$  perfectly balances all depolarizing currents causing  $V_{mem}$  to stabilize at approximately 0.45V.

### Analysis of the class chip auditory neuron

In this section, I analytically describe the operation of the class chip auditory neuron. First I define the equations governing operation of the simple integrate-and-fire neuron. Then I provide a detailed description of the  $K_{LT}$  circuit. My analytical solutions to the  $K_{LT}$  circuit are compared to data collected from the class chip, namely the steady state I-V curve for the circuit and the time course of  $I_{KLT}$  activation and deactivation.



**A3.3: Oscilloscope traces of the silicon neuron's response to a pulse of current with  $K_{LT}$  disabled and enabled** (left) The response of a leaky integrate-and-fire silicon neuron to a step increase in injected current. When  $V_{in}$  (red trace, top plot) steps from 2.5 to 2.13 V,  $V_{mem}$  (blue trace, left ordinate) spikes repeatedly at a constant rate. When  $V_{in}$  returns to 2.5 V,  $V_{mem}$  slowly returns to its resting level due to various leaks to ground in the circuit – there is no explicit leak transistor.  $I_{KLT}$  is disabled ( $V_{sat}$  is 2.5 V), such that  $I_{KLT}$  (green trace, right ordinate) never exceeds 7.2pA. (right) When  $K_{LT}$  is enabled ( $V_{sat}$  is 1.062 V),  $V_{mem}$  increases at the onset of a current injection and spikes before  $I_{KLT}$  sufficiently activates. A  $V_{in}$  value of 2.139V is this neuron's input threshold; if  $V_{in}$  is increased by a few mV,  $V_{mem}$  does not spike. By the end of the current injection  $V_{mem}$  stabilizes as  $I_{in}$  plus  $I_{Na}$  balance  $I_{KLT}$ . When  $V_{in}$  returns to 2.5V,  $V_{mem}$  quickly drops to its resting value as  $I_{KLT}$  slowly deactivates. The time course of  $I_{KLT}$  deactivation is markedly slower than its activation.  $V_{thr}$  is set to 0V and  $V\tau$  is 100mV. Transient  $I_{KLT}$  was converted to a voltage recorded by the oscilloscope by dropping it across 10M $\Omega$  resistor.  $I_{KLT}$  has additionally been scaled down by an approximate pad gain of 1000.

Equation 1 is the differential equation that describes how  $V_{mem}$  changes with time based on the sum of the currents indicated in Figure A3.1.  $I_{KHT}$  is only active immediately following a spike (during the reset pulse) and doesn't contribute to the change in  $V_{mem}$  during integration. During integration, Equation 2 describes  $V_{mem}(t)$ , given that  $V_{mem}(t)$  remains greater than or equal to 0V and less than the spike threshold  $V_{spike}$ .

$$(A3.1) \quad C_{mem} \frac{dV_{mem}}{dt} = I_{in} + I_{Na} - I_{KLT} - I_{KHT}$$

$$(A3.2) \quad V_{mem}(t) = \frac{1}{C_{mem}} \int_0^t (I_{in}(t) + I_{Na}(t) - I_{KLT}(t)) dt + V_{mem}(0); \quad \left\{ 0 \leq V_{mem}(t) \leq V_{spike} \right\}$$

If the currents are constant,  $V_{mem}(t)$  will have a linear trajectory with a slope defined by the sum of the currents divided by  $C_{mem}$ .  $V_{spike}$  may be defined as the  $V_{mem}$  value that sufficiently activates the positive feedback loop with  $I_{Na}$  such that spiking is inevitable. In Figure A3.2, I define  $V_{spike}$  as the membrane voltage at which the slope of  $V_{mem}(t)$  doubles — this is the voltage at which  $I_{Na}$  equals  $I_{in}$ . If all currents are constant and their sum is positive  $V_{mem}$  will increase to  $V_{spike}$ , cause a spike, reset to ground, then once again increase to  $V_{spike}$  thereby eliciting spikes at a constant frequency as observed in Figure A3.3, left. When time varying currents such as  $I_{KLT}$  are also considered, a fixed  $V_{spike}$  no longer exists. When the slope of  $V_{mem}(t)$  doubles due to  $I_{Na}$  activation, a delayed activation of  $I_{KLT}$  might counteract positive

feedback and inhibit the spike. A better measure of spike threshold with  $I_{KLT}$  enabled is therefore the level of  $I_{in}$  required to elicit a spike during a pulse of input current starting with  $I_{KLT}$  fully deactivated (Figure A3.3).

I analyze the  $K_{LT}$  circuit using the sub-threshold transistor current equations provided earlier in this text. Referring to the neuron schematic in Figure A3.1, the exponential of  $(V_K/u_t)$  varies according to the following differential equation assuming the transistor with  $V_A$  at its gate is in saturation, and  $V_{sat}$  is completely on such that  $V_A$  equals  $V_{mem}$ :

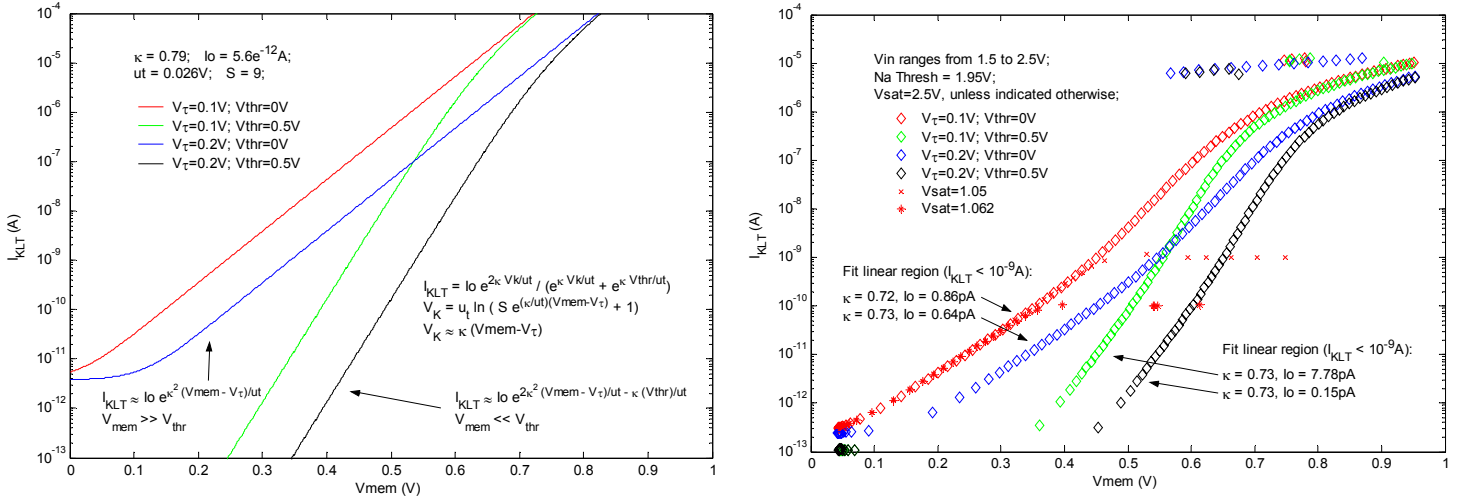
$$(A3.3) \quad \left( \frac{C_{KLT} u_t S}{I_o e^{\kappa V_{\tau}/u_t}} \right) \frac{d e^{V_K/u_t}}{dt} + e^{V_K/u_t} = S e^{\frac{\kappa}{u_t}(V_{mem}-V_{\tau})} + 1$$

Where  $S$  is the length to width ratio of the  $V_{\tau}$  transistor ( $W/L = 1/9$ ),  $C_{KLT}$  is the capacitance of the  $K_{LT}$  capacitor,  $u_t$  is the thermal voltage (26mV at room temperature), and  $\kappa$  is the exponential slope of the nMOS sub-threshold I-V curve (approximately 0.79 for this 0.25 $\mu$ m process). The time constant for this equation ( $\tau_{V_K}$ ) is the leftmost expression in parenthesis. The steady state solution for  $V_K$  shapes the I-V curve of  $I_{KLT}$  according to the following equation:

$$(A3.4) \quad I_{KLT}(t = \infty) = I_o \frac{e^{2\kappa V_K/u_t}}{2e^{\kappa V_K/u_t} + e^{\kappa V_{thr}/u_t}}; \text{ where } V_K = u_t \ln \left( S e^{\frac{\kappa}{u_t}(V_{mem}-V_{\tau})} + 1 \right)$$

In Figure A3.4, I plot the numerical approximation of  $I_{KLT}$  in steady state using the transistor constants measured for an individual nMOS transistor. As  $V_{mem}$  increases,  $I_{KLT}$  increases exponentially. Increasing the bias  $V_{\tau}$  shifts  $I_{KLT}$  downward. This occurs because  $V_K$  cannot increase until the current dumping onto  $C_{KLT}$  is greater than the current being pulled off by the  $V_{\tau}$  transistor. This is predicted in the analytical solution, where  $V_K$  is proportional to  $\kappa(V_{mem} - V_{\tau})$ . Increasing  $V_{thr}$  reduces  $I_{KLT}$  at low  $V_{mem}$ , but also increases the slope of the I-V curve such that I-V curves with the same  $V_{\tau}$  but different  $V_{thr}$  values intersect. This intersection point happens approximately  $4u_t$  above  $V_{thr}$ , when its contribution to the equation for  $I_{KLT}$  becomes negligible. As my theoretical I-V curves are constructed using strictly sub-threshold equations, the exponential relationship between  $I_{KLT}$  and  $V_{mem}$  continues even for  $V_{mem}$  values greater than the recorded nMOS threshold of 0.38V. I measured  $I_{KLT}$  I-V curves from the class chip using the same bias settings considered theoretically (right plot). Qualitatively, theory and chip data agree as  $V_{\tau}$  and  $V_{thr}$  exhibit the predicted effects on  $I_{KLT}$ . Overall the chip currents are lower than those predicted; for low  $V_{mem}$  values, this is likely due to an overestimate of  $I_o$  in my theory plots, or an underestimation of the pad gain in the experimental plots. I fit the linear region of the I-V plots below  $10^{-9}$ A to find approximate  $I_o$  values and  $k$  according to the simplified equations provided in the right plot. Experimental  $\kappa$  ranges from 0.725 to 0.734 among the four curves, while  $I_o$  ranges from 0.145pA to 7.78pA. The two I-V traces with  $V_{thr}$  set to zero yielded  $I_o$  values of 0.63 and 0.85pA, which corroborates with the lower magnitude of these currents compared to my theory which assumed an  $I_o$  value of 5.6pA. For  $V_{mem}$  values greater than approximately 0.4, the chip I-V slopes decrease as the transistor currents are no longer sub-threshold and exponentially related to the voltages at their terminals. The exponential region of the chip data ( $I_{KLT} < 10e^{-9}$ A) has a smaller slope than I predicted, agreeing with the measured values of  $\kappa$  being lower than the value of

0.79 used in my analytical solutions. An additional discrepancy is the set of points at  $10^{-5}$ A that are discontinuous with the rest of the I-V plots. These points resulted from neuron spiking during high current injection levels. Finally, I demonstrate the result of changing  $V_{sat}$ , which effectively limits the maximum  $V_{mem}$  apparent to the  $K_{LT}$  circuitry, thereby causing saturation in output current with increasing  $V_{mem}$ .



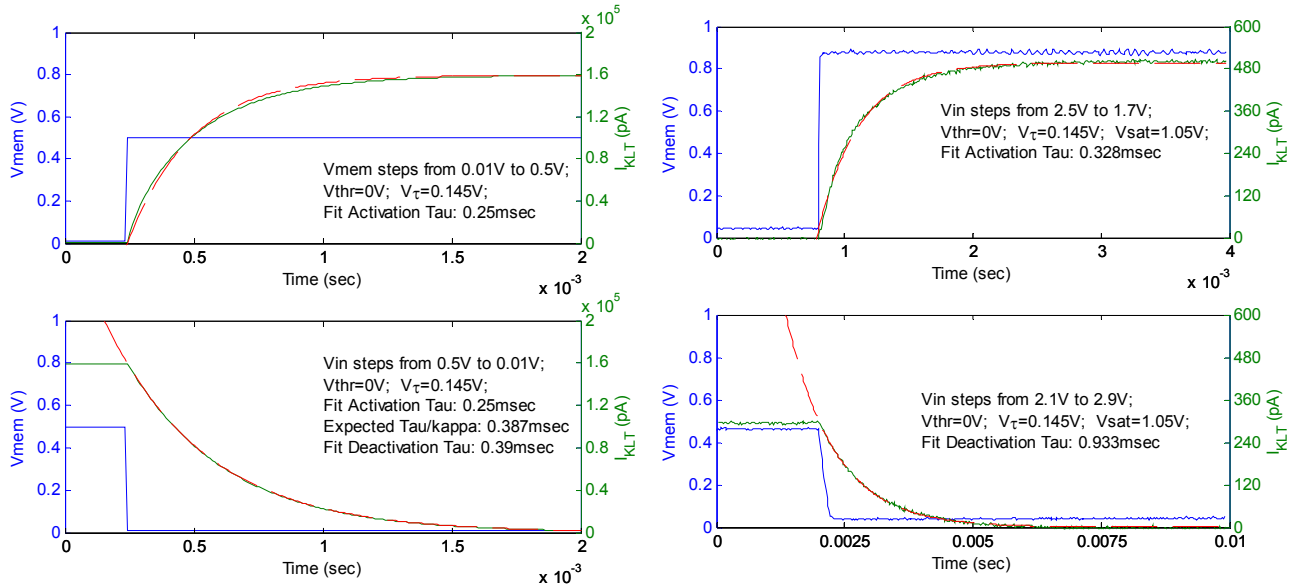
**A3.1: The silicon  $K_{LT}$  I-V Curve: theory versus class chip data** (left) Analytical solution to the steady state  $I_{KLT}$  equation. Four sets of  $K_{LT}$  parameters are displayed, as indicated in the legend. Simplified solutions to the  $I_{KLT}$  equation predict an exponential slope of  $\kappa^2$  ( $V_{th} = 0V$ ) and  $2\kappa^2$  ( $V_{th} \gg V_{mem}$ ). (right) I-V curves measured on a class chip.  $V_{mem}$  and  $I_{KLT}$  were recorded while stepping  $V_{in}$  from 1.5 to 2.5V in 10mV increments. The same sets of four parameters were used to construct these curves. Additionally, the effects of  $V_{sat}$  are shown while setting  $V\tau$  to 0.1V and  $V_{thr}$  to 0V. Measured currents were divided by an approximate pad gain of 1000. Deviations from theory include a decrease in slope at high  $V_{mem}$  values as the transistor currents increase above threshold, and the set of points at approximately  $10^{-5}$ A which result from neuron spiking.

$$(A3.5) \text{ Activation: } I_{KLT}(t) \approx (I_{KLT}(\infty) - I_{KLT}(0)) \left(1 - e^{-t/\tau_{vk}}\right)^\kappa + I_{KLT}(0); \quad \{V_{thr} \ll V_K\}$$

$$(A3.6) \text{ Deactivation: } I_{KLT}(t) \approx (I_{KLT}(\infty) - I_{KLT}(0)) \left(e^{-t/\tau_{vk}}\right)^\kappa + I_{KLT}(0); \quad \{V_{thr} \ll V_K\}$$

The time course of  $I_{KLT}$  activation and deactivation is asymmetric. This is due to using nMOS transistors to implement the low pass filter that drives  $I_{KLT}$ . The low pass filter sub-circuit is activated by the transistor with a gate voltage of  $V_A$ , which dumps current onto  $C_{KLT}$  increasing  $V_K$  which drives  $I_{KLT}$ . The sub-circuit is deactivated by the  $V\tau$  transistor, which draws  $sat$  current from  $C_{KLT}$  decreasing  $V_K$ . Asymmetry in the time course of activation and deactivation stems from the form of the differential equation found in Equation 3. This equation describes the time course of  $\exp(V_K/u_t)$ , though  $I_{KLT}$  is proportional to  $\exp(\kappa V_K/u_t)$ . In Equations 5 and 6, I show how this differential equation affects the step response of  $I_{KLT}$  when  $V_{thr} \ll V_K$ . The time constant ( $\tau_{vk}$ ) is defined in Equation 3, while  $I_{KLT}(0)$  and  $I_{KLT}(\infty)$  are the steady state solutions to the beginning and end of the step response. Deactivation of  $I_{KLT}$  follows an exponential time course in the for  $\exp(-t/\tau_{vk})^\kappa$ , therefore the time constant for deactivation of  $I_{KLT}$  is  $\tau_{vk}$  divided by  $\kappa$ . The equation describing activation follows an exponential time course of the form  $(1 - \exp(-t/\tau_{vk}))^\kappa$ , and

because  $\kappa$  does not equal one, a single time constant for  $I_{KLT}$  activation cannot be described analytically. Figure A3.5 compares the analytical time course of  $I_{KLT}$  with data from the class chip. I fit the activation data with a single exponential to approximate its time constant. My theoretical results predict a deactivation time constant 1.5 times greater (slower) than the approximate activation time constant. Chip data indicates that this asymmetry is even greater than predicted, with a deactivation time constant 2.5 times greater than the approximate activation time constant.



**A3.5: Time course of  $K_{LT}$  activation and deactivation: theory versus class chip data** (left) Analytical solution to the time course of  $I_{KLT}$  activation and deactivation in response to a step in membrane voltage. Transistor parameters are the same used to calculate the steady state I-V curves in Figure A3.4. The analytical solutions presented here do not make the simplifying assumption that  $V_K \ll V_{thr}$  (Equations 5 and 6), though  $V_{thr}$  was set to 0V. Converting  $\exp(V_K/u)$  to  $I_{KLT}$  involves exponentiating by  $\kappa$ , which differentially affects the activation and deactivation time constants; the deactivation time constant equals  $\tau_{VK}/\kappa$ , but activation cannot be analytically described with a single time constant. The deactivation time constant is approximately 1.5 times greater (slower) than the approximate activation time constant when  $\kappa$  equals 0.79. (right) Time course of  $I_{KLT}$  activation and deactivation measured on the class chip. On chip the  $I_{KLT}$  deactivation time constant is roughly 2.8 times greater than the approximate activation time constant. Measured currents were divided by an approximate pad gain of 1000.

### Criticism of class chip auditory neuron

The class chip auditory neuron is a good first approximation to modeling a bushy cell. With  $I_{KLT}$  active,  $V_{mem}$  varies dynamically with a step input current (Figure A3.3, right), as is found in biological bushy cells. This silicon implementation of an integrate-and-fire neuron is compact in terms of surface area;  $V_{mem}$  and the spike circuitry are implemented with a single capacitor and eight transistors. The  $K_{LT}$  circuit is also quite compact, with an additional capacitor and six transistors. Integrate-and-fire models are commonly used in neural simulations, though Rothman and colleagues (Rothman et al. 1993) found this simplified neural model is insufficient for describing the response of bushy cells in the cochlear nucleus. Conductance based bushy cell models, which will be discussed in Appendix 4, exhibit a

change in membrane time constant with  $V_{mem}$ . Due to a reduction in input resistance as voltage dependent conductances activate, a constant input current becomes less effective as the neuron membrane depolarizes.

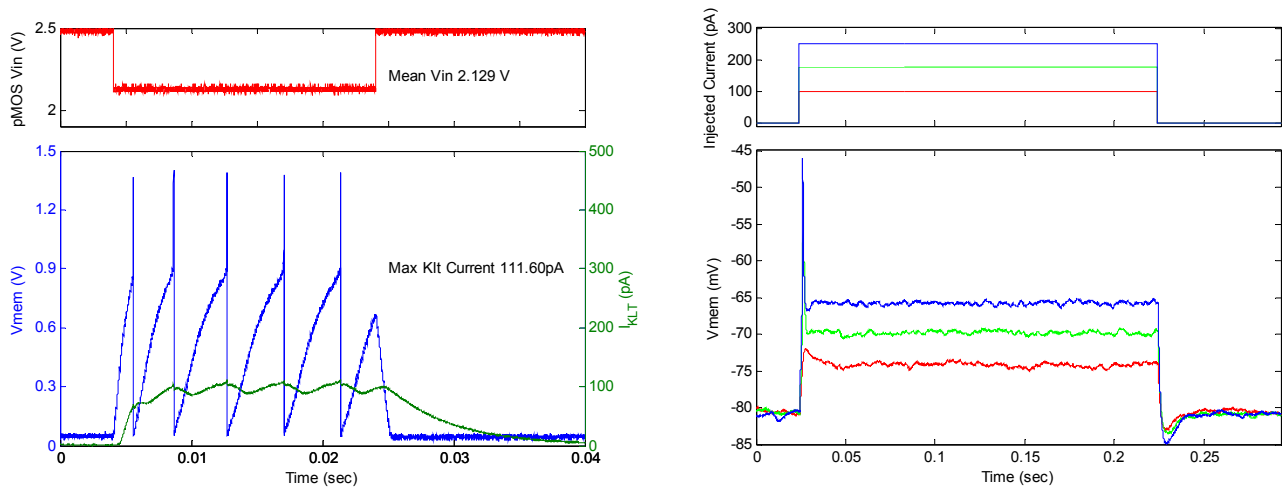
A second flaw with this neuron design is the asymmetry of  $I_{KLT}$  activation and deactivation time course. Characterization of  $K_{LT}$  by Rothman and Manis (2003a, Figure 12 in this proposal), show activation and deactivation have similar time constants. The asymmetry caused by implementing the time course of  $I_{KLT}$  with nMOS transistors results in a deactivation time constant 2.5 times greater than that of activation. Additional on chip characterizations (not shown) revealed this discrepancy can be as large as a 3.6 fold difference. Both biological and this silicon bushy cell are able to respond to a depolarizing current injection with a single spike. Bushy cells also phase lock to pure tone acoustic stimuli up to a few kHz. When stimulating the silicon neuron with high frequency pulses to mimic synaptic input from the auditory nerve, the slow deactivation of  $K_{LT}$  effectively inhibits multiple responses. A symmetric time course of  $K_{LT}$  activation and deactivation may therefore be required for bushy cells to respond with a single spike to depolarizing current injection yet encode the phase of an acoustic stimulus. In Appendix 4, I will present a pMOS low pass filter that has symmetric activation and deactivation time courses.

In biology,  $K_{LT}$  is active at rest which reduces the membrane resistance, effectively lowering the membrane time constant (Golding et al. 1999). In order to approximate bushy cell function, I set  $V_{thr}$  to zero so that  $K_{LT}$  would be maximal at rest for whatever  $V\tau$  value I used. Therefore, this circuit could be made more efficiently by eliminating  $V_{thr}$  and one of the  $V_K$  transistors. In this case the circuit would only consist of a capacitor and four transistors, but would essentially function identical to that of the current design.  $I_{KLT}$  would then be equal to  $I_o \exp(\kappa V_K/u_t)$ , so the I-V curve would look like that with  $V_{thr}$  set to zero, but shifted up by a factor of two.

This silicon neuron's response is quite sensitive to current injection level compared to a biological bushy cell. In Figure A3.6 (left), I show the response of the silicon bushy cell an input current greater than the threshold to elicit a single spike. I stepped  $V_{in}$  10mV lower than the spike threshold shown in Figure A3.3, which corresponds to a 1.35 fold increase in  $I_{in}$  assuming the measured pMOS  $\kappa$  value of 0.789. This increase in  $I_{in}$  leads to repetitive spiking during the 20msec current injection, presumably because  $I_{in}$  exceeds the maximum  $I_{KLT}$  value. In contrast, a biological bushy cell consistently fires just once at the onset of current injection even when the current level is several times greater than that required to elicit a spike (Figure A3.6 right demonstrates the single spike response over a 1.4 fold increase in the 175pA spike threshold). This result was identified by Rothman and Manis (2003b) who observed a wide range of maximal  $I_{KLT}$  values that consistently resulted in a single onset spike. The robustness of the biological bushy cell response is likely a result of several features including a large  $K_{LT}$  current, the conductance mode operation of the cell membrane, the electrotonic distance of the axon hillock, and voltage dependent inactivation of sodium channels.

Rothman and Manis found the single spike response was consistent despite variability in the threshold voltage and peak magnitude of  $I_{KLT}$ . They found the single spike response consistently occurred when the slope of the whole cell I-V curve exceeded a particular value – this slope was primarily determined by the magnitude of  $I_{KLT}$ . Therefore I suggest that the consistency of the bushy cell response is primarily due to the magnitude of  $I_{KLT}$  with respect to the input currents tested. Due to the compact design of this silicon bushy cell, the maximal  $I_{KLT}$  is limited by  $V_{sat}$ , which

is necessarily low to prevent above-threshold gate voltages at node  $V_A$ . If  $V_{sat}$  is set high to  $V_{dd}$ ,  $I_{KLT}$  fully activates within tens of nanoseconds whenever the neuron spikes, drastically increasing the asymmetry in activation and deactivation described above. Therefore  $V_{sat}$  must be used to limit  $V_A$ , though it also limits  $I_{KLT}$ , reducing the robustness of the single spike response. The silicon design of  $K_{LT}$  I present in Appendix 4 has separate pathways for sensing  $V_{mem}$  and outputting  $I_{KLT}$  to avoid this problem. A second feature of the biological bushy cell that possibly inhibits multiple spikes is the conductance mode operation of the cell. The biological bushy cell reduces its membrane resistance as  $K_{LT}$  activates, which in turn reduces the effectiveness of  $I_{in}$  at depolarizing the cell.



**A3.6: Silicon auditory neuron response is stable over a narrow range of input currents compared to a biological bushy cell** (left) Increasing  $I_{in}$  past spike threshold quickly results in multiple spikes.  $V_{in}$  is 10mV lower than shown in Figure A3.3, which corresponds to a 1.35x increase in current (assuming  $\kappa$  is 0.789 and  $u_i$  is 26mV).  $K_{LT}$  parameters are the same as in Figure A3.3:  $V_{sat}$  is 1.062V,  $V_{thr}$  is 0 V and  $V\tau$  is 100mV. (right) A current clamp recording from a mouse bushy cell reveals the robustness of its single spike response. The input current required to elicit a single spike was 175pA (green). This cell continued to respond with just a single spike when the input current was increased 1.42 times greater than threshold (250pA, blue). Data recorded by M. McGinley from Dr. Oertel's laboratory. Membrane voltage has been corrected for a -12mV junction potential.

Two additional features of the biological bushy cell that potentially inhibit multiple spikes have to do with its axon hillock. In Figure A3.6 (right) it appears that the bushy cell axon hillock is electrotonically distant from the cell body. This is evident from the peak of the action potential, which is well below the sodium reversal potential of 55mV, and the lack of post-spike repolarization in this somatic current clamp recording. Increased electrotonic distance means the axon hillock is subjected to an attenuated version of the somatic  $V_{mem}$ ; it is likely filtered in both time and space as is approximated by the cable equation. Such filtering may help to inhibit multiple spikes as the apparent  $V_{mem}$  at the hillock is reduced, or because the additional delay allows  $I_{KLT}$  close to the hillock to sufficiently counteract the depolarization caused by current injection. Another possible mechanism for reducing multiple spikes is inactivation of the fast sodium channels responsible for action potential initiation. Santos-Sacchi (1993) found a strong voltage dependence on sodium inactivation when characterizing guinea pig spiral ganglion cells which also express  $K_{LT}$ . Such inactivation would limit the neurons ability to spike even if  $V_{mem}$  surpasses the spike threshold.

In conclusion, the auditory neuron on the class chip is a compact representation of an integrate-and-fire neuron with a low-threshold potassium current. In a narrow regime of input currents and bias values, the response of this silicon neuron reasonably approximates that of a biological bushy cell. I have analytically described the  $K_{LT}$  channel of this neuron, which qualitatively matches data collected from the class chip. The primary feature of this design is its space efficiency; the implementation of the spike mechanism and  $K_{LT}$  circuitry use a minimal number of transistors and capacitors. Computational modeling indicates that an integrate-and-fire model is insufficient for describing the precise timing of the bushy cell response. Additionally, the nMOS implementation of  $I_{KLT}$  creates an asymmetry in the time course of activation and deactivation. Most importantly, the characteristic single spike response of this neuron is not robust over a wide range of input currents. This results from the necessary restriction of  $I_{KLT}$  magnitude when adjusting biases so the time course of activation is dictated by sub-threshold current levels. Other features of the biological neuron may also contribute to its ability to consistently spike only once at the onset of current injection.

### **Literature Cited in Appendix 3:**

- Golding, N.L., Ferragamo, M.J. and Oertel, D. (1999). Role of Intrinsic Conductances Underlying Responses to Transients in Octopus Cells of the Cochlear Nucleus. *J Neurosci* 19(8): 2897-905.
- Rothman, J.S. and Manis, P.B. (2003a). Differential Expression of Three Distinct Potassium Currents in the Ventral Cochlear Nucleus. *J Neurophysiol* 89(6): 3070-82.
- Rothman, J.S. and Manis, P.B. (2003b). The Roles Potassium Currents Play in Regulating the Electrical Activity of Ventral Cochlear Nucleus Neurons. *J Neurophysiol* 89(6): 3097-113.
- Rothman, J.S., Young, E.D. and Manis, P.B. (1993). Convergence of Auditory Nerve Fibers onto Bushy Cells in the Ventral Cochlear Nucleus: Implications of a Computational Model. *J Neurophysiol* 70(6): 2562-83.
- Santos-Sacchi, J. (1993). Voltage-Dependent Ionic Conductances of Type I Spiral Ganglion Cells from the Guinea Pig Inner Ear. *J Neurosci* 13(8): 3599-611.

## Appendix 4: Conductance neuron circuit model

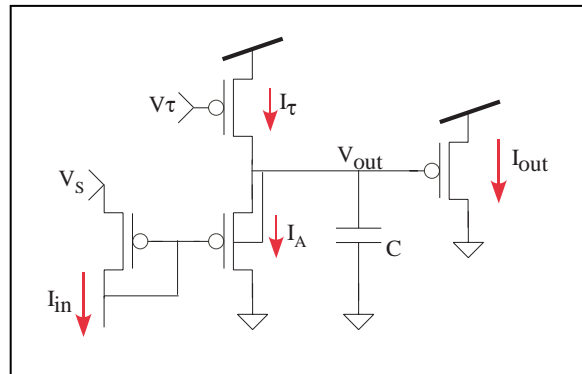
In this appendix, I present three circuit diagrams; the pMOS low-pass filter, my generalized silicon conductance model, and my silicon bushy cell implementation. The purpose of this section is not to rigorously analyze these circuit models as in Appendix 3, but rather to briefly describe their function, and how they will be used as building blocks for my cochlear nucleus chip. Detailed analysis will be presented in my thesis, along with chip data for comparison.

### pMOS Low-Pass Filter

The following circuit is similar to the nMOS low-pass filter used to realize the time course of activation and deactivation of the  $K_{LT}$  circuit in Appendix 3. The nMOS low-pass has asymmetric activation and deactivation time constants because the differential equation describing its time course lacks  $\kappa$  (Equation 3 from Appendix 3 is in terms of  $\exp(V_K/u_t)$  rather than  $\exp(\kappa V_K/u_t)$ ). Design of the pMOS low-pass filter circumvents this issue by connecting the well of the activating transistor (passing  $I_A$  in the diagram below) to  $V_{out}$ . This leads to a differential equation in terms of  $I_{out}$ , and a time constant of  $(u_t C / \kappa I_\tau)$  for both activation and deactivation. The following implementation of a pMOS low-pass filter also has a gain ( $A_S$ ) set by the source bias labeled  $V_s$ . This circuit operates as follows: a step increase in  $I_{in}$  is amplified by the gain factor  $A_S$ , this amplified current is drawn from the capacitor through  $I_A$ , decreasing  $V_{out}$  and increasing  $I_{out}$ . The current  $I_A$  is proportional to  $I_{in} I_s / I_{out}$ ; as  $I_{out}$  increases during activation,  $I_A$  becomes less effective at drawing charge from the capacitor. This leads to the exponential time course of  $I_{out}$  activation. A step decrease in  $I_{in}$  immediately decreases  $I_A$ , such that  $V_{out}$  is linearly increased toward  $V_{dd}$  by  $I_\tau$ . This causes the exponential time course of  $I_{out}$  deactivation.

Equation governing the pMOS LPF with gain:

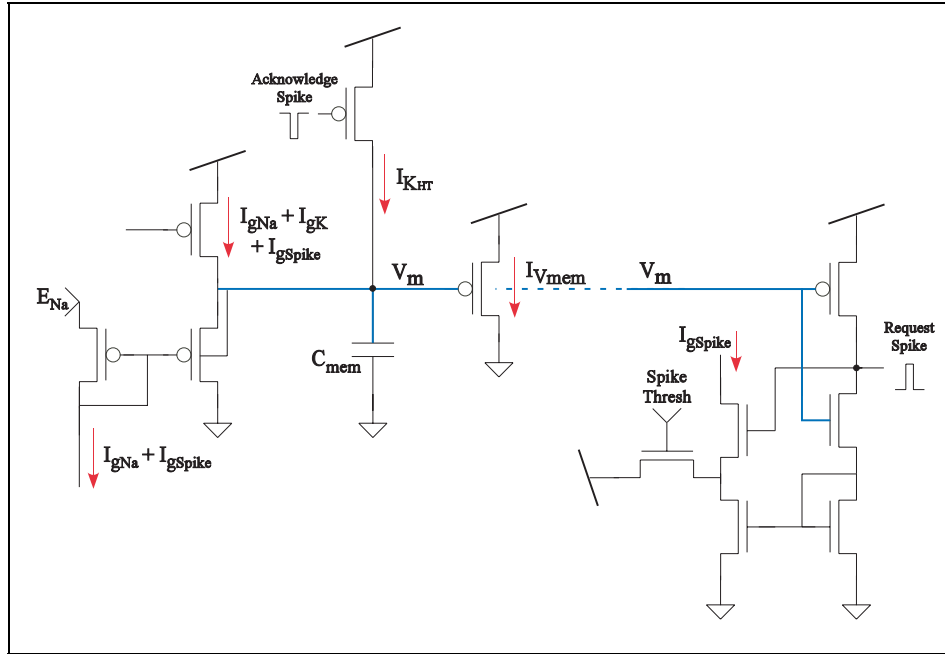
$$\left( \frac{u_t C}{\kappa I_\tau} \right) \frac{dI_{out}}{dt} + I_{out} = I_{in} A_S; \quad \left\{ A_S = e^{\frac{\kappa}{u_t}(V_\tau - V_s)} \right\}$$



### General Silicon Conductance Model

The following circuit utilizes the pMOS low-pass filter to implement a neuron membrane. Unlike the integrate-and-fire neuron presented in Appendix 3, this neuron's membrane voltage is represented by a current ( $I_{V_{mem}}$ ) instead of a voltage ( $V_{mem}$ ). This is because the pMOS low-pass filter is a current-mode device; its output current is a low-pass version of its input current. As  $I_{V_{mem}}$  is represented by pMOS transistors, a reduction in  $V_m$  leads to an increase in  $I_{V_{mem}}$ . This conductance neuron's positive feedback spiking circuitry draws charge from  $C_{mem}$  to increase  $I_{V_{mem}}$ , as opposed to the positive feedback circuitry used in the integrate-and-fire neuron which dumps charge onto the

$C_{mem}$  to increase  $V_{mem}$ . The high threshold potassium current ( $I_{KHT}$ ) is implemented with a pMOS transistor that resets  $V_{mem}$  after a spike by pulling  $V_m$  up to  $V_{dd}$ . The analytical solution to  $I_{V_{mem}}$  of this circuit mimics the conductance equation described by Hodgkin and Huxley (1952), if the reversal potential of potassium ( $E_K$ ) is zero.



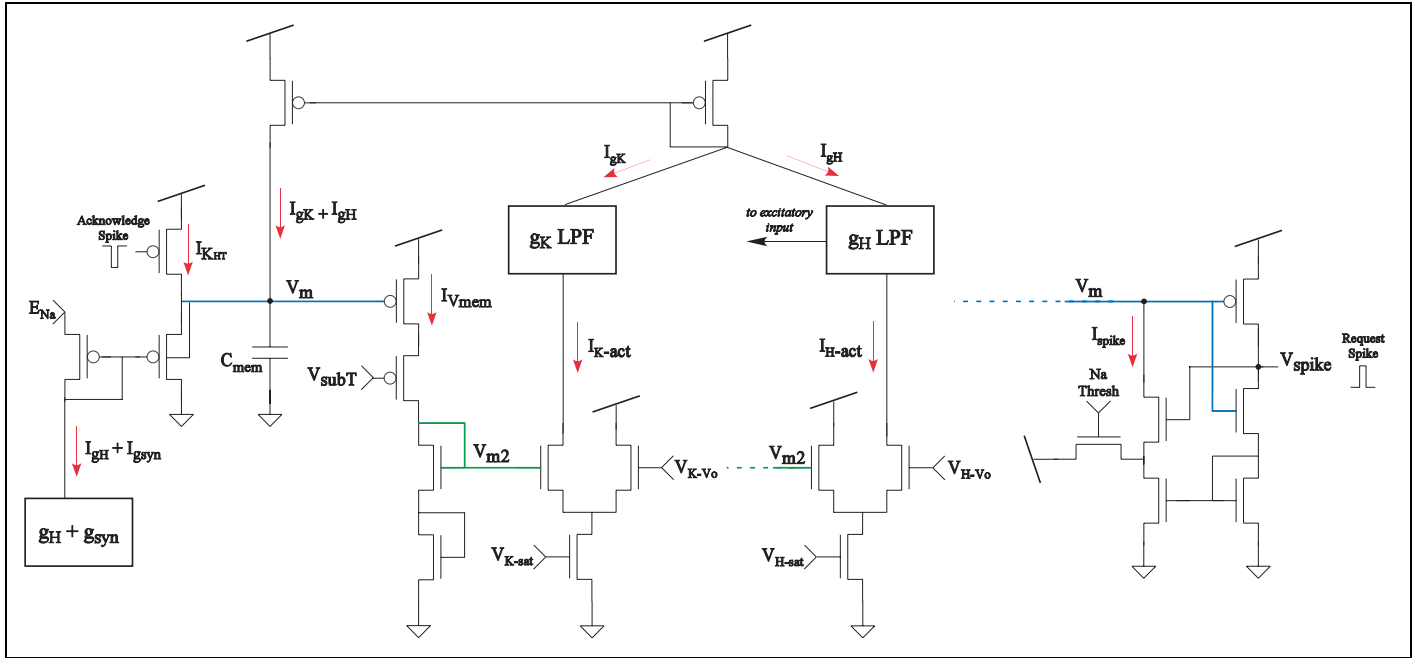
Equation governing the general silicon conductance model:

$$\frac{1}{\kappa} \left( \frac{u_t + C_{mem}}{I_{gNa} + I_{gSpike} + I_{gK} + I_{gKHT}} \right) \frac{dI_{V_{mem}}}{dt} + I_{V_{mem}} = \frac{I_{gNa} I_{E_{Na}} + I_{gSpike} I_{E_{Na}} + I_{gK} I_{E_K} + I_{gKHT} I_{E_K}}{I_{gNa} + I_{gSpike} + I_{gK} + I_{gKHT}}; \quad \left\{ I_{E_{Na}} = e^{\frac{\kappa}{u_t} E_{Na}}; I_{E_K} = 0 \right\}$$

### Silicon Bushy Cell Implementation

In Figure 14 of this proposal, I present simulation results from the following silicon bushy cell model. This model is conductance based with two voltage sensitive conductances in addition to the standard spike mechanism; a low-threshold potassium conductance ( $g_K$ ) and mixed-cation hyperpolarization activated conductance ( $g_H$ ) are implemented using pMOS low-pass filters (schematized with boxes in the circuit diagram below). The inputs into these filters ( $I_{K-sat}$  and  $I_{H-sat}$ ) are driven by a current ( $\hat{I}_{V_{mem}}$ ) that grows faster than the square of  $I_{V_{mem}}$  because  $\kappa$  is less than one. Both inputs are controlled by independent biases affecting the conductances' saturation levels ( $V_{K-sat}$  and  $V_{H-sat}$ ) and half activation voltages ( $V_{K-V_0}$  and  $V_{H-V_0}$ ). Notice the difference between  $g_K$  activation and  $g_H$  activation;  $g_K$  activates with increasing  $I_{V_{mem}}$  therefore  $I_{K-sat}$  must pass through the transistor with  $V_{m2}$  at its gate, while  $g_H$  activates with decreasing  $I_{V_{mem}}$  so  $I_{H-act}$  must pass through the transistor with  $V_{E-V_0}$  at its gate. The output of the  $g_K$  low-pass filter is a current that increases  $V_m$  and reduces the time constant of the conductance equation. In contrast, the output of the  $g_H$  low-pass filter also increases  $V_m$  to reduce the membrane time constant, but additionally is multiplied by  $I_{E_{Na}}$  to depolarize the cell and increase  $I_{V_{mem}}$ . In the circuit below, I tie the output of the sodium spike directly to  $V_m$  instead of multiplying it by  $I_{E_{Na}}$  and passing it through the membrane low-pass filter (as is done in the general conductance model above). This direct  $V_m$  connection increases the effectiveness and speed of the spiking mechanism without significantly altering the conductance equation describing  $I_{V_{mem}}$ . Each low-pass filter is made up

of four transistors and a capacitor. This silicon neuron model has a total of 27 transistors and three capacitors, almost double the 14 transistors and two capacitors used to implement the silicon neuron presented in Appendix 3.



Equations governing the silicon bushy cell model:

$$\frac{1}{\kappa} \left( \frac{u_t + C}{I_{gK} + I_{gH} + I_{gKHT} - I_{Spike}} \right) \frac{dI_{V_{mem}}}{dt} + I_{V_{mem}} = \frac{I_{gSyn} I_{E_{Na}} + I_{gH} (I_{E_{Na}} + I_{E_K}) + I_{gKHT} I_{E_K}}{I_{gH} + I_{gK} + I_{gKHT} - I_{Spike}}; \quad \left\{ I_{E_{Na}} = e^{\frac{\kappa}{u_t} E_{Na}}; I_{E_K} = 0 \right\}$$

$$I_{K-act} = \frac{1}{I_0} \left( \frac{\hat{I}_{V_{mem}} I_{K-sat}}{\hat{I}_{V_{mem}} + I_{K-V_0}} \right); \quad I_{H-act} = \frac{1}{I_0} \left( \frac{I_{H-V_0} I_{H-sat}}{I_{H-V_0} + \hat{I}_{V_{mem}}} \right); \quad \left\{ \text{where } \hat{I}_{V_{mem}} = I_0 e^{\left(\frac{\kappa-1}{u_t}\right) V_{mem}} > I_{V_{mem}}^2 \right\}$$

$$I_{spike} = \frac{1}{I_0} \left( \frac{I_{V_{spike}} I_{V_{mem}}}{I_{V_{spike}} + I_{NaThr}} \right)$$